Multi-Scale Characterization of the Roles of Alkali Post-Deposition Treatments and Ag-Alloying in Cu(In,Ga)Se_2 Solar Cells

by

Tara M. Nietzold

A Dissertation Presented in Partial Fulfillment
of the Requirement for the Degree
Doctor of Philosophy

Approved August 2021 by the
Graduate Supervisory Committee:

Mariana I. Bertoni, Chair
Martin Holt
William N. Shafarman
Sefaattin Tongay

ARIZONA STATE UNIVERSITY

December 2021

ABSTRACT

Thin film solar cells are based on polycrystalline materials that contain a high concentration of intrinsic and extrinsic defects. Improving the device efficiency in such systems relies on understanding the nature of defects - whether they are positive, negative, or neutral in their influence - and their sources in order to engineer optimized absorbers. Oftentimes, these are studied individually, as characterization techniques are limited in their ability to directly relate material properties in individual layers to their impact on the actual device performance. Expanding the tools available for increased understanding of materials and devices has been critical for reducing the translation time of laboratory-scale research to changes in commercial module manufacturing lines.

The use of synchrotron X-ray fluorescence (XRF) paired with X-ray beam induced current and voltage (XBIC, XBIV respectively) has proven to be an effective technique for understanding the impact of material composition and inhomogeneity on solar cell device functioning. The combination of large penetration depth, small spot size, and high flux allows for the measurement of entire solar cell stacks with high spatial resolution and chemical sensitivity. In this work, I combine correlative XRF/XBIC/XBIV with other characterization approaches across varying length scales, such as micro-Raman spectroscopy and photoluminescence, to understand how composition influences device performance in thin films.

The work described here is broken into three sections. Firstly, understanding the influence of KF post-deposition treatment (PDT) and the use of Ag-alloying to reduce defect density in the Ga-free material system, $CuInSe_2$ (CIS). Next, applying a similar characterization workflow to industrially relevant Ga-containing $Cu(In_{1-x}Ga_x)Se_2$ (CIGS) modules with Ag and KF-PDT. The influence of light soaking and dark heat exposure on the modules are also studied in detail. Results show that Ag used with KF-PDT in CIS causes undesirable cation ordering at the CdS interface and affects the device through increased potential

fluctuations. The results also demonstrate the importance of tuning the concentration of KF-PDT used when intended to be used in Ag-alloyed devices. Commercially-processed modules with optimized Ag and KF concentrations are shown to have the device performance instead be dominated by variations in the CIGS composition itself. In particular, changes in Cu and Se concentrations are found to be most influential on the device response to accelerated stressors such as dark heat exposure and light soaking. In the final chapter, simulations of nano-scale XBIC and XBIV are done to contribute to the understanding of these measurements.

ACKNOWLEDGEMENTS

Thank you to all of my collaborators and the funding sources that made this research possible. Thank you to everyone at MiaSole Hi-Tech Corp. (Jeff, Dmitry, Rouin) for their commitment to my success throughout my entire PhD. Thank you as well to my collaborators at University of Delaware, Dr. Shafarman and Dr. Nick Valdes, those at SLAC, Dr. Schelhas and Dr. Sinha, and those from the Holman Group, Dr. Arthur Onno, Barry Hartweg, and Mason Mahaffey, all of who were pivotal in the final stages of completing my thesis. A very big thank you also to Barry Lai, Zhonghou Cai, and Martin Holt, as well as many others at the Advanced Photon Source of Argonne National Laboratory. Thank you also to Dr. Tongay for always being supportive and encouraging. A particular thanks also to Michael Stuckelberger for everything you taught me.

Thanks to the IGERT program and the friends I made along the way. And thanks to all of the friends I have made at conferences, through random projects, and through QESST.

Thanks to my fellow lab mates, especially those from the founding days who made research fun and supported me through the highs and lows.

Thanks to my family. All of my success is entirely because of their love and support throughout my entire life.

Last, but not least, thank you to my boss, Dr. Mariana Bertoni. Thank you for accepting me in the lab as an NNIN REU student. Thank you for pushing me to apply to graduate school and just try it. Thank you for pushing me for the next five years afterwards, too. Thanks for teaching me to be the person and researcher I am. And thank you for making it fun.

TABLE OF CONTENTS

CHAPTER Page

CHAPTER Page

LIST OF TABLES

LIST OF FIGURES

Figure Page

Figure Page

Figure Page

Figure Page

Figure Page

Figure Page

Figure Page

Figure Page

Figure Page

Figure Page

Figure Page

Chapter 1

INTRODUCTION

1.1 Thin Film Photovoltaics

In 2018, the total number of people across the globe without access to electricity fell below 1 billion [1]. Considering that as of July, 2019 the global population was just under 7.58 billion people [2], this accounts to just over 13% of the global population having limited-to-no access to electricity. Solar energy, due to its increased reliability and efficiency, and lower cost, can substantially improve electricity access and in turn the global standard of living. Estimates by the U.S. Energy Information Agency (EIA) show electricity generation by renewables growing from 19% in 2020 to 38% by 2050 [3] and being the only sector of electricity generation to grow at all, in comparison to natural gas, nuclear, and coal. Within the breakdown of the renewables category, solar energy is anticipated to grow the most and is projected to account for 46% of all renewable electricity generation by 2050.

Silicon solar cells continue to dominate the solar industry in terms of overall installed capacity [4, 5]. While solar cells using silicon substrates boast high efficiencies surpassing now 26% [6, 7] and long module lifetimes, thin film technologies offer certain benefits and therefore remain. For example, III-V materials such as GaAs and GaInP remain the leader in solar materials for space applications due to their ability to form highly efficient devices that can withstand the demanding environmental conditions of outer space [8, 9]. Additionally, the chalcogenide material system $Cu(In_{1-x}Ga_x)Se_2$ has been demonstrated for commercial viability for flexible applications [10–12], including wearable electronics and building integrated photovoltaics (BIPV) [13, 14]. These flexible modules compete

directly with silicon modules in efficiency, recently reaching 18.64% efficiency [15].

In order for thin film solar cells to remain cost competitive and capable of meeting the needs of particular applications, they must further improve the efficiency to approach the material's maximum theoretical conversion efficiency [12]. Optimizing the device efficiencies has proven to be one of the most effective ways to reduced the levelized cost of energy (LCOE), in $ per kWh, of solar technologies [16, 17]. In thin film CIGS solar cells, the absorber quality plays a significant role in the performance losses. Current losses occur due to light reflection and incomplete light trapping, as well as absorption losses in the Mo back contact and parasitic absorption in the CdS and ZnO front contact [12]. Limitations to achieving maximum open-circuit voltages (V_{oc}) instead occur due to recombination losses through defects, compositional inhomogeneity, and electrostatic potential variations [18].

Beyond these improvements, demonstration of successful implementation in tandem devices is critical. Tandem solar cells allow for modules to surpass individual theoretical limits by combining materials with varied bandgap energies to maximize the absorption and conversion of light. Thus far, CIGS and Ga-free $CuInSe_2$ materials have been incorporated into CIGS/perovskite tandem devices achieving 25% efficiency in a four-terminal tandem configuration [19]. The combination of perovskites with CIGS thin films is particularly promising for future applications because they could in theory be developed into flexible, lightweight modules.

1.2 Motivation

The semiconductor $Cu(In_{1-x}Ga_x)Se_2$ is a p-type, direct bandgap material [20, 21]. The bandgap can range from 1.0-1.7 eV depending on the [Ga]/[Ga]+[In] (GGI) ratio, with increasing Ga concentration equating to a wider bandgap. CIGS is often doped p-type by maintaining the Cu concentration below the stoichiometric value [22]. The material is thermodynamically stable despite being Cu-poor due to the compensating formation of defects

[23]. Despite the existence of high concentrations of defects in CIGS, device efficiencies are now above 23% for laboratory-scale devices [24].

The defects found in CIGS can be both beneficial and detrimental, perplexing researchers for many years. These defects can vary significantly in length-scale, some presenting themselves as individual point defects [25] up to entire micron-sized clusters of ordered defect compounds (ODCs). These defects also include potential variations at grain boundaries [26] and the formation of interface phases between CIGS and CdS or CIGS and Mo. To measure all existing defects and quantify their impact on device performance therefore proves to be a complex measurement challenge. A thorough understanding of individual defects and their impact is necessary for addressing the current and voltages losses in CIGS thin film solar cells.

In the present day, efficiency improvements in CIGS-based solar cells has come through the addition of even more elements, such as the alloying of the Cu-site with Ag. Defect passivation through the incorporation of alkali elements, such as Na or K, has also helped improve performances [27]. Any additional elements that are added to the CIGS crystal only further expand and complicate the parameter space of potential defects. With industry moving along with the incorporation particularly of Ag and K, it is critical to form an understanding of their impact on the absorber quality for the field to progress.

Therefore, the goal of this work is to focus on understanding the formation of defects and their impact on device performance in CIGS. To do so, a comprehensive study on laboratory and industrially-relevant cells treated with Ag and K was conducted using a multi-scale characterization approach.

1.3 Approach

By addressing defect composition and spatial variation, significant improvements can be made to the device performance of CIGS solar cells. Measurements of both device

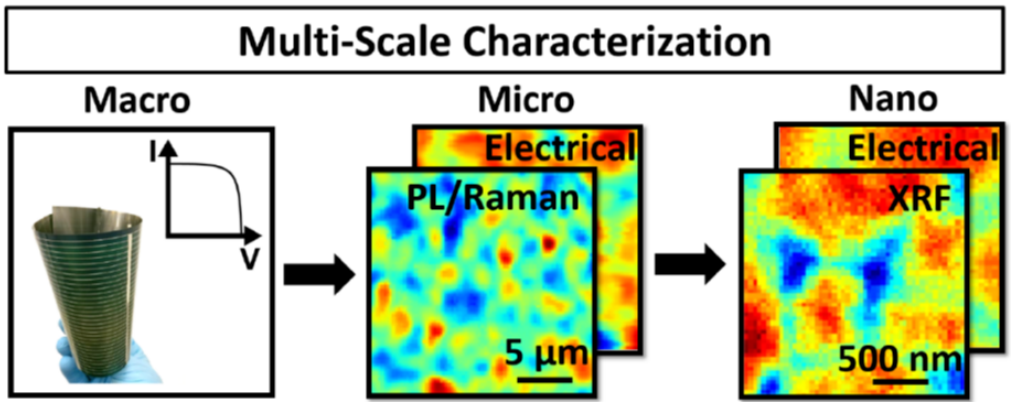

Figure 1.1: Example of the workflow used to connect information on multiple scales of CIGS solar cells. Taken from West [28].

performance and film quality need to be conducted across multiple length scales to identify the largest contributors to efficiency losses. One of the major challenges with this approach is the ability to connect observations across length scales. In order to do so, this work relies on correlative measurements on the nano- and micro-scale that directly relate materials properties to local current and voltage measurements.

The process is built upon the workflow described by West [28] and shown in Figure 1.1. Devices are always characterized first using light and dark J-V (current density vs. voltage) to evaluate the efficiency of the devices. On the micro-scale, the devices are evaluated using photoluminescence (PL) mapping and Raman spectroscopy. By using a laser with a spotsize on the order of 1 µm, sample areas of 20 µm x 20 µm are studied multiple times for increased statistics. From the PL results, information on the band-to-band recombination is obtained. The measurement is then repeated in the configuration for Raman spectroscopy, for the direct correlation between the two results. Raman spectroscopy provides information on changes in the CIGS structure and also informs about the formation and concentration of any secondary phases or ordered defect compounds.

Measurements on the nano-scale were then used to study closely the compositional variations in the device. Nano-scale X-ray fluorescence (XRF) measurements were done si-

multaneously with X-ray beam induced current (XBIC) and voltage (XBIV). Similar measurements have been done to examine defects and impurities in Si wafers [29–31], study the in-situ growth of CIGS absorber layers [32], and to analyze the temperature response of CIGS solar cells [33]. The results from XRF mapping indicate the impact of additional treatments like Ag-alloying and KF-PDT on compositional inhomogeneity. XBIC describes local electron-hole pair generation, similar to what occurs during standard solar cell operation [34].

In the following sections, we will focus on how these characterization tools can be combined and applied to thin film CIGS solar cells. In Chapter 4, samples without Ga are studied for their response to passivation by post-deposition treatment and A-site alloying to understand defects in Ga-free samples. In Chapter 5, commercial CIGS modules with the same treatments and grown on flexible stainless steel substrates are investigated for compositional variations occurring as a result of accelerated stress testing that serves as an indicator of anticipated long-term field reliability.

Chapter 2

BACKGROUND OF $Cu(In_{1-x}Ga_x)Se_2$ SOLAR CELLS

A solar cell's performance is best summarized by the device efficiency. The efficiency is calculated from the properties of open-circuit voltage (V_{oc}), short-circuit current (J_{sc}), the fill factor (FF), and the incident power, P_{in} following the equation:

$$Efficiency(\eta) = \frac{V_{oc} \cdot J_{sc} \cdot FF}{P_{in}}$$

The parameters are measured through a current density-voltage (JV) curve that studies the device current density, in mA/cm^2, as a function of applied voltage, in V, under illumination and in the dark [35]. An example of a JV curve is shown in Figure 2.1, where the maximum power point represents the current and voltage that optimizes the square area under the curve. The V_{oc} has a direct dependence on the material bandgap and recombination while J_{sc} describes the discrepancy between the number of generated carriers and those that recombine, the difference of which is the total collected carriers from a device [36].

Solar cell efficiency is intrinsically limited by the thermodynamic limits established through the Shockley-Queisser (SQ) limit. The SQ limit is calculated for solar cells that are assumed to have only radiative recombination, which describes the process of an electron-hole pair being generated through excitation by photons with energy higher than the semiconductor's bandgap [37]. For this reason, the maximum theoretical efficiency of a solar cell is directly determined by the material bandgap [38]. For CIGS solar cells, the bandgap is controlled through changing the ratio of Ga/In concentration.

Figure 2.2 demonstrates the dependence of SQ efficiency limits on bandgap and in-

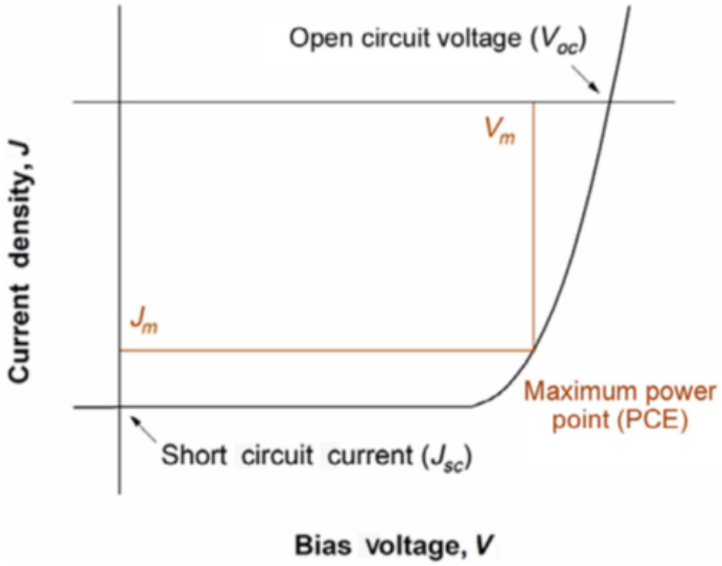

Figure 2.1: An example of a measured current density versus voltage (JV) curve of a solar cell. Taken from Wang *et al.* [35].

cludes markers for the current efficiencies of different solar technologies. CIGS devices are at about 60% of the absolute efficiency (shown in Figure 2.2 by the grey line) [12, 37]. CIGS solar cells remain far from their theoretical efficiency limits due to both lower-than-ideal J_{sc} and V_{oc}[12]. Polman *et al.* cites key losses in J_{sc} arising due to light reflection, incomplete light trapping, and absorption by the other layers in the device [12]. Alternatively, losses in the V_{oc} are often attributed to three key sources: recombination through defects, recombination due to overall film inhomogeneity, and electrostatic potential variations [18].

The theoretical maximum achievable V_{oc} in a direct bandgap solar cell occurs in the situation where there is only radiative recombination [36]. In reality, solar cells exhibit additional mechanisms of recombination that serve to drive down the V_{oc} in a device. They are Shockley-Read-Hall (SRH) recombination, which is the situation where an electron or hole is trapped in a defect state within the solar cell bandgap, Auger recombination, and surface and interface recombination. Under the general assumption that CIGS grains are

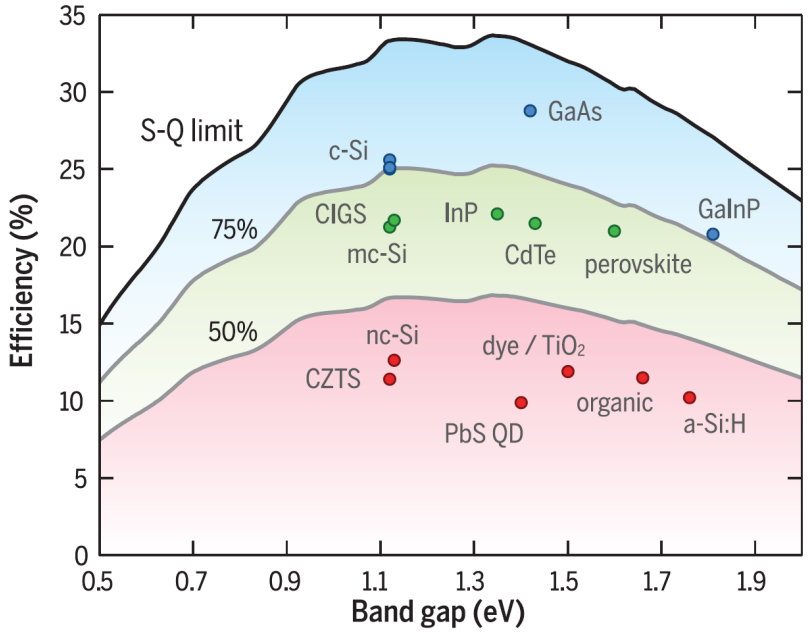

Figure 2.2: A plot of the theoretical Shockley-Queisser efficiency limits as a function of bandgap (the black line). The colored sections are used to separate the materials based on the percentage of the theoretical efficiency limit achieved today by record devices. Taken from Polman *et al.*[12].

grown in parallel, the device voltage is thus limited by the grains with the lowest values [39].

In order to increase V_{oc} and efficiency in CIGS solar cells, the concentration of detrimental defects introduced during film growth needs to be minimized. As the films are almost always grown polycrystalline, grain boundaries also need to be treated to reduce recombination. While defects are important for acquiring marginal improvements in V_{oc}, a growing body of work now agrees that recombination through defects is not the primary source of V_{oc} losses [18, 40]. Instead, Siebentritt particularly cites electrostatic potential variations as being the largest contributor to lower V_{oc} in CIGS [18, 26]. Potential fluctuations arise in semiconductors with high levels of defects as defects become compensated by impurities [41]. The process of defect compensation then results in the formation of Coulomb potential wells that create potential fluctuations [42].

2.1 Growth of $Cu(In_{1-x}Ga_x)Se_2$ Absorbers

Defects in $Cu(In_{1-x}Ga_x)Se_2$ (CIGS) thin film solar cells are primarily addressed and controlled through alterations to the growth process. A number of growth methods have been studied throughout the years, from chemical vapor deposition to electrodeposition [43–45]. The most commonly used and accepted growth method today is 3-stage co-evaporation or co-sputtering that involves different concentrations of the four metal precursors (Cu, In, Ga, and Se) during three separate stages of the process in order to manipulate the relative elemental concentrations throughout the absorber depth and in turn control the concentration of compensating defects [46–49]. In general, the stages of growth follow the sequence: 1) In, Ga, Se deposition; 2) Cu and Se; 3) In, Ga, and Se until a thickness of approximately 1.5-2 μm is achieved [50]. This approach results in the entire growth process being completed in a Se-rich environment. Also, from the stages, one can see that the center of the absorber will be Ga poor, as there is no Ga introduction in stage 2. This demonstrates one of the added benefits of 3-stage co-evaporation, which is the ability to control the Ga composition throughout the depth of the absorber. The control of the Ga composition in depth is often called "grading" and has been demonstrated to improve device efficiency by creating a graded bandgap [27, 47].

The addition of Ga to the second cation site where In sits is done to widen the film bandgap. The bandgap of $CuInSe_2$ to $CuGaSe_2$ ranges from 1.0 to 1.7 eV [21] and thus by manipulating the relative concentrations of In and Ga, the bandgap can be tuned to the close to the ideal value of 1.1 eV, as was found from the SQ limit. The process of Ga-alloying, however, causes increased compositional variation throughout the film and has been related to bandgap fluctuations that were found to limit the V_{oc} [51, 52]. More recent studies, however, have found that better optimizing the placement of increased Ga concentration within the space charge region can increase the V_{oc} demonstrating the importance

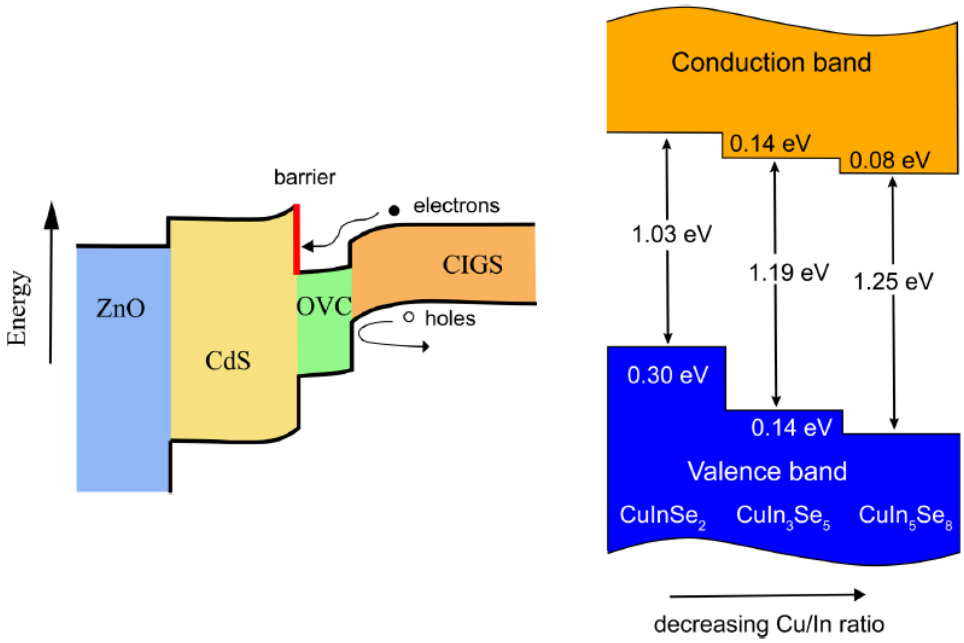

Figure 2.3: A graphical representation of the band diagram for CIS with an layer of ordered vacancy compound (OVC) (left). The relative conduction band and valence band positions and bandgaps are shown for the compounds as they become more Cu-poor from left to right (right). Taken from Sharan *et al.* [57].

of tight control over the placement of Ga during CIGS growth [53, 54]. Kawano *et al.* discovered that double-grading of the [Ga]/[Ga]+[In] (GGI) ratio, where Ga is increased in concentration toward both interfaces, has lead to an increase in J_{sc} up to 40 mA/cm^2 [20]. Overall, improved control of Ga grading in CIGS has alone resulted in efficiencies over 21% [24, 55].

The control of Cu concentration has also been found to be critically important to optimizing the device performance. Particularly, Cu-poor absorber surfaces are almost always preferred compared to Cu-rich ones as they demonstrate decreased surface recombination [22, 56]. Work by Siebentritt *et al.* identified that absorbers with Cu-poor surfaces instead have increased bulk recombination, actually resulting in absorbers with worse transport and recombination properties [23]. However, despite worse bulk properties in Cu-poor CIGS, device performances are generally higher due to the formation of a Cu-poor interface state

occurring at the device junction. This interface state is called an ordered defect compound (ODC), which is an off-stoichiometric CIGS phase that forms as compensation to a high defect density, in this case Cu vacancies.

Ordered defect compounds occurring in $CuInSe_2$ appear as the off-stoichiometric compounds such as $CuIn_3Se_5$ and $CuIn_5Se_8$. They are particularly beneficial when they occur at the CdS/CIS interface because of their larger bandgap [23]. In particular, the ODCs have a greater valence band offset (VBO) than at the conduction band, resulting in a hole barrier at the junction, as shown in the schematic in Figure 2.3(left). Note that the ODC layer may also be called an ordered vacancy compound (OVC), as is labeled in the figure from Sharan *et al.* [57]. Figure 2.3(right) shows the relative band offsets and bandgap energies for the ideal CIS and two most common ODCs. The figure shows the decrease in both conduction band and valence band, and also shows that the offset is greater for the valence band energy.

As mentioned, the formation of ODCs or OVCs occurs as a factor of high defect or vacancy density in the films. These defects are highly cited as being the pair between copper vacancies and In-Cu interstitials, $2V_{Cu}^{-} + In_{Cu}^{2+}$, that is found to occur as one pair per tetragonal $CuInSe_2$ unit cell [57]. The defect pair is cited frequently for being electrically neutral, allowing for the ODC to benefit the device [58, 59]. Particularly, a detailed analysis of defect energy levels and formation energies by Zhang *et al.* found that the passivation of the In_{Cu}^{2+} by $2V_{Cu}^{-}$ is what produces the electrical neutrality of the two defects [58].

Other defect compounds have been found to form beyond the $2V_{Cu}^{-} + In_{Cu}^{2+}$ pair [60]. Specifically, the defect pair of V_{Se}-V_{Cu} has been studied in detail for its existence and impact on device performance [61]. While the formation energy of V_{Se}-V_{Cu} has been estimated to be much higher than that of $2V_{Cu}^{-} + In_{Cu}^{2+}$ and therefore occurs with less frequency, it is found to have a significantly greater impact on performance [59, 62]. The affect from the V_{Se}-V_{Cu} defect pair is attributed almost entirely to the selenium vacancy.

V_{Se} itself acts as an electron trap and this behavior is translated to all other V_{Se}-related defect compounds. Similarly to the control of Cu during growth to deliberately control Cu defect density, the same considerations can be take to minimize detrimental Se defects [61].

Igalson *et al.* identified that the impact of Se defect pairs on the JV characteristics is strongly dependent on the band alignment at the CdS interface and the doping of the CdS itself [63]. Their research also suggested that even in the situation that devices are optimized to reduce the impact of the V_{Se}-V_{Cu} pair, the devices still suffer from the existence of the defect pair in situations such as light soaking, a part of regular device operation. Se vacancies are electron traps that can exhibit different charge levels from +2 to 0. The V_{Se}-V_{Cu} defect pair instead goes from +1 to -1 and therefore can change between an acceptor and a donor [59, 64, 65]. It is hypothesized that this switching in the electronic nature of the V_{Se}-V_{Cu} defect pair, often considered a metastibility, is responsible for the observed trends for long term device performance [66, 67].

2.2 Device Metastability During Operation

When translating laboratory-scale devices to industrial application, it becomes important to consider module reliability and lifetime. Industry standards evaluate modules based on performance metrics for their responses to temperature and humidity cycling as well as light soaking, as is established under the performance standard IEC 61646 for evaluating thin film solar cells [68]. In particular, thin films require an additional test of their response to light soaking since an observed change in device performance, through losses in J_{sc}, V_{oc}, and FF, has been identified by many [25, 65, 69–75]. The observed behavior is largely attributed to the formation and movement of the metastable V_{Se}-V_{Cu} defect pair that gains enough energy from incident light to change its electronic state between an acceptor and a donor [64, 67, 73, 76].

One of the methods suggested for reducing the impact of the V_{Se}-V_{Cu} defect pair is

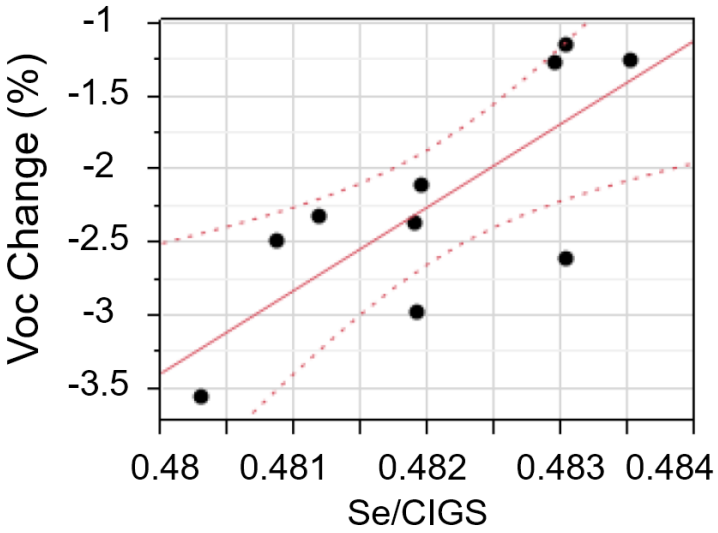

Figure 2.4: A plot of the light soaking-induced V_{oc} change with increasing Se atomic ratio. Taken from Farshchi *et al.* [64].

through changing the Se concentration in the CIGS films. Farshchi *et al.* directly related the V_{oc} losses caused by light soaking in CIGS modules to the relative Se concentration in the CIGS film (Figure 2.4) [64]. The results showed that continual increase in the Se/CIGS ratio reduces the V_{oc} loss incurred from light soaking. The incorporation of additional Se has been found to be effective either when incorporated during an additional annealing step in a Se atmosphere after the CIGS growth [77] or when Se is applied directly to the Mo back contact prior to the CIGS deposition [69]. The added benefit of applying a layer of Se to the back contact first is that it drives the formation of a back surface field [43, 78, 79]. The reason for this is hypothesized to be due to the formation of $MoSe_2$, which forms regardless of the application of a pre-selenization layer and therefore unintentionally consumes Se during the growth process [80]. The consumption of Se for the formation of $MoSe_2$ could potentially explain the high density of V_{Se} observed.

Little evidence has directly related the behavior of the V_{Se}-V_{Cu} complex or other V_{Se}-related defects to light soaking behavior. Instead, most works hypothesize the role of de-

fects through indirect measurements. A limited body of work has suggested that the alternation between an acceptor and donor configuration of the pair may arise from defect migration that changes the density of defect pairs. For instance, copper vacancies switching between being paired with In_{Cu} versus V_{Se} has already been described to significantly change the implications of defects in CIGS. Gartsman *et al.* was the first to demonstrate the movement of Cu within CIS under applied bias through the use of Cu as a radioactive tracer [81]. Thus bias voltage can change in the distribution of Cu within the depth of the device [82]. Until now, this migration is hypothesized to occur predominantly through the diffusion of V_{Cu}, which are more likely to exist in Cu-poor samples [83–85].

2.3 Treating Defects Through Post-Deposition Treatments

Previously, it was described that the existence of copper vacancies at the CdS interface are important for obtaining high V_{oc}, yet these vacancies are also responsible for metastable device performance under operating conditions such as light soaking. Therefore, finding alternative ways to achieve higher V_{oc} in devices while preventing performance degradation during operation has called for the invention of passivating techniques used during growth. Most notably is the use of alkali post-deposition treatment (PDT) [83, 86]. The process involves the deposition of a thin alkali-fluoride layer, either NaF [87–89], KF [90], RbF [91–93], or CsF [94], at lower substrate temperatures after the growth of the CIS or CIGS is complete.

The use of NaF-PDT was the first treatment considered for CIGS after samples grown on Na-containing soda lime glass substrates were found to have higher V_{oc} and fill factor than those grown on Na-free substrates [95, 96]. Since then, the optimization of NaF concentrations has lead to improvements in efficiency up to almost 20%, as is evidenced in Figure 2.5 [97]. The figure also shows the improvements in efficiency by the previously mentioned approach of Ga-grading. In addition, it demonstrates how the most recent

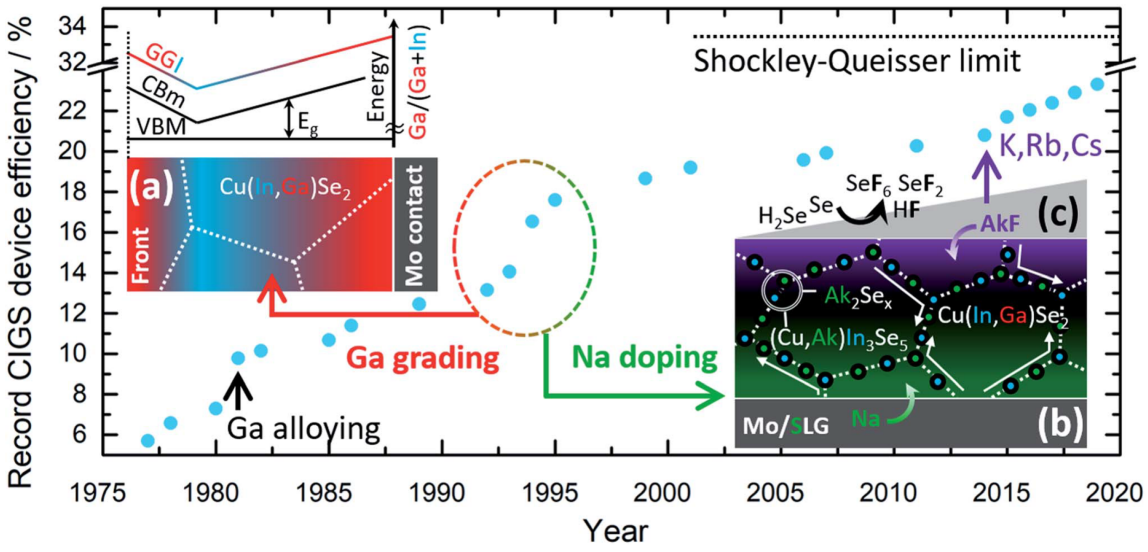

Figure 2.5: Historical progress of CIGS solar cell efficiency and the improvements attributed to: a) Ga-alloying and Ga- grading, b) Na doping, and c) heavier alkali metal post-deposition treatment. Taken from Colombara *et al.* [97].

improvements in efficiency come from heavier alkali PDTs, despite the limited resource availability of these elements. Special focus has looked in detail at KF-PDT, in part due to the scalability of K incorporation over other rarer elements such as Rb and Cs.

A study by Reinhard *et al.* compared the effects of NaF to KF-PDT in CIGS solar cells and found that KF forms a K-rich surface of the CIGS that Na does not [98]. Other work has supported the observation of a K-rich layer or even a K-related secondary phase formed at the surface that is similar to the function of an ODC and may benefit the device V_{oc} through band bending that serves as a hole repellent [99–102]. The formation of the layer may also be dependent on the concentration of ODC prior to PDT [103]. Other work by Handick *et al.* found instead that samples treated with NaF and KF separately both had significant increases in the bandgap, up to 2.52 eV, at the CIGS surface, but this was attributed to the surface being Cu poor rather than the formation of an alkali compound [102]. The formation of an alkali layer at the absorber surface has also been linked to improved CdS coverage [104].

Alkali PDTs have also been researched for the ability to passivate defects within grain boundaries. Thus far, no consensus has been reached on their impact on the device, with some researchers indicating a clear passivating effect [100, 105, 106] meanwhile others suggest there is no evidence of passivation, concluded by studying the grain boundary recombination velocity in samples treated with Na and K [107]. At this point in time, no clear definition of exactly how alkali PDTs benefit device parameters is agreed upon, however, a growing body of work seems to indicate the benefit comes predominantly from improvements in defect passivation within grain cores and at film surfaces.

Despite the scientific debate on the function of alkali elements in CIGS, the use of KF has proceeded as a common treatment in commercial CIGS devices. Flexible modules produced by MiaSolè Hi-Tech Corp. utilize KF-PDT in order to achieve high efficiency, full-size modules. This comes in part due to increasing evidence that the passivation of defects through alkali PDTs improves device stability under temperature and light bias. Work by Khatri *et al.* founded that samples treated with KF-PDT showed improvements in V_{oc} after light soaking [108]. Furthermore, Farshchi *et al.* demonstrated Na migration in CIGS with light soaking, but concluded that the impact of alkali migration is not significant enough to describe trends in carrier concentration [64]. Both works combine to suggest that the composition of the relaxed state, particularly regarding defect densities, is the most indicative of the expected light soaking behavior and therefore remains the primary focus for optimizing devices. This work therefore focuses on the impact of CIGS defects, especially V_{Cu} and V_{Se}, on V_{oc} and efficiency with less focus given directly to the alkali elements as the growing body of research indicates it is intrinsic defects of CIGS that drive device function.

Chapter 3

EXPERIMENTAL APPROACH

In the following section, the various parameters and conditions used for the multi-scale materials characterization methodology are described. First, nano-scale compositional variations can be studied by using correlative X-ray fluorescence and X-ray beam induced current and voltage. Considerations necessary for conducting these measurements are described, including elemental quantification and electrical connections. Then, micro-scale photoluminescence and Raman spectroscopy are described and details are provided on the fitting methods used for each technique.

3.1 X-Ray Fluorescence Microscopy

X-ray fluorescence (XRF) is a technique that provides information on the chemical make up of a sample. It is used across a number of fields, from identifying the materials used in ancient paintings and archaeological artifacts [109, 110], to topics in biology such as plants [111, 112] and insects [113], to understanding the role of metal uptake in cancer cell development [114, 115] and the ion concentrations responsible for hearing loss [116].

The measurement works by using high energy incident X-rays to excite core-shell electrons. In the process, outer shell electrons drop down and emit photons of distinct energies for the atom and the shell levels involved. Figure 3.1 demonstrates the process of an incident X-ray or electron creating a hole and a photoelectron [117]. The hole is then filled by an electron from the outer shell, resulting in a K-beta transition and emitting a fluorescence X-ray with an energy of the difference between the energy of the outer shell and the energy level that was replaced. To the right of Figure 3.1, the X-ray fluorescence spectrum that results from the binning of the energies of the different transitions is shown. One impor-

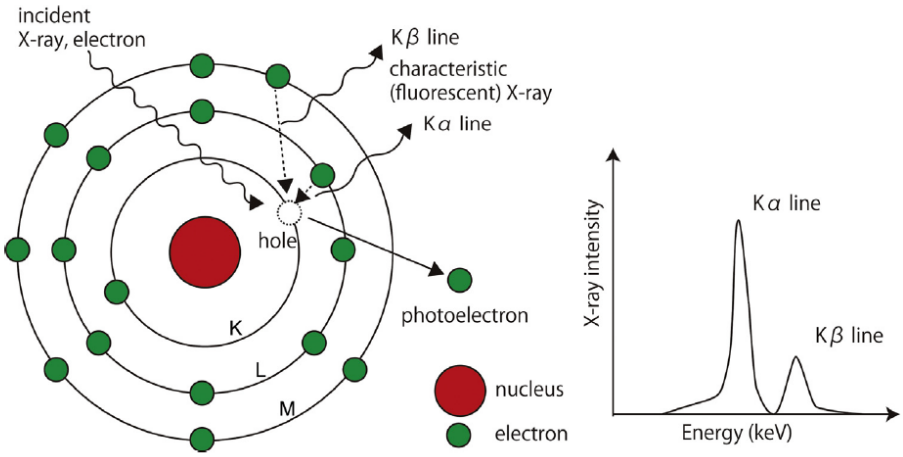

Figure 1 The mechanism of characteristic X-ray generation.

Figure 3.1: A schematic depiction of the X-ray fluorescence process involving incident X-rays and the emission of fluorescent X-rays (left). A simplistic schematic of the XRF spectrum produced plotted as x-ray intensity versus Energy (keV) (right). Taken from Uo *et al.* [117].

tant feature in XRF is the ratio of the heights between the different transitions, called the branching ratio. For instance, in the graphic the K-alpha line is higher than the K-beta.

In XRF measurements of compound materials, the fluorescence process occurs for millions of atoms of different elements each with their own distinct energy lines. The sum of the signal measured at each binned energy value is displayed as a spectrum of fluorescence counts, or the number of photons collected by the energy dispersive fluorescence detector, as a function of photon energy, as was shown before. The spectra are first fit and then compared to a standard measurement to calculate the quantified data. In particular, the first step of fitting fluorescence spectra is critical even for the qualitative analysis of the elements. This is because prior to fitting, counts are binned based on their energy, which becomes a problem when two elements with similar fluorescence transitions are contained in the sample. In this situation, counts may be assigned to the wrong element. An example of an integrated XRF spectrum of a CIGS solar cell is shown in Figure 3.2, modified from Nietzold *et al.*[118]. The white line is the experimental results and the green line is the

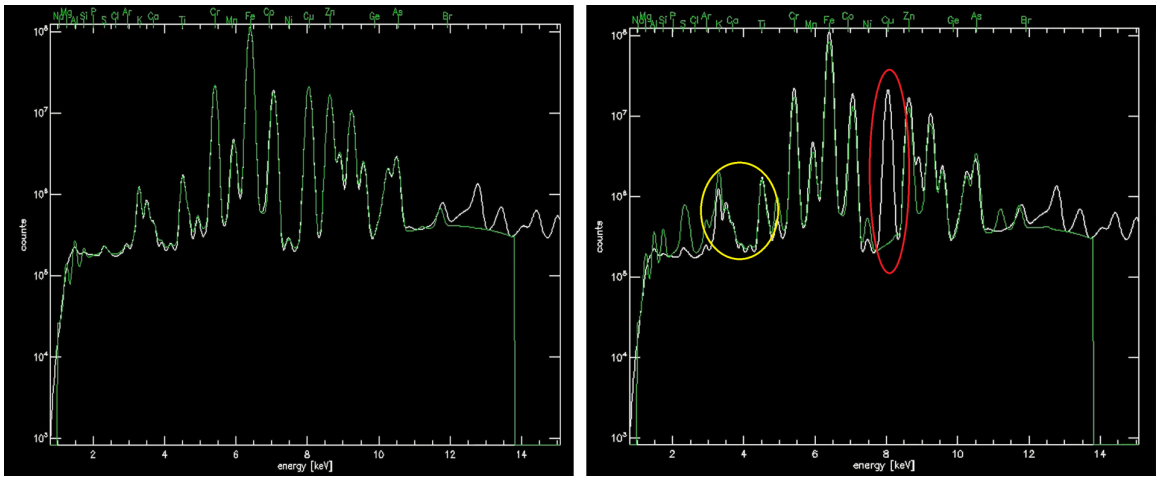

Figure 3.2: An example integrated XRF spectrum is shown, with the various elements marked at the top. The white lines represent the experimental data and the green line is the results of the fitting procedure. The figure on the right demonstrates an example of incomplete or inaccurate fitting parameters being implemented.

results from a fitting procedure used for quantifying the data.

The process of quantifying elemental concentrations from X-ray fluorescence (XRF) measurements translates fluorescence intensity counts into elemental mass concentrations (e.g. $\mu g/cm^2$). The fitting procedure is done by comparing the XRF counts to the counts produced for a sample with known concentration, called a standard. The standard with known elemental concentrations is measured in the exact same geometry and environment as the samples are, and the XRF spectra are then fitted to relate fluorescence counts to the known concentrations. Data acquired from the Advanced Photon Source at Argonne National Laboratories can be fit using the proprietary software, Maps [119]. The step-by-step procedure on how to do so has been written and published elsewhere [118].

3.1.1 Synchrotron XRF Procedure

In this work, X-ray microscopy measurements paired X-ray fluorescence (XRF) to provide chemical information with X-ray beam induced current and voltage (XBIC and XBIV, respectively) to provide information on device performance. The measurements were com-

pleted at end stations 2-ID-D and 26-ID-C of the Advanced Photon Source of Argonne National Laboratory with a focused beam of approximately 150 nm or 40 nm at full-width half-maximum (FWHM), respectively. Incident energies of 12.8 keV (above the Se_K edge), 10.4 keV (above the Ga_K edge), and 9.0 keV (above the Cu_K edge) were used to best capture all of the elements of interest from the devices. Multiple maps of different areas were taken for each sample studied. The map parameters used were on the order of 10-20 μm x 10-20 μm maps, 50-150 nm step size, 1 second dwell time. The average data produced per map were approximately 10,000-20,000 data points.

The set up for XRF/XBIC/XBIV mapping involves determining the geometries for the incident X-ray beam and the XRF detector and forming the correct electrical connections. Figure 3.3 shows an example of a CIGS mini-module being studied at the end station 2-ID-D. The incident X-ray is focused by a series of lenses or Fresnel zone plates that allow a broad X-ray beam to be focused down to a record of 10 nms [120]. The geometry of the incident angle, sample surface, and detector geometry need to be optimized to consider a number of things. Firstly, the spot size of the beam on the sample is most narrow when the incident beam is normal to the surface - tilting the sample thus widens the projection of the beam. Next, the angle of the detector must be optimized for capturing the most of the exiting fluorescence signal from the sample. The ideal geometry would be if the detector could be in the same place as the incident beam, so that it could capture the full wide angle of signal. However, as this is not physically possible, the detector is generally placed between 43-47 degrees.

During the measurements, the x-y stage or the X-ray optics move to map the region of interest (ROI). Previously, mapping the sample was done using step scan, the process where the positioner stage moves to the next pixel and pauses to measure. In recent years fly-scan mode has been added to some beamlines, which allows the stage motor to continue to move during simultaneous acquisition by the detector. This method of data acquisition

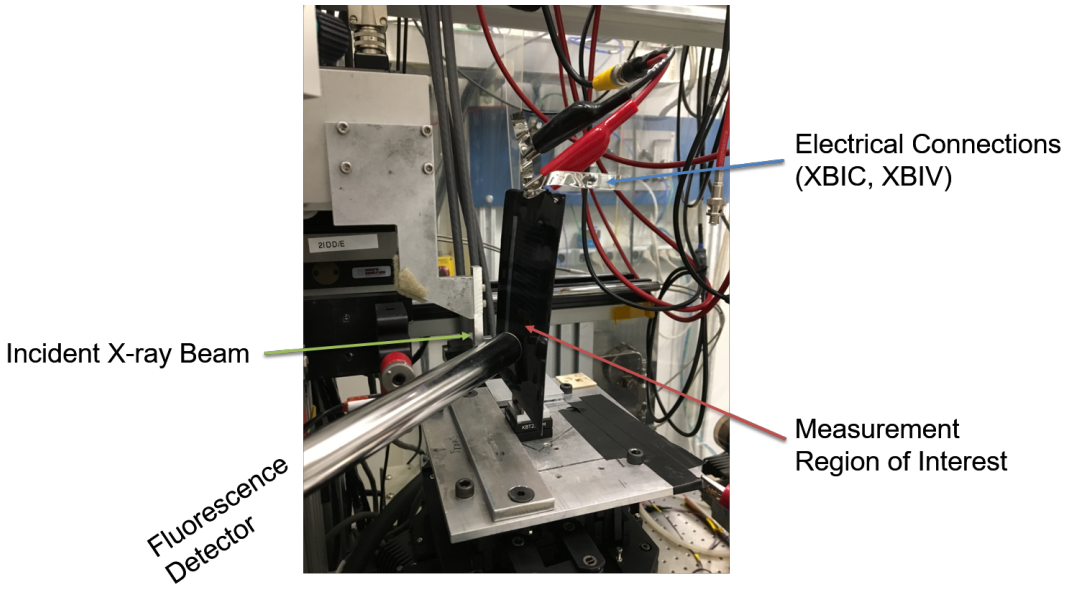

Figure 3.3: Photograph of a CIGS mini-module mounted for correlative XRF/XBIC/XBIV measurements at the end station 2-ID-D of Argonne National Laboratory. Labeled are the X-ray optics for the incident beam, fluorescence detector, and the sample and its wiring.

has allowed for significantly faster measurement speeds and in turn, has made larger map sizes more feasible [121, 122]. With mapping, an XRF spectrum is generated at each map pixel, resulting in oftentimes thousands of individual spectra.

The high energy of synchrotron X-rays results in a high penetration depth in thin film solar cell stack structures. In the case of CIGS thin films, the commonly used incident energies mentioned before (12.8 keV, 10.4 keV, and 9.0 kev) are all able to penetrate through the entire stack structure of a CIGS solar cell. This results in chemical information for all the materials, including the absorber, the CdS buffer, the Mo back contact, and the ZnO transparent conducting oxide. The challenge is that each additional layer provides the opportunity for outgoing X-rays to be attenuated. Lower energy fluorescence photons are particularly susceptible to absorption within the stack. This is even more so a concern for L- and M-line transitions, but also for transitions that are significantly lower in energy than the incident X-ray energy such as lower Z elements like Na and K.

Figure 3.4 shows the calculated attenuation of the four CIGS elements within the depth

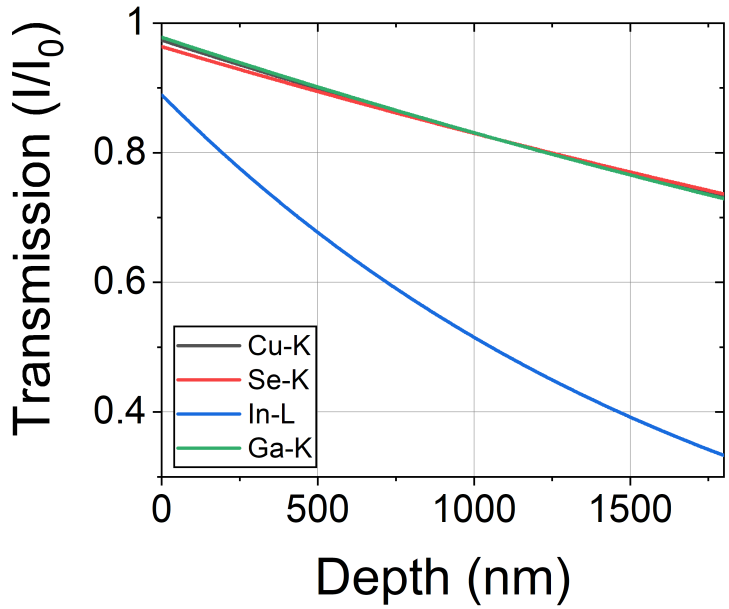

Figure 3.4: Calculated transmission ratio of the four CIGS elements for each of their measured energy lines (note the In-L is studied in all experiments) as a function of depth in the absorber. Deeper into the absorber signifies towards the Mo back contact and away from the CdS interface.

of the absorber of approximately 1.8 µm. From the figure, the loss in signal transmission of all the elements is increased the deeper in the absorber depth (meaning further from the sample surface of the incident X-ray beam). The In signal clearly suffers more transmission losses than any of the other elements. This is because at all of the possible incident energies, only the In-L lines are measurable. L-lines are of lower energy and have many more possible transitions than for K-shell transitions. This not only makes elements studied in fluorescence using their L-lines more difficult to measure, but they are also more difficult to fit. As there are many more L-shell transitions, the branching ratios between all of them need to be optimized for the fitting to be done accurately [123]. Figure 3.2(right) shows an example of non-optimized fitting of In-L lines, circled in yellow. The red circle instead shows an example of an entire element being excluded from the fitting algorithm, in this case Cu was excluded.

3.1.2 X-ray Beam Induced Current and Voltage Considerations

All of the samples are connected for X-ray beam induced electrical measurements to directly correlate the XRF and electrical results. The measurement of XBIC is similar to that of J_{sc} where incident light generates electron-hole pairs and the charge collection is studied. Figure 3.5 shows the set up for an XBIC measurement of a perovskite solar cell as an example. Also shown is the figure is TEY, or total electron yield, which is the ejection of surface layer electrons (in the case of the figure, from the TCO) occurring so that the sample can maintain charge neutrality [34].

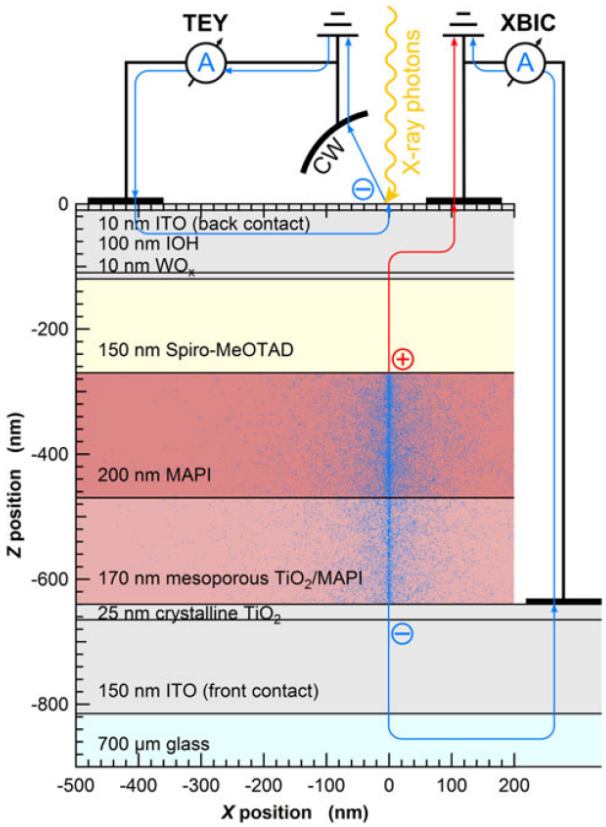

Figure 3.5: Set up of an X-ray beam induced current (XBIC) measurement (right circuit) and of a total electron yield measurement (TEY) in a perovskite solar cell. The blue dots represent the end-of-trajectory of the secondary electrons generated in the solar cell by the incident X-ray beam (in this case, 9 keV). Taken from Stuckelberger *et al.* [34].

Being that the TEY is measured from the surface of the sample, the positive and nega-

tive connections of the electrical measurements are critical to consider in order to prevent one from measuring TEY instead of XBIC/XBIV. To address this, the sample surface must always be grounded, however, depending on the orientation of the p-n junction to the incident beam determines whether the output signal is positive or negative. In the case of CIGS, the orientation is almost always that the n-type CdS is closer to the sample surface than the p-type CIGS, meaning that the XBIC signal should be positive when measured by the current amplifier.

Recent work has studied the use of a lock-in amplifier to improve the signal-to-noise of the nano-scale electrical measurements [124]. Figure 3.6 shows an example of an XBIC map of a CIGS solar cell measured for direct signal and measured using lock-in amplification. The lock-in map is more clear, with more sharply defined features. The map also has some measurement artifacts removed, such as horizontal lines. This is a function of the lock-in amplifier, which applies a low-pass filter to remove signal frequencies below some user-defined value. Careful consideration is required for determining the low-pass cut-off frequency because it is also related to the charge-carrier lifetime and the measurement frequency (dwell time).

In addition to the low-pass filter, the frequency of the optical chopper helps to define the signal quality achievable. In an ideal situation, the optical chopper frequency would be able to match the frequency of the X-ray beam. However, the beam frequency is on the order of 10^{17} Hz and achieving such frequencies with an optical chopper is currently not feasible. As a rule of thumb, the frequency of the low-pass filter should be one order of magnitude lower than the frequency of the optical chopper, and the sampling rate should be one order of magnitude below the low-pass filter frequency.

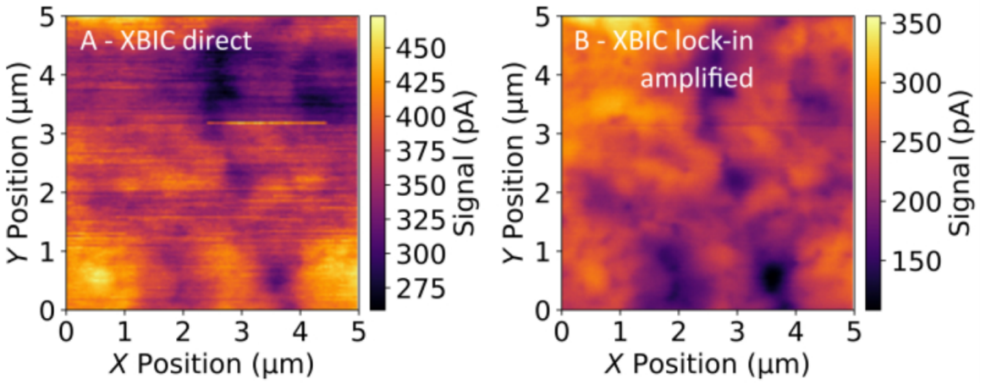

Figure 3.6: XBIC maps of a CIGS solar cell measuring the direct XBIC signal (A) and the XBIC signal after lock-in amplification is applied (B). Taken from Ossig *et al.* [124].

3.1.3 Image Analysis of Map Data

Figure 3.7 shows an example of the XRF and XBIC maps that are produced by correlative XRF/XBIC/XBIV [125]. There is a watershed overlayed (black lines) that are used to define grain boundaries. From the maps, the spatial correlation of the elements and the XBIC signal is clearly defined. There is an inverse relationship found for In concentration to XBIC signal and a positive correlation was found for Cu and Ga to XBIC. The results indicated that areas of higher performance are relatively Cu/Ga-rich and/or In-poor. It also concluded that grain boundaries of CIGS do appear to be Cu-poor.

The limitation to the findings from West *et al.* is that the samples used were a single grain thick, meaning that no CIGS grains were stacked on top of each other. This made observations of boundaries more clear and allowed for a strong linear correlation between XBIC and composition. Commercial devices, however, have thicker absorbers and are not necessarily grown with enough control to prevent small crystallites from forming. Thus, the XRF measurements become convoluted when looking at multiple grains stacked on each other and linear relationships between XBIC and composition are often very weak.

One proposed method to address this challenge is the use of image segmentation to study areas of high and low signal and identify any compositional variations between the

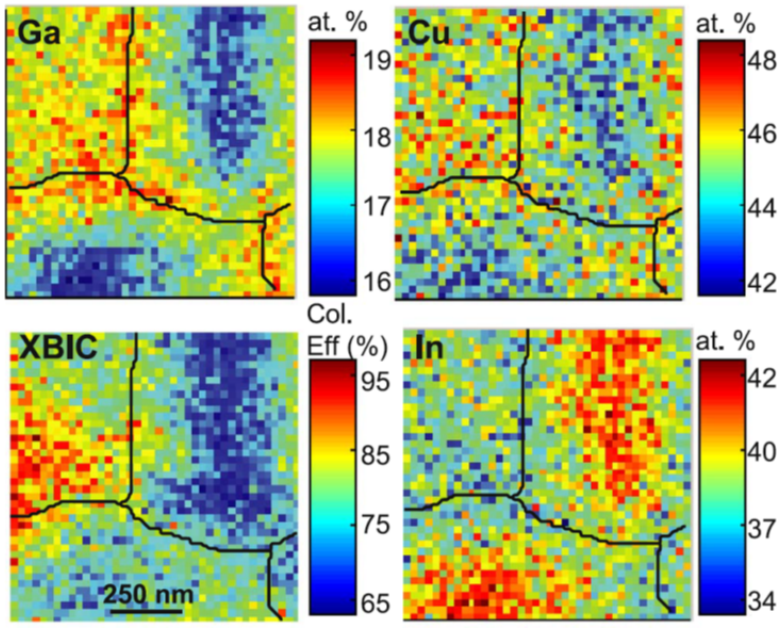

Figure 3.7: Example results of Ga, Cu, and In concentrations of CIGS solar cells measured by XRF at the Ga-K edge (10.4 keV) and the correlative XBIC measurement. The overlaid lines are to show the result of watershed image processing to approximate grain boundary locations. Taken from West *et al.* [125].

regions [126]. K-means clustering has been studied as an effective way to simply segment data into a set number of groups input by the user. Figure 3.8 shows the results of clustering the data from XBIC and the data from Se maps for $CuInSe_2$ (CIS) solar cells. The original maps are shown for XBIC (Figure 3.8(a)) and Se (Figure 3.8(b)) and the following two columns show the results for clustering into two groups (middle column, Figure 3.8(c,d)) and into three groups (right column, Figure 3.8(e,f)). Immediately, with the use of two groups, it is clear that the group assignments of the pixels are significantly different depending on the map that is used for the clustering. Being that in the case of solar cells, we seek to identify the characteristics that define poorly performing areas, it can be more beneficial to use the XBIC or XBIV maps for clustering. This allows for the chemical information describing high and low performing areas to be isolated and directly correlated to the performance.

In addition to needing to increase throughput speeds of the analysis, many maps re-

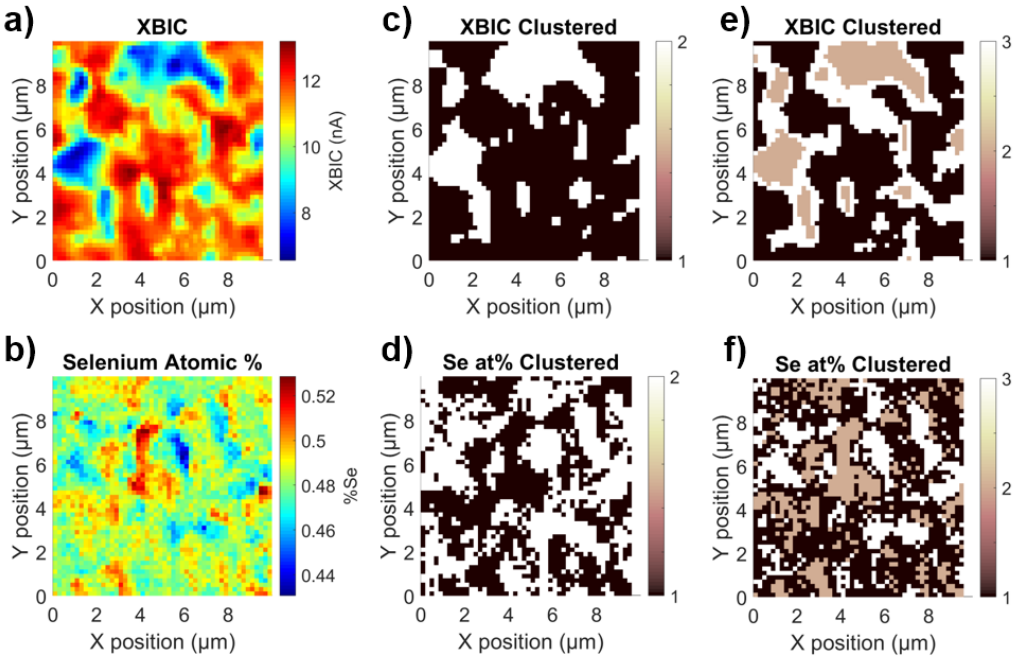

Figure 3.8: Example results of clustering XRF and XBIC data, shown for $CuInSe_2$ solar cells. (a,b) Show the original maps for XBIC (a) and Se (b). (c,d) Show the results of K-means clustering using 2 groups, and (e,f) using 3 groups, when the XBIC map is clustered (c,e) or the Se map is what is clustered (d,f).

sulting from correlative XRF/XBIC/XBIV need additional image registration that can be extremely time consuming and requiring a high degree of accuracy. This is because XBIC and XBIV maps are unable to measured simultaneously. Even maps repeated directly one after the other can be slightly shifted from a number of sources, including the accuracy on the nano-scale of the stage positioner to return to the exact same starting point, vibrational noise from the stage, and from slight movement of the sample as the wires are changed from one electrical configuration to the other. Shifts in the map positions make statistically significant linear relationships even more difficult to identify. Improved image registration is therefore a component of the future work proposed.

3.2 Micro-Photoluminescence and Raman Spectroscopy

The correlative XRF approach is complimented by laser-based techniques photoluminescence (PL) and Raman spectroscopy for their abilities to probe: 1) different length scales and 2) additional, but related, materials properties. If proper considerations are taken to create measurement fiducials, these measurements can even be directly correlated to XRF when the same areas are measured. In this work, a green 532nm laser was used in order to be sensitive to the absorber surface. Due to the absorption coefficient of CIGS at 532 nm, the calculated penetration depth of the laser is approximately the top 80-100 nms of the film [127].

Both PL and Raman are done using an x-y stage for mapping. The laser is focused through optical microscope objectives down to 1 μm spot size and maps of approximately 20 μm x 20 μm were measured for the samples. The dwell time and laser power used is entirely dependent on the absorption of the layers above the CIGS (CdS, TCO) and the power density that is safe for the sample to prevent laser bleaching [128]. However, measurements within sample sets were always set to the same laser power for the appropriate comparison between the results.

Photoluminescence spectra describe the recombination in a semiconductor. The most intense peak is representative of the band to band transition, or bound-to-free, which is related to the bandgap of the material. Increases in the full width half maximum (FWHM) or the appearance of additional peaks beneath the bandgap energy indicate the existence of defects. For instance, in Figure 3.9, which shows PL spectra of CIGS samples with different annealing temperatures, there are two peaks below the bandgap that are due to defect states [129]. The peak to the right of the band-to-band (1.17 eV) at 1.22 eV is from a wider bandgap alloy of CIGSSe (Se site alloyed with S from the CdS). Fitting the peaks with multiple Gaussian functions can obtain their amplitudes and can suggest the relative

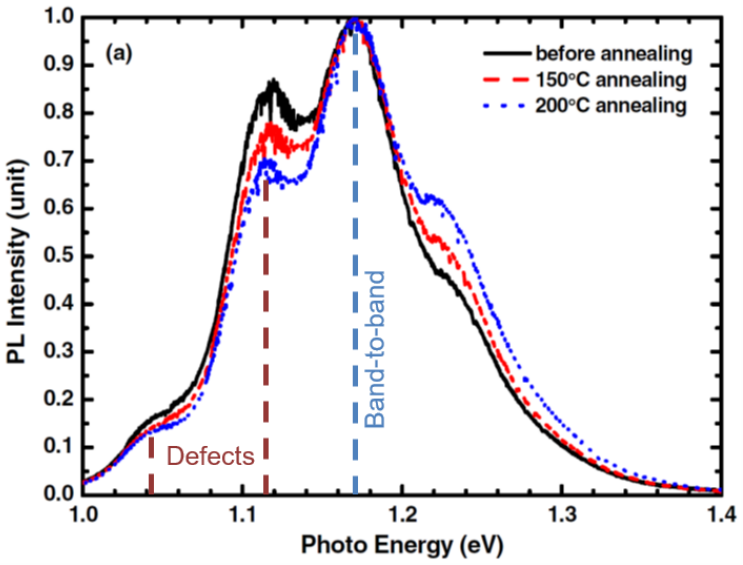

Figure 3.9: PL spectra of a CIGS solar cells fabricated with different annealing temperatures, including a sample that was not annealed (black). The peak at 1.17 eV represents the band-to-band transition of the CIGS bandgap for 30% Ga incorporation. The peaks at 1.05 and 1.12 are from defect states. Taken and modified from Chen *et al.* [129].

concentrations of certain known defect peaks.

The addition of temperature-dependent and injection-dependent PL studies provides additional information on the defect states present in the films. For instance, Guthrey *et al.* evaluated the temperature and injection level dependence of cathodoluminescence spectra (CL; similar in interpretation to PL) in KF treated CIGS devices [130]. The peak position of the KF treated sample was found to be non-uniform between grain boundary and grain interior regions, with boundaries exhibiting a blue shift in energy to lower peak positions in eV. More importantly, both techniques (temperature and injection level) demonstrated an increase in band-impurity recombination for the KF treated sample that was proposed to be responsible for the blue shift in the peak position.

Raman spectroscopy is often done in tandem with PL measurements because it can make use of almost all of the same components of the PL tool. Raman spectra can be used to provide information on the crystal structure [131] and grain orientations [132, 133]. The measurement studies the material interactions in the form of vibrational transitions that

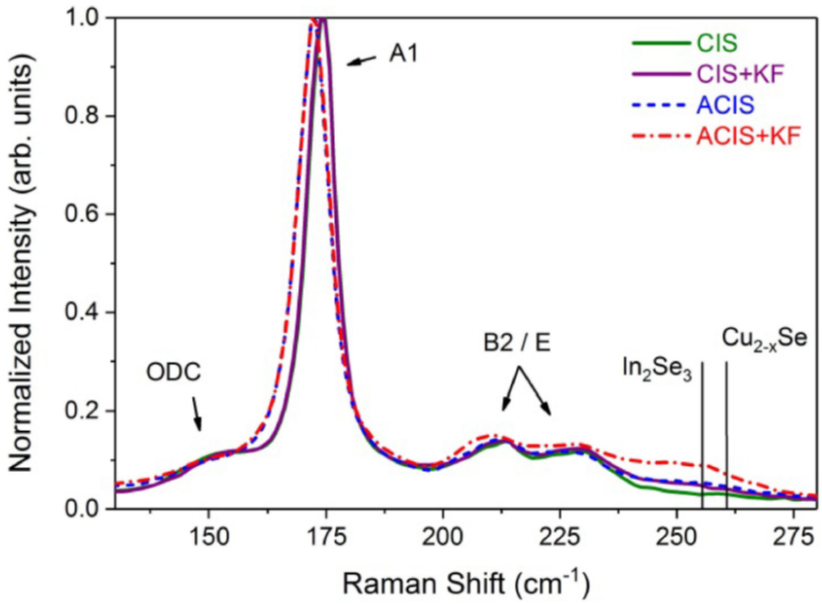

Figure 3.10: Raman spectra of CIS samples alloyed with Ag and treated with KF post-deposition treatment. The various Raman modes observed are labeled including the A_1, the ODC peak, and the E/B_2 modes. Taken from Valdes *et al.* [135].

occur as matter interacts with monochromatic light [134]. The type of vibrations include symmetrical stretching of bonds, asymmetrical stretching, and bending, each of which have distinct frequencies depending on the atoms and bond lengths involved.

In CIS, the Raman mode with the highest scattering cross section is the A_1 vibration that occurs from the stretching of Se around the resting Cu and In cations [131, 135]. The same vibration exists for ordered defect compounds, such as the Cu-poor structures $CuIn_3Se_5$ and $CuIn_5Se_8$, however with a different frequency due to the change in the atoms around the stretching Se atoms. Specifically, the ODC structure is distinguished in Raman by the A_1 mode existing at a lower wavenumber [79, 136–138]. This can explained by the reduction in Cu atoms paired with increased In atoms in the structure that results in an increase in the atomic weight about the Se atoms, following the inverse relationship of reduced mass to frequency described in [134].

Figure 3.10 shows an example of the Raman spectra commonly produced for CIS solar

cells. The labeled spectra show the A_1 mode as well as the ODC peak occurring at lower wavenumber, usually around 152 cm^{-1}. It also shows the E/B_2 mode that represents the asymmetrical stretching of the Cu and In atoms around the Se atoms [133, 137]. The peaks in Raman can also be fitted, most often by a Lorentz function, in order to obtain the peak amplitude of a certain mode to calculate the relative concentrations of certain modes or phases present.

Also similarly to PL, temperature-dependent Raman spectroscopy measurements can be used to help resolve additional peaks currently not observable with room temperature measurements. Mishra *et al.* for example showed that temperature-dependent Raman spectroscopy was capable of identifying additional vibrational modes in CdS at low temperatures [139]. These modes were found in addition to the main CdS peak anticipated at 300 cm^{-1}. Future work on CIGS films may therefore include temperature and injection dependent PL and Raman to investigate in greater detail the structure and electrical properties.

Chapter 4

$CUINSE_2$ SOLAR CELLS

In this section, the impacts of post-deposition treatment (PDT) and Ag-alloying are studied in the absence of Ga. In particular, the characterization approaches from Chapter 3 are used to investigate the incorporation and impact of the two treatments used to increase efficiency in $CuInSe_2$ solar cells on glass substrates. The objective of this work is two-fold: it firstly allows for the study of a simpler system with fewer potential defects and secondly, CIS is becoming an increasingly interesting material for its potential use in tandem solar cells.

Being that the bandgap of $CuInSe_2$ is approximately 1eV, the absorber material has the potential ability to serve as the bottom cell in tandem applications [19, 140–143]. One of the added benefits of CIS in comparison to currently accepted bottom cell materials such as silicon is that while research on flexible Si is on-going and progressing, flexible CIGS devices based on stainless steel or polymer substrates are already commercially viable [144]. Beyond that, as mentioned in Chapter 2, CI(G)S films have tunable bandgaps by means of Ga-alloying and therefore allowing them to be used as different or multiple terminals in tandem solar cells.

4.1 Sample Preparation and Background

Samples were fabricated by collaborators at the University of Delaware using 3-stage co-evaporation [136, 145]. Half of the samples were co-evaporated with Ag to produce a Ag/(Ag+Cu) (AAC) ratio of 0.20, which was validated by X-ray fluorescence. After the absorber deposition, the samples were cooled to 350 °C, and half the samples received an in-situ PDT with $\sim$7.5 nm of KF deposition in a Se atmosphere, similar to the process described in [146]. The resulting four samples are assigned the following names: CIS,

ACIS, CIS+KF, and ACIS+KF, similarly to the samples studied in [147]. The devices were completed with CdS (50 nm), i-ZnO (50 nm), ITO (150 nm), and a Ni-Al grid.

Table 4.1 shows the bulk J-V characteristics measured for sister samples of these devices. The J_{sc} increases slightly with Ag-alloying, as is expected due to silver's ability to reduce defect density in the absorber by lowering the alloy's melting temperature [148, 149]. The V_{oc} increases in the CIS+KF sample as expected due the expectation that KF can passivate defects [90, 100, 106, 150] and/or create a surface layer with a lower valence band maximum (VBM) that serves as a hole repellent at the CdS interface . However, an increase in V_{oc} is not observed for the ACIS+KF sample, which shows that the addition of KF to ACIS significantly reduces the V_{oc} by over 100 mV.

Table 4.1: JV Characteristics of Samples Studied Under Simulated AM 1.5G at 25°C

Sample	J_{sc} (mA/cm^2)	V_{oc} (mV)	FF (%)	η (%)
CIS	36.9	437	67.8	10.9
CIS+KF	36.7	479	72.6	12.8
ACIS	37.1	431	70.7	11.3
ACIS+KF	37.2	331	63.8	7.8

Thus, the main goal of this chapter is to form an understanding of the reduced V_{oc} and FF when Ag and KF are used in combination. Studies on sister samples by Valdes *et al.* have demonstrated that the application of a KF-PDT influences the growth of the CdS layer [136] and that it drives the surface to become further Cu-poor and Ag-poor, in the case of the Ag-alloyed CIS [151]. This indicates there is a change in the compositional distribution of the films when exposed to the KF, the mechanism of which is unclear. Most recently, Sopiha *et al.* found by calculation that Ag-alloying can make the CIGS alloy unstable, which can result in film decomposition during the additional temperature step of PDT [152]. These findings suggests the primary concern in the case of Ag and K incorporation is the impact it has on film homogeneity and the connection that inhomogeneity can have on electrostatic potential fluctuations that hinder V_{oc} as outlined by Siebentritt [18].

Samples first studied using correlative XRM at the end station 2-ID-D of Argonne National Laboratory. Three maps per sample were taken, each with dimensions 10 μm x 10 μm with a spot size of 150 nm at the Se edge. Data was obtained for both XBIC and XBIV done in sequential order.

Synchrotron X-ray diffraction was done at beamline 11-3 of the Stanford Synchrotron Radiation Lightsource (SSRL), a division of SLAC National Accelerator Laboratory to validate the existence of phases hypothesized from Raman spectroscopy. Two-dimensional scattering data were collected using a Rayonex MX225 detector in a grazing incidence geometry with the X-ray beam held at an incident angle of 3°. Images were calibrated using a LaB6 standard and integrated between 10°¡ χ ¡ 170° (χ is the polar angle) using GSAS-II [153]. A spot size of 150 μm x 50 μm was used with an incident wavelength of 0.9744 Å. Six separate measurements were taken of areas between two metallization lines on the samples.

4.2 Studying Compositional Variation and its Relation to Performance

Examples of the XRF maps taken are shown in Figure 4.1 for the ACIS+KF sample. The low concentrations of Ag are evident by the noisy appearance of the map in Figure 4.1(a). Despite the low signal-to-noise of the Ag, some clustering is still observable. From the maps, it seems as though the Cu, In, and Se are co-located. This is a factor of thickness variation rather than true compositional distribution, demonstrating the importance of normalizing the maps by the total elemental concentration. Normalizing the data for all of the samples and maps, it is difficult to qualitatively determine any compositional variations between the samples. Therefore, a K-means clustering algorithm was applied to the maps of XBIC for each sample to separate the data into four groups: high XBIC, medium-high XBIC, medium-low XBIC, and low XBIC.

The XRF data is then taken from the index locations of the highest and lowest XBIC

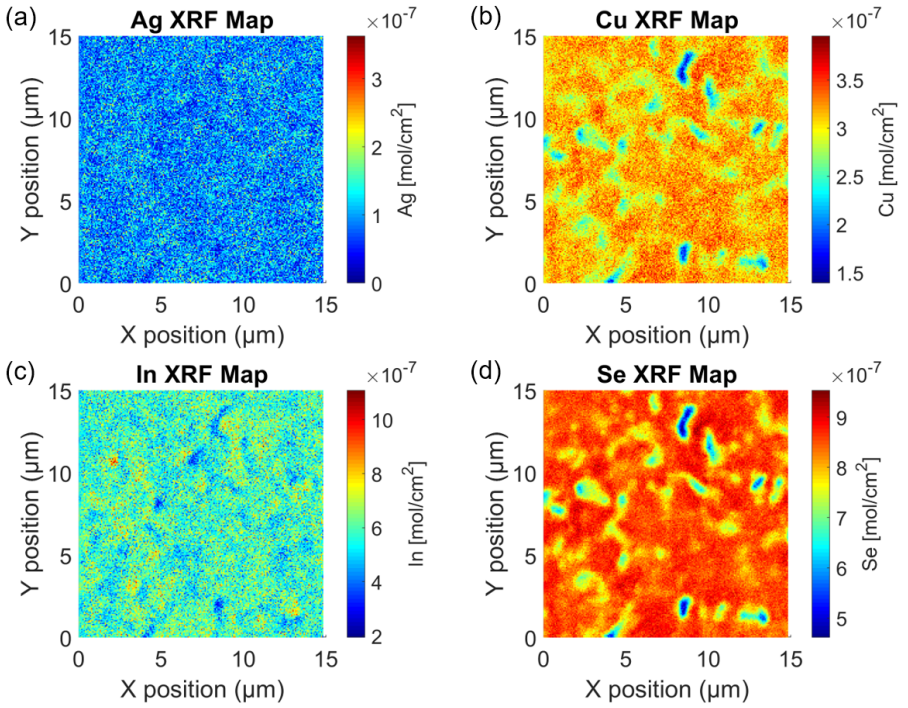

Figure 4.1: XRF maps for: (a) Ag, (b) Cu, (C) In, and (d) Se concentration for the ACIS+KF sample.

regions in order to evaluate the compositional difference between the two extremes in performance. The distributions of these data are shown in Figure 4.2. The data is shown as atomic ratio to correct for the influence of thickness variation as aforementioned. The split violin plots show the side-by-side comparison of the elemental information from the highest (light shading) and lowest (dark shading) XBIC areas of each sample and include the median (long dashed line) and the inner-quartile region (25^{th} to 75^{th} percentile of data, shown as short dashed lines).

The atomic ratio of Ag is included in Figure 4.2(a) in order to validate: 1) the correct concentration of Ag incorporation and 2) comparable and consistent Ag incorporation for both the ACIS and ACIS+KF sample. The data show that the Ag/[Ag+Cu] ratio is approximately 0.2 for both devices and the variation between the high and low XBIC groups is minimal. Additionally, the variation in overall Ag concentration and distribution is sim-

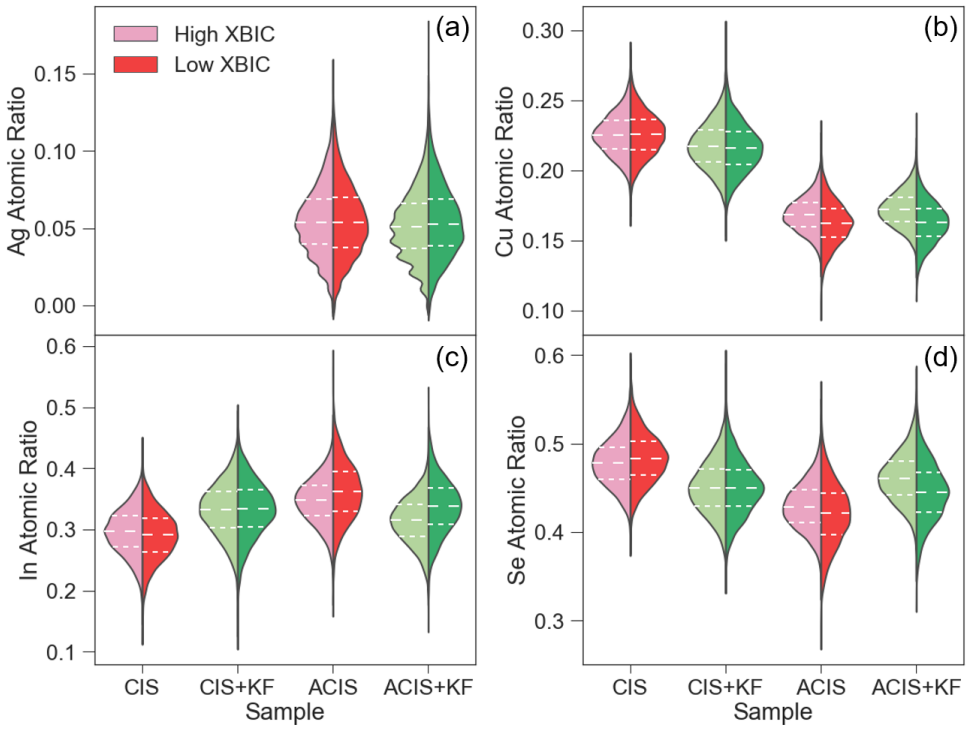

Figure 4.2: Violin plots of the XRF data of atomic ratio for (a) Ag, (b) Cu, (c) In, and (d) Se for the compositional data for the highest XBIC data (light shading) and the lowest XBIC data (dark shading) segmented by using a K-means clustering algorithm set to four groups. Dashed lines represent the inner-quartile range, and the center line represents the median.

ilar between the ACIS and the ACIS+KF. The consistent Ag concentrations for low and high XBIC in both Ag-containing samples confirms that changes in the other concentrations are not driven by variations in Ag. It also indicates that the distribution of Ag is not negatively related to performance variations in the samples. The wavy-features in the high XBIC cluster data of the Ag atomic ratio (Figure 4.2a, light red and light green for ACIS and ACIS+KF respectively) indicate that the Ag in these areas is grouped into finite bins, potentially due to segregation.

The remaining three split violin plots in Figure 4.2b-d show the atomic ratios for Cu, In, and Se between the high and low XBIC areas. The Ag-free samples demonstrate minimal variation in the median and inner-quartile boundaries for the three elements. In particular, the CIS+KF sample shows the least amount of compositional variation between the two

performance groups. This indicates a high degree of homogeneity between the two and suggests that compositional inhomogeneity is not dominating device performance in this sample. On the other hand, the Ag samples show that areas with lower XBIC intensity are richer in In and poorer in Cu and Se compared to the high intensity areas, especially observable in the ACIS+KF. This is seen as a difference of approximately 1 at% for the low XBIC areas of the ACIS and ACIS+KF. Note that there is also a degree of variability in the median In and Se concentrations from sample to sample, with a range in the median atomic ratio of approximately 7 at%. This is characteristic of a redistribution of elements through the depth of the absorber, as described by West *et al.* [154].

These results indicate there is a high degree of compositional inhomogeneity particularly in the ACIS+KF sample. Instead, the CIS+KF sample appears the be the most compositionally uniform, while also demonstrating the highest V_{oc} and efficiency (from Table 4.1). This is not surprising as film inhomogeneity is often cited as being both detrimental, but also necessary in CI(G)S devices [25, 52, 125, 155]. Inhomogeneity results from the ability for $Cu(In_{1-x}Ga_x)Se_2$ to deviate from stoichiometry through the formation of compensating defects. It is then the defects that are responsible for the resulting device performance.

The increase in inhomogeneity in the ACIS+KF significant and is further evidenced by studying at the spatial distribution of the XBIC signal provided in Figure 4.3. From the maps, the first clear observation is that the overall signal for the ACIS+KF is much lower compared with the three remaining samples. The map topology and feature sizes appear consistent for the three samples: CIS, CIS+KF, and ACIS. The ACIS+KF instead shows low signal regions of much larger size, for example the dark feature centered near (5,5) of Figure 4.3(d) that is a much larger, low performing feature than any features found in the other samples. These XRF data of these dark features are what seen in the violins for the low XBIC in Figure 4.2. The fact that the ACIS+KF is more compositionally inhomo-

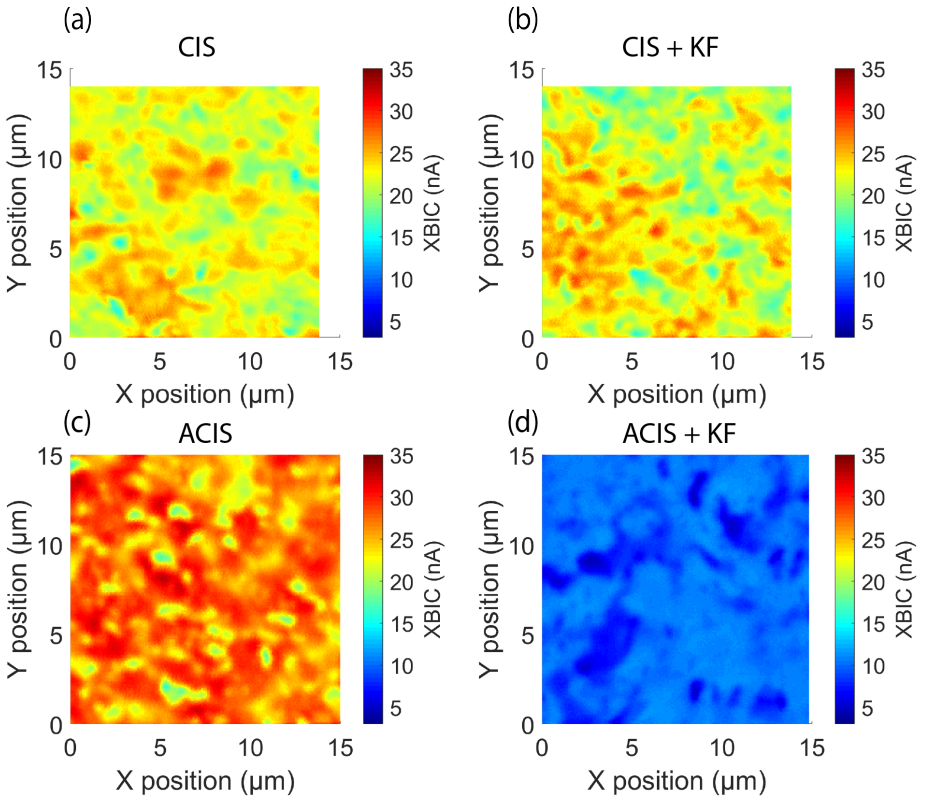

Figure 4.3: XBIC maps for: (a) CIS, (b) CIS+KF, (C) ACIS, and (d) ACIS+KF. All maps are shown on the same scale for comparison. Note that figures (a) and (b) were map sizes 14 μm x 14 μm compared to the 15 μm x 15 μm maps in (c) and (d).

geneous and that the inhomogeneity is found in large areas of low performance begins to indicate a potential problem in the sample that may be capable of describing the significantly reduced V_{oc} observed.

The nature and volume of these features can be demonstrated in a statistical manner by the use of violin plots that contain information of both XBIC and XBIV signal for all of the maps measured per sample. Figure 4.4 shows the distributions of the electrical signal of the four samples. Most noticeable is again the contrast between the CIS+KF and ACIS+KF samples. The CIS+KF sample has the widest distribution in both XBIC and XBIV, followed by similar widths for the CIS and the ACIS. The three samples also show normal distributions of their data, again in both the XBIC and XBIV. The ACIS+KF instead has a narrow distribution around the mean, but then a large tail of data toward lower signals

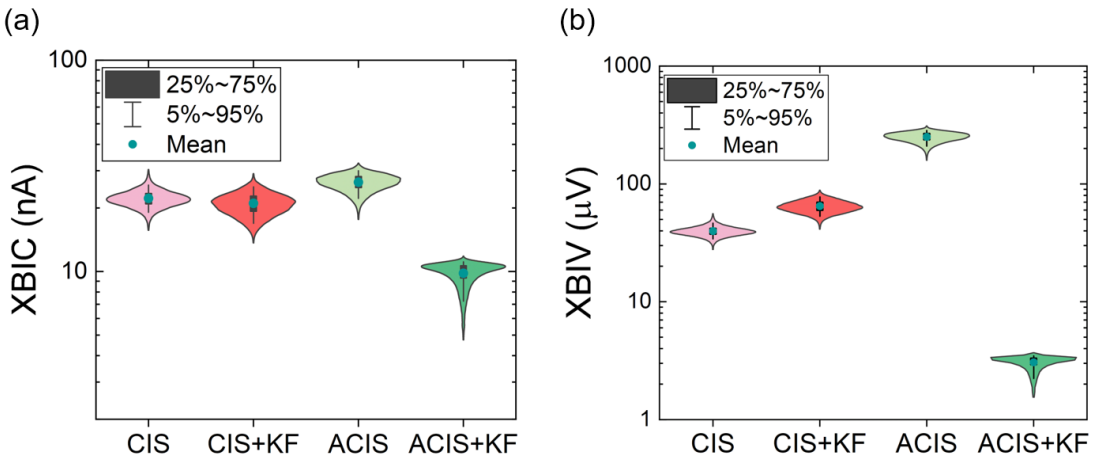

Figure 4.4: Violin plots of the distributions of the XBIC (a) and XBIV (b) signal shown on a y-log scale for comparison of the violin shapes.

in both the XBIC and XBIV. The data that falls in the tails of the violin plots are the features discussed before in reference to Figure 4.3(d). This demonstrates not only the magnitude of the features, that they are low enough in intensity to create such a long tail in either signal, but also the volume, seen by the lateral width of the violin plot at the tail.

The second noticeable trend in Figure 4.4 is the mean signal intensity of both XBIC and XBIV is lowest in the ACIS+KF. The observation that this occurs in both the XBIC and XBIV indicates that the sample itself had some issue with series resistance. Often, this can happen from an issue with the sample wiring that is done for the nano-scale electrical measurements. The Ag paint that is used to attach the metal wires to the sample surface has also been observed to cause local shunting upon application. Thus, in this situation, it is not reasonable to directly compare the signal intensities from sample to sample. However, the distribution of the data and the relative changes within maps are still meaningful and comparable.

The results from correlative XRF/XBIC/XBIV have so far indicated that the low V_{oc} sample, ACIS+KF, is compositionally and electrically inhomogeneous. By relating the

high and low XBIC data to composition, the inhomogeneity of the ACIS+KF was identified as being Cu- and Se-poor in areas of reduced XBIC signal. This clearly demonstrates that the use of Ag and K together results in increased film inhomogeneity. However, inhomogeneity alone is not necessarily capable of explaining the observed V_{oc} loss between the CIS+KF and the ACIS+KF of over 100 mV. To better understand the impact of Ag and K on reducing the V_{oc}, additional materials characterization was done to investigate the impact of the KF passivation.

4.3 Validation of Proper Passivation with KF-PDT

One possible explanation for the lower V_{oc} observed in the ACIS+KF is that the existence of the Ag that is alloyed into the Cu-cite perhaps prevents or alters the manner in which the K is added to the absorber to passivate defects. Photoluminescence mapping of 5 map areas, each 20 µm x 20 µm, per sample provides statistical as well as spatial infor-

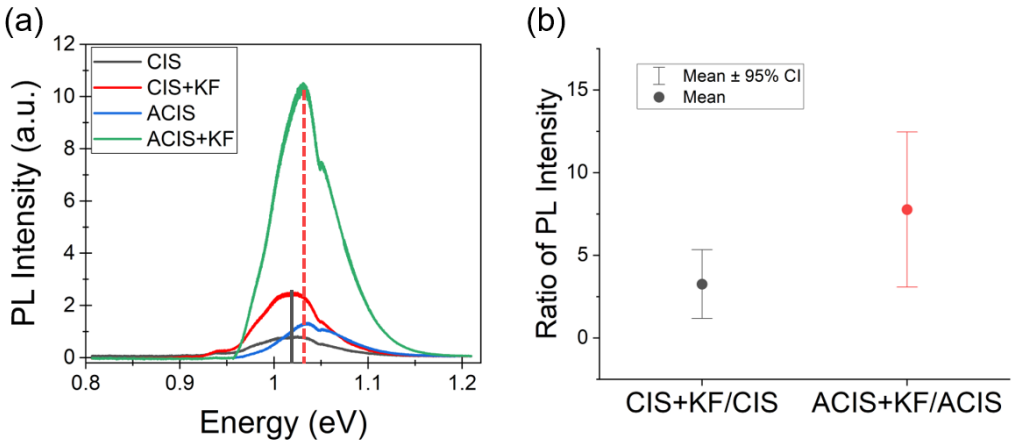

Figure 4.5: (a) Average photoluminescence spectra for all four samples, measured with a 532 nm laser. The peak maximum represents the band-to-band transition occurring at the bandgap energy. A slight increase is seen in the peak maximum for the Ag-samples due to their slightly wider bandgap as a direct result of Ag-incorporation (shift from solid black line to dashed red line). The edge around 1.055 eV is hypothesized to be a measurement artifact. (b) Ratio of the mean increase in PL signal with the use of KF-PDT for CIS (black) and ACIS (red). Bars represent the 95% confidence interval (CI) of estimating the mean PL ratio, suggesting the mean can lie anywhere within that range to a high degree of reliability.

mation on the degree of passivation by KF. It is important to note that due to the absorption of CIS of the 532 nm laser used, only approximately the top 80 nms of the absorber is studied. The average PL spectra for each of the samples is shown in Figure 4.5(a). The first observation is that the ACIS+KF sample has the highest overall PL intensity at the band-to-band transition that occurs around the bandgap of approximately 1.05 eV. Both the samples treated with KF-PDT show an increase in the PL intensity when compared to the non-KF treated samples (CIS and ACIS). The spectra for the four samples demonstrate similar features, indicating that a room temperature, there are no observable defects in any one of the samples, which would appear as an extra peak at sub-bandgap (less than 1.05 eV) energy. The edge to the right of the main peak occurring around 1.055 eV is attributed to the stitching of the spectra that is done due to the physical movement of the diffraction grating in the PL tool.

The individual spectra per-pixel of the PL maps were fit to a signal Gaussian to extract the peak amplitude. Figure 4.5(b) shows the ratio of average KF-treated PL intensity over the average non-treated PL intensity for the CIS series (black) and the ACIS series (red). Being that the mean values are greater than 1, it can be concluded that KF-PDT results in increased photoluminescence yield. Secondly, the relative improvement from the KF-PDT is higher for the ACIS case. The confidence intervals (bars) indicate however that the value for the mean can be reliably within 95% confidence within the boundaries, suggesting a much greater variation in the average benefit of the KF-PDT for the ACIS than is the case for the CIS.

The spatial distribution of the peak amplitude for one of each of the five maps of each sample is shown in Figure 4.6. The size and intensity difference of features is increased with the application of KF-PDT. In the CIS+KF sample, there are some features that are significantly more intense, such as the feature centered around (5,3) of Figure 4.6(b). The existence of these bright features then washes away those of lesser intensity, such as the

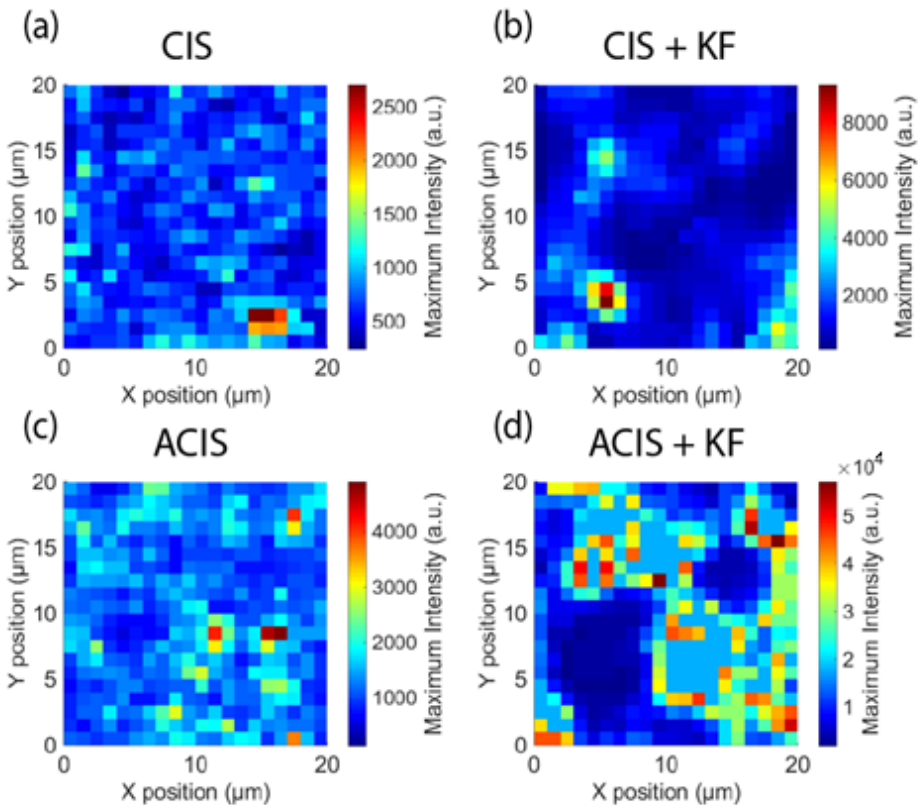

Figure 4.6: 20μm x 20 μm maps of maximum PL intensity, measured using a 532 nm laser, for the (a) CIS, (b)CIS+KF, (c) ACIS, and (d) ACIS+KF samples. The PL amplitude was obtained by fitting a single Gaussian to the spectrum of each pixel. Measurements courtesy of Michelle Chiu.

topology that is observed in the upper right corner of the same map. By the map's appearance, it suggests that the data may be bi-modally distributed. A similar observation is seen for the ACIS+KF in Figure 4.6(d), however the feature size of high intensity and low intensity particles is larger than the CIS+KF. The features here are on the order of multiple grains (average grain size is approximately 1 μm), whereas in the CIS+KF, the high PL features are smaller and closer to 1-2 grains in diameter. The appearances of the maps would suggest that, while the PL intensity is consistently improved with KF-PDT, it is not homogeneously distributed.

The KF-PDT seems to increase the inhomogeneity of the film, providing certain areas

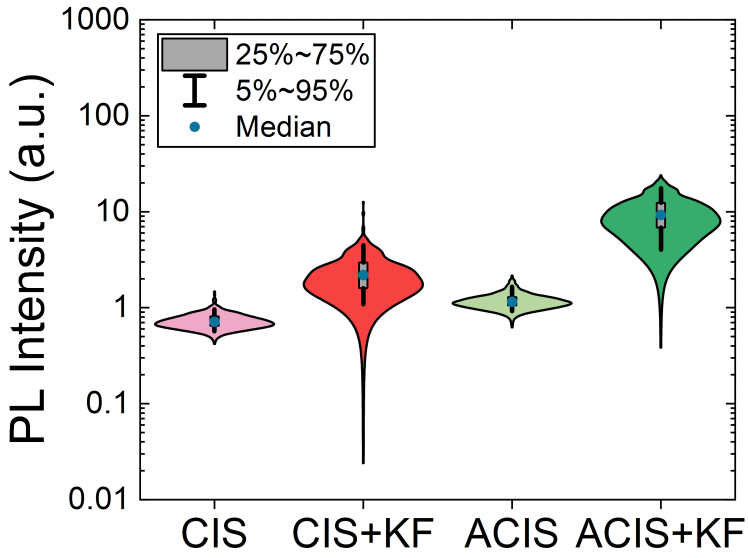

Figure 4.7: Violin plots on a y-log scale showing the distribution of the maximum PL intensity per-pixel of the CIS samples (red) and the ACIS samples (green). Darker shading indicates samples treated with KF-PDT. Blue dots are used to mark the median values and the grey boxes indicate the data in the inner-quartile region. The black whiskers indicate the data that lies within the 5^{th} and 95^{th} percentiles. Measurements courtesy of Michelle Chiu.

better passivation than others. Evaluating the data of the maximum PL intensity for multiple maps of each sample, the finding of increased inhomogeieinty is validated by increasing the sample size of the data. The total number of spectra evaluated across the 5 maps per sample represent over 20,000 data points. The data are represented as violin plots on y-log scale in Figure 4.7. The improvement in PL signal with the addition of KF-PDT is again clear looking at the median PL intensity values, as is the fact that the ACIS+KF sample improved by a larger factor than the CIS+KF did.

The shape of the violins also indicate the observation from the spatial maps that the samples treated with KF-PDT demonstrate increased inhomogeneity in PL intensity. The violins for the CIS+KF and the ACIS+KF are broader, pointing to the increased inhomogeneity observed in the multiple map areas. And lastly, we can see the observation of a slight bi-modal distribution, with a small shoulder toward higher PL signal for both KF-PDT samples, in agreement with the observations from the PL maps.

Through photoluminescence, reduced recombination through defects with KF-PDT has been validated. This suggests that the drop in V_{oc} and *FF* occurring for the ACIS+KF sample is not mediated by recombination at mid-gap states and/or the CIS/CdS interface. The results showed that the passivation is inconsistent across the sample, but the process by which this occurs is not determinable by PL alone. Being that KF-PDT has been cited for increasing V_{oc} by creating a $KInSe_2$ (KIS) surface layer that has a lower valence band maximum and can serve as a hole-repellent layer, synchrotron X-ray diffraction was used to search for the existence of KIS [156, 157].

4.3.1 No Indication of KF Passivation Through $KInSe_2$ Surface Layer

Thermodynamics supports the hypothesis that KIS can form in CIS and is in fact more likely to form as a secondary phase than in a mixed phase with CIS [83, 158]. Work by Donzel-Gargand *et al.* showed that excess KF concentration in ACIGS resulted in the formation of the KIS phase and also served to reduce the median V_{oc} values of the devices [99]. The results suggested that an optimal amount of KF needs to be used in order to benefit performance and therefore, excess KF in the form of a KIS surface layer can be responsible for the reduced V_{oc} found for the ACIS+KF device.

Figure 4.8 shows the synchrotron-based XRD pattern of the four samples under study, which make evident the absence of KIS or any Ag-related phases. From the data, the incorporation of Ag is evident, seen as a shift to lower scattering vector values and seen in the change of peak doublets to single peaks, such as those around Q=4.4 A^{-1} [147, 149, 159, 160]. These observations indicate that the higher V_{oc} in the CIS+KF does not originate from the existence of a KIS surface layer that acts as a hole barrier. It also suggests that excess KF was not incorporated in the Ag-alloyed sample and did not serve as the main mechanism for reducing the V_{oc} in the ACIS+KF device. Note that the measurement sensitivity limits us to crystalline materials larger than a few nanometer; amorphous or

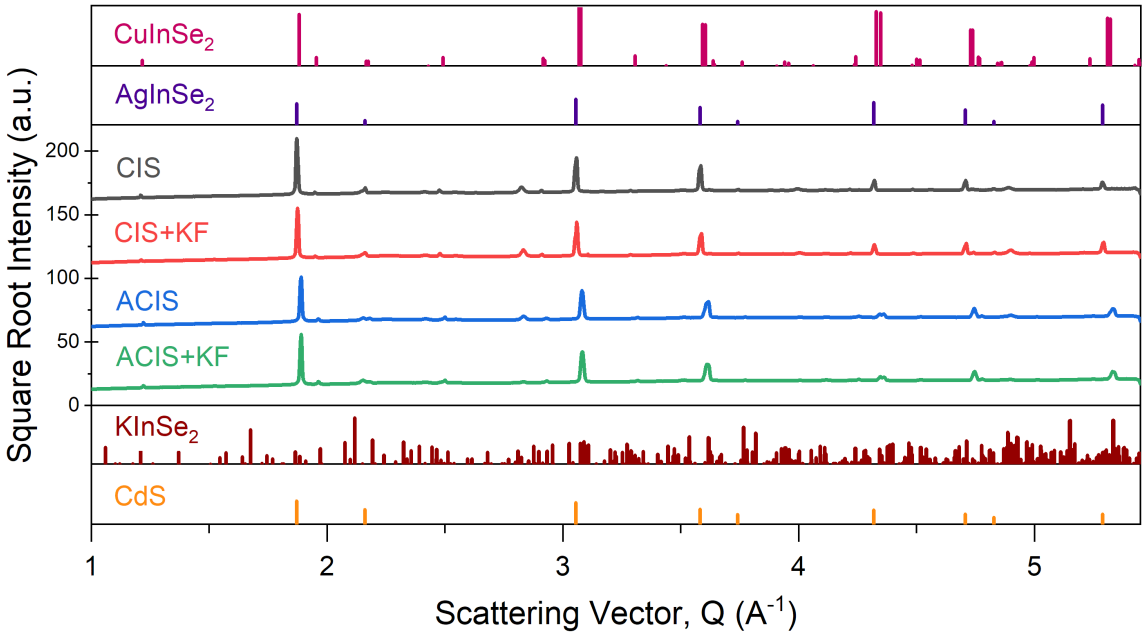

Figure 4.8: Square root intensity synchrotron X-ray diffraction patterns for CIS (black), CIS+KF (red), ACIS (blue) and ACIS+KF (green), measured using grazing incidence geometry. Each pattern is offset with a constant of 50. Reference spectra are shown for $CuInSe_2$ and $AgInSe_2$ (top) and $KInSe_2$ and CdS (bottom). Samples were full devices with the incident beam on the TCO side. The patterns shown are the average of six measurements taken per sample. Measurements courtesy of Dr. Archana Sinha.

small clusters would not appear.

Beyond secondary phases such as KIS or others as In_2Se_3 that are structurally distinct from CIS and should appear in XRD when in great enough concentrations, CI(G)S materials often contain ordered defect compounds (ODCs). Some of the most common secondary phases that result from ODCs are $CuIn_3Se_5$ and $CuIn_5Se_8$ [137]. Being that the compounds are long-range clusters of defect pairs, the structure of ODCs is the same as CIS and therefore their existence is indeterminable from XRD. Raman spectroscopy is one of the most accessible tools for identifying secondary phases formed from ordered defect compounds in CIS and their concentrations as it looks at the interactions of the atomic bonds to incident light.

4.4 Raman Spectroscopy of Ordered Defect Compounds and Cation Ordered CIS

2D Raman spectroscopy measurements were completed on the devices to investigate the existence of variations in defect concentrations that may be responsible for reduced performance in the ACIS+KF. A total of 5 maps across the samples were analyzed to increase the sample size probed. The map areas were the same as those studied by PL in section 4.3. This allows for pixel-by-pixel correlation of the observation of any phase formation to recombination.

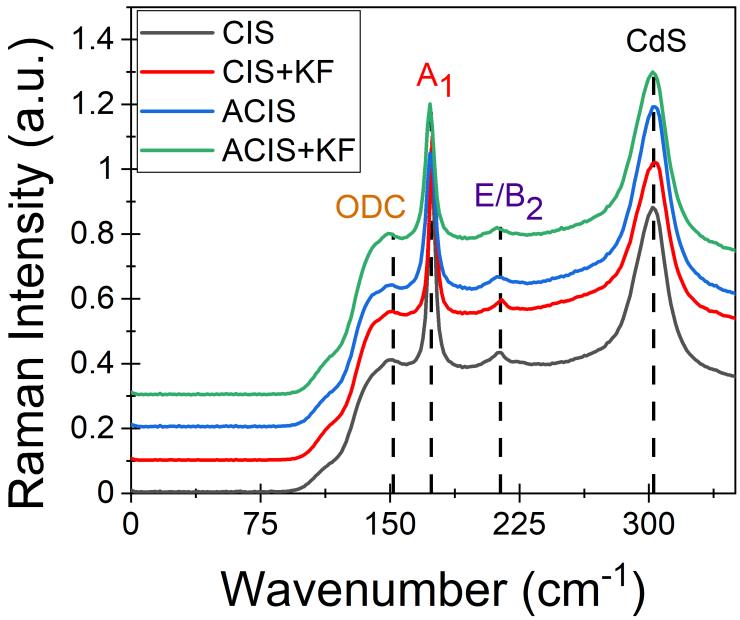

Figure 4.9: Average Raman spectra (taken from 5 sets of maps) for all four samples

The Raman spectra indicate the nature of the atomic bonds in the material by the peak position and the fitting of the peak amplitude indicates the concentration of the specific interactions observed. The average Raman spectra calculated from all of the pixels of all five maps for each sample are shown in Figure 4.9. In the four spectra, the same peaks appear, suggesting no significant concentrations of additional phases or compounds are found as a result of KF and/or Ag. In the spectra, we observe the A_1 mode for CIS around 174 cm^{-1} [135] and the peak associated with CdS at 304 cm^{-1} [139, 161, 162]. The peak

position of the A_1 mode is downshifted slightly to lower wavenumber for the Ag-alloyed samples as a result of the larger Ag atoms sitting in the Cu sites and causing compressive stress in the lattice along the c-axis [163]. This can be seen in Figure 4.10(a), which shows a zoom of the A_1 peak.

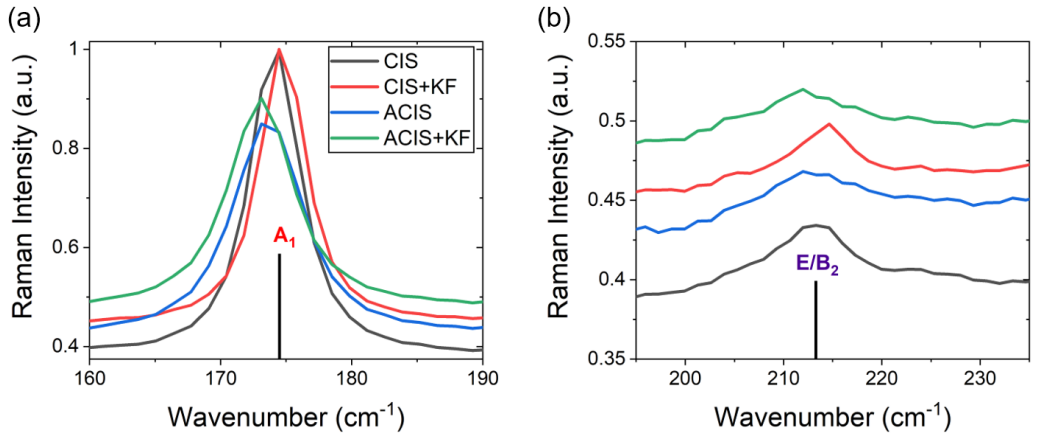

Figure 4.10: Zoom of the A_1 (a) mode and the E/B_2 (b) mode of the average Raman spectra (taken from 5 sets of maps) for all four samples.

Also clearly visible in the spectra of Figure 4.9 is the ODC peak at 152 cm^{-1} [79, 136, 137] that is down-shifted from the A_1 mode due to the change in the concentration of Cu and In around Se [138] and the E/B_2 mode centered around 216 cm^{-1} [79, 137, 164] that represents the asymmetrical stretching around Se [137]. The E/B_2 mode is attributed to cation ordering in CIS, which is the situation in which the cation atoms Cu and In alternate along the (100) plane, rather than along the (201) plane of chalcopyrite CIS, as hypothesized by Shirakata *et al.* [165] and demonstrated through high resolution TEM by Su *et al.* in the sulfide-based system $CuInS_2$ [166]. An example of the difference in appearance of the two structures (standard chalcopyrite CIS vs. cation ordered CIS) is observable in the inset of Figure 4.12. A zoom of this peak is shown in Figure 4.10(b) for comparison between the four samples.

The shift to lower wavenumber with the incorporation of Ag is seen for both the A_1

mode and the E/B_2 mode due to the size of the Ag atom sitting in the Cu site. The fact that this is seen also in the E/B_2 mode suggests that the incorporation of Ag is still observable in the cation ordered CIS structure and supports the idea that the observation of increased E/B_2 intensity is a factor of a structural change rather than the formation of a secondary phase, particularly one excluding Ag.

To understand any variation in the concentrations of Cu-poor ODCs or cation ordered CIS, the peaks for each are fit using individual Lorentzian functions to calculate the peak intensity. The amplitudes calculated from the fit per-pixel are represented as boxplots in Figure 4.11. The whisker lines represent the data within 5^{th}-95^{th} percentiles. Outliers falling outside of three standard deviations have been masked for visualization purposes. The fit results for the ODC peak at 152 cm^{-1} (filled boxes) show similar distributions and average values of peak intensity across the samples with and without Ag. Therefore, the addition of Ag is related to an increase in ODC concentration, regardless of KF-PDT. If this peak represents the phases $CuIn_3Se_5$ or $CuIn_5Se_8$ [167, 168], we could conclude that the incorporation of Ag further drives the formation of this Cu-poor ODC at least near the CdS interface. X-ray photoelectron spectroscopy (XPS) results of sister samples have shown an increased Cu-poor surface with the addition of Ag-alloying to support this observation [151].

The increase in ODC concentration corresponds most with the slight improvements seen in J_{sc} on the macro-scale and does not trend with the changes in device V_{oc} that are under question. This observation is supported by results from Sharan *et al.*[57], which showed $CuIn_3Se_5$ has a lower valence band maximum (VBM) and wider bandgap compared to $CuInSe_2$. The increased concentration of the ODC at the CdS interface lowers the VBM at the junction and acts as a hole barrier, increasing carrier collection through reduced recombination.

The results for the intensity of the E/B_2 mode (hashed boxes) instead show a different

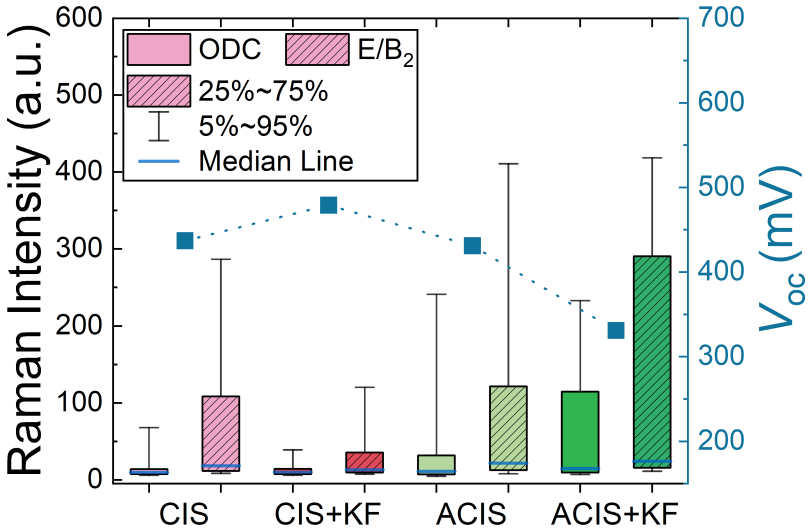

Figure 4.11: Boxplot data for the Lorentzian peak fitting results of two Raman modes, ODC at 152 cm^{-1} (solid boxes) and E/B at 212-218 cm^{-1} (hashed boxes) and V_{oc} values shown in blue squares (right y-axis).

behavior from that of the ODC mode, not appearing to be directly related to the addition of Ag. Overall, the intensity of the E/B$_2$ mode trends very closely, but inversely, with the change in V_{oc} in the devices (shown as blue square markers in Figure 4.11). The direct relationship between the E/B$_2$ intensity and the V_{oc} is demonstrated in Figure 4.12. The linear fit of the data shows clearly the existing inverse trend between the two variables.

The boxplot for CIS+KF shows the lowest intensity values of the E/B$_2$ mode and the tightest distribution paired with the highest device V_{oc} while the opposite is true for the ACIS+KF case. Note that the median values for peak intensity, shown as teal lines within the boxplots, are all of similar values for all four samples. This indicates that the upper half of the data is becoming more widely distributed and having higher intensities that trend directly with the bulk V_{oc}. The broader distribution of the peak intensity for the E/B$_2$ mode indicates increased chemical inhomogeneity in the form of cation ordered CIS. The expectation of increased cation ordering is not unrealistic as the formation energy of cation ordered CIS is estimated to be only 8meV/4 atoms (∼0.2 kJ/mole) higher than that of chalcopyrite CIS [166], and therefore can easily form during or after growth [164].

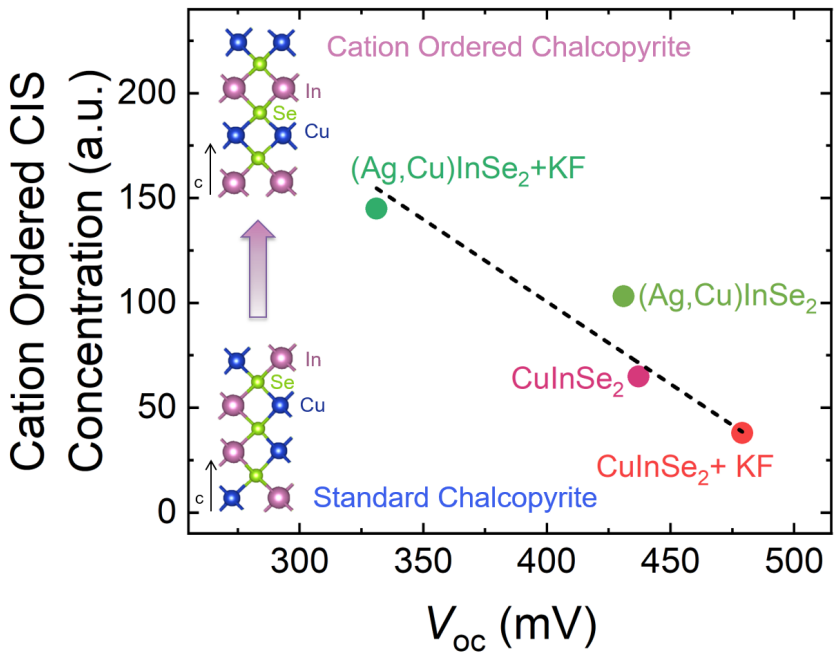

Figure 4.12: Correlation of the average E/B_2 mode intensity that is indicative of cation ordered chalcopyrite (structure shown top) to the device V_{oc}. Dashed line represents linear fit results. The structure on the bottom left is an example of the expected order of cations in chalcopyrite CIS.

4.4.1 Connection of Cation Ordering to Electrostatic Potential Fluctuations

The observation that cation ordering is inversely correlated to the V_{oc} suggests there is a meaningful relationship between the two that may be capable of describing the low open-circuit voltage in the ACIS+KF sample. From the results of PL mapping, recombination active defects were not found to be related to the reduced V_{oc} found for the sample alloyed with Ag and treated with KF-PDT (ACIS+KF). This indicates that the impact of cation ordering must not come directly through defect recombination.

Instead, cation ordering is a result of a different arrangement of the Cu and In atoms about the Se atoms. Cation ordered structures near surfaces and interfaces usually originate from the surface reconstruction needed to relieve the electrostatic dipole characteristics of CIS surfaces, which contrary to other semiconductors have a polar nature [169]. This reconstruction involves creating rows of defects, like V_{Cu}^{-} and In_{Cu}^{2+}. These charges com-

pensate each other as well as the surface dipole, and the overall inhomogeneity of the charge distribution causes potential fluctuations as described by Shklovskii and Efros' theory for semiconductors with high levels of defects and compensation [41, 42].

Being that XPS results did show an increasingly Cu- and Ag-poor surface for the ACIS+KF sample, relative to the ACIS and CIS+KF cases, the surface of the ACIS+KF is reasonably more populated by charged defects that require compensation by impurities. Dirnstorfer *et al.* described that defects are compensated by the formation of charged impurities, which creates a Coulomb potential with a depth that is dependent on the ratio of the concentration of charged impurities to free carriers (holes in the case of CIS) [42]. As the ratio of compensation by charged impurities increases, likely due to greater deviation from stoichiometric CIS, the depth of the fluctuations increases and can exceed the activation energy for recombination of donors or acceptors, in turn causing it to become the dominating mechanism [42].

Valdes *et al.* observed the ACIS+KF has the lowest activation energy of recombination, which they attributed to potentially increased interface recombination [147]. From the PL results, increased interface recombination was not found to occur in the ACIS+KF, helping to support the conclusion that instead the lowest activation energy of recombination affects the V_{oc} by making the device which the most easily affected by the existence of electrostatic potential fluctuations. This conclusion is also in agreement with the suggestion by Siebentritt, which stated that electrostatic potential variations are generally the most responsible for V_{oc} losses in CI(G)S solar cells and can amount to differences in voltages of up to 100 mV [18]. This discrepancy in open-circuit voltages is on the order of what was observed between the CIS+KF and the ACIS+KF.

Furthermore, Mainz *et al.* completed a comprehensive study on the growth of CIGS by the selenization process where Cu,In, and Ga are co-sputtered and then annealed in a Se atmosphere to complete the growth [170]. Their work found that the process time for

growing high-quality CIGS absorbers is limited rather by the formation and then evolution of cation ordered CIGS, rather than being limited by the time it takes for complete Se incorporation. Similarly, Sopiha *et al.* found recently by calculation that Ag-alloying can make the CIGS alloy unstable, which can result in film decomposition during the additional temperature step of PDT [152]. This highlights the impact of process time on reducing cation ordering and recommends that, in the case of samples grown with Ag, additional annealing time may be required to minimize cation ordering after applying KF-PDT.

4.5 Influence of Cation Ordering on Contact Selectivity

The previous sections demonstrated that the existence of cation ordered CIS at the CdS/CIS interface is directly related to the performance losses in the ACIS+KF sample. Measuring the external radiative efficiency (ERE) can further indicate whether the electrostatic potential fluctuations caused by compensating the cation ordered defects limit the device performance through recombination or an issue of the contacts/interfaces [171]. ERE works by first biasing the device to open-circuit voltage conditions where the carriers, electrons and holes, have distinct quasi-fermi levels. Then a calibrated excitation laser is incident to the sample and the emitted photons from the bias laser only are filtered and measured by a dual-phase lock-in amplifier [172]. The ERE signal measured by the lock-in amplifier is then the ratio of emitted photons to those incident, represented as a percentage. From this value, the implied voltage can be calculated as a function of the bandgap and temperature.

Figure 4.13 shows a graphic of the band diagram of a device measured with ERE, where the iV value represents the implied voltage from the quasi-fermi level splitting in the device. The emitted photons that are produced due to laser stimulation serve to describe the emission efficiency of the absorber, where the created voltage is independent of the specific contact resistances (denoted as *rho*/textsubscriptc,h). Instead, the voltage (V) measured

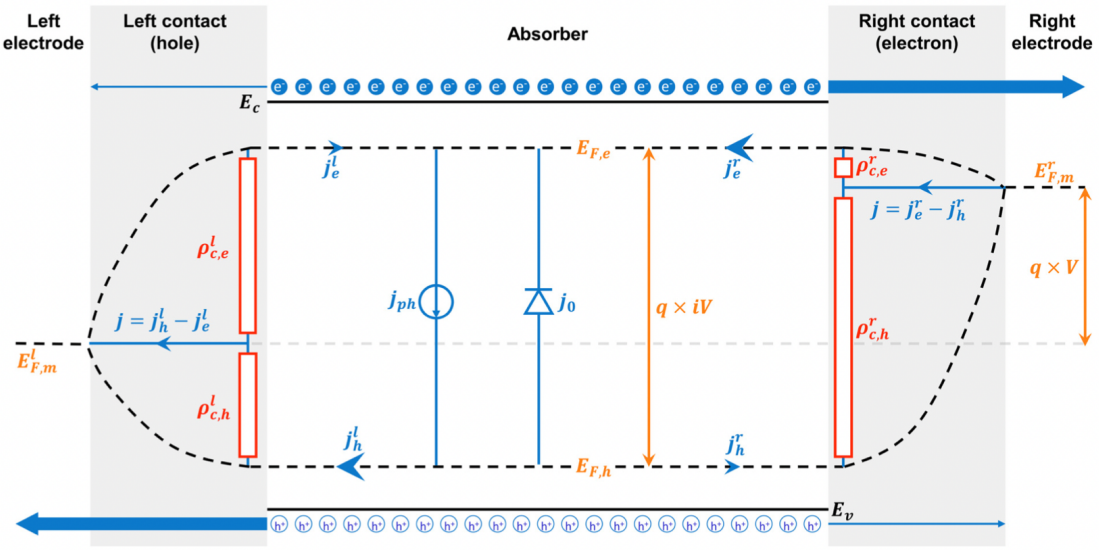

Figure 4.13: Band diagram graphic of external radiative efficiency measurements, which require a device under bias to produce fermi-level splitting. Taken from Onno *et al.* [170].

across the electrodes is reduced by the contact resistances of the left (hole) and right (electron) electrodes. The value differences between the measured V_{oc} across the electrodes, where the bands flatten, and the implied V_{oc} (iV_{oc}) calculated from the ERE measurement, are therefore a sign of the contact resistances in the device. The greater the reduction in V_{oc} relative to the iV_{oc}, the more the contact resistances are negatively affecting the output voltage of the device. In the inverse case, the closer the two values, the more "perfect" or carrier-selective the contacts can be considered.

Table 4.2 shows a direct comparison between the voltages for each of the four CIS samples. Studying strictly the iV_{oc} results, the trends follow closely to what was expected from the addition of KF-PDT for passivating defects. The implied voltage increases in both samples treated with a KF-PDT compared to their untreated counterparts, similarly to the results described by Elanzeery *et al.* [173]. This implies that the KF-PDT does have an impact on reducing recombination in the CIS absorbers. From the ERE results, it seems the addition of Ag alone does not have a significant impact on increasing the voltage, however this is reasonable due to the low overall concentration of Ag added.

Table 4.2: Comparison of Measured Open-Circuit Voltage to Calculated Implied Voltage from ERE

Sample	V_{oc} (mV)	iV_{oc} (mV)	ΔV_{oc} (mV)
CIS	437	460	23
CIS+KF	479	467	-12
ACIS	431	458	27
ACIS+KF	331	475	144

Despite the minimal observed impact of Ag-alloying on its own, the ACIS+KF demonstrates the highest implied V_{oc} as was originally expected. This observation becomes even more clear when studying the delta between the measured device V_{oc} and the iV_{oc}. The delta V_{oc} for the ACIS+KF sample is over 100 mV greater than any other sample. This again relates to the conclusion by Siebentritt *et al.* that suggested electrostatic potential fluctuations can result in over a 100 mV difference [18]. As a note, the ΔV_{oc} cannot physically be negative and so the observed discrepancy arises from an accuracy limitation of the current tool setup or the calculation of the iV_{oc} value from the ERE.

Therefore, the ERE results suggest that while the absorber quality was improved by the combination of Ag and KF, the low resulting device V_{oc} for the ACIS+KF is a factor of greater contact resistance rather than increased recombination within the absorber. This further supports why the ACIS+KF sample demonstrated increased PL yield (Section 4.3) despite the observation of an increased concentration of cation ordered CIS. Combining the findings from the PL, Raman spectroscopy, and ERE measurements, we can conclude that the formation of cation ordered structure at the CdS interface is detrimental to the contact quality of the device.

These findings are extremely important when beginning the consideration of industrial CIGS devices. Industry standards incorporate both Ag and KF-PDT to achieve record efficiencies [15]. This section has demonstrated that combining complimentary measurements can provide holistic view of the absorber, the contacts, and the device behavior. The development of contactless measurements such as ERE can serve as a highly effective first step

in device characterization. Results from ERE can point to where ensuing characterization should focus, either on the absorber quality or the contacts and interfaces. In the following section, a similar approach will be used to evaluate what limits device performance in devices that contain Ga, as well as optimized concentrations of both Ag and KF.

Chapter 5

METASTABLE DEFECTS IN INDUSTRIALLY-RELEVANT ACIGS SOLAR CELLS

In the previous chapter, the importance of optimized Ag and KF post-deposition concentration temperatures and process times was highlighted in the simpler materials system, $CuInSe_2$. It was found that Ag and K can drive increased formation of cation ordered CIS, a different atomic ordering than the standard chalcopyrite structure. Cation ordering was hypothesized to drive down the device V_{oc} due to increased electrostatic potential fluctuations that arise from the need of impurities to compensate the defects of the cation ordered structure.

Commercial CI(G)S solar cells also commonly incorporate Ag and K for increased J_{sc} and V_{oc}. These devices have been optimized for their concentrations such that they can demonstrate efficiencies over 18.5% on full sized modules. As a result, their performances are more limited by issues with long term reliability. In thin film solar cells, light soaking response has been frequently cited as a source of reduced current collection efficiency [73]. In particular, devices demonstrate a metastable response to light soaking, which makes reliable and predictable field performance more elusive.

The light soaking response in CIGS has been observed to occur on relatively short time frames, often within a few hours. It has been proposed that light soaking behavior arises from either the electromigration of elements within the absorber [78, 81, 174] and/or through changes in the configuration of the defect pair V_{Se}-V_{Cu} between an acceptor and a donor [64, 67]. XRF mapping can again be applied in this situation in order to evaluate metastable defects by combining it with electrical measurements to relate composition to its impact on the device. In this chapter, nano-scale X-ray absorption near-edge spectroscopy (XANES) measurements are described that look into the coordination environment around

Cu and Se and the potential evolution with light soaking.

5.1 Sample Preparation and Background

Fully encapsulated mini-modules were prepared by standard roll-to-roll processing by MiaSole Hi-Tech Corp [64, 76]. Samples were alloyed with Ag and treated with a KF post-deposition treatment. Different concentrations of Se were applied initially to the Mo back contact to drive the formation of $MoSe_2$. The samples studied here are denoted high PS (pre-selenization) as excess Se was deposited prior to the CIGS growth. After the mini-modules were prepared, half of the samples were placed in a dark heat (DH) tester at 85°C for 1000 hours, following the procedure described in [69]. This resulted in samples denoted as initial and DH, respectively. An example of the mini-modules studied is seen in Figure 5.1.

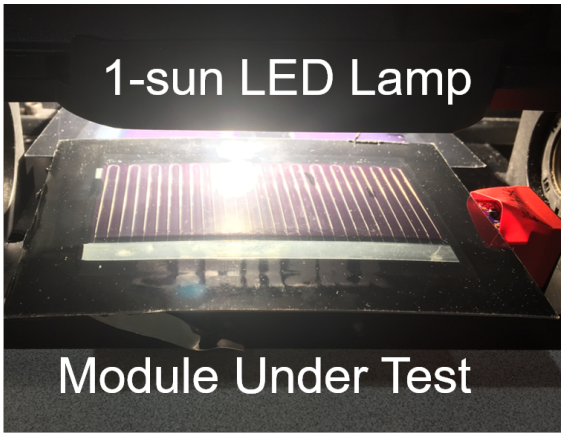

Figure 5.1: Image of the mini-modules studied. The sample is shown during the light soaking procedure used.

JV curves of multiple sister mini-modules (7 each) were measured under 1-sun illumination before and after 24 hours of light soaking (LS). Figure 5.2 shows the trend in J_{sc}, V_{oc}, fill factor (FF), and efficiency (η) after LS, DH, and DH+LS. The results show that efficiency values after DH and LS follow a different trend depending on the pre-selenization conditions. In particular, for the high PS sample, changes in the efficiency with dark heat and light soaking are driven by changes in V_{oc} and FF. Regardless of the PS concentration,

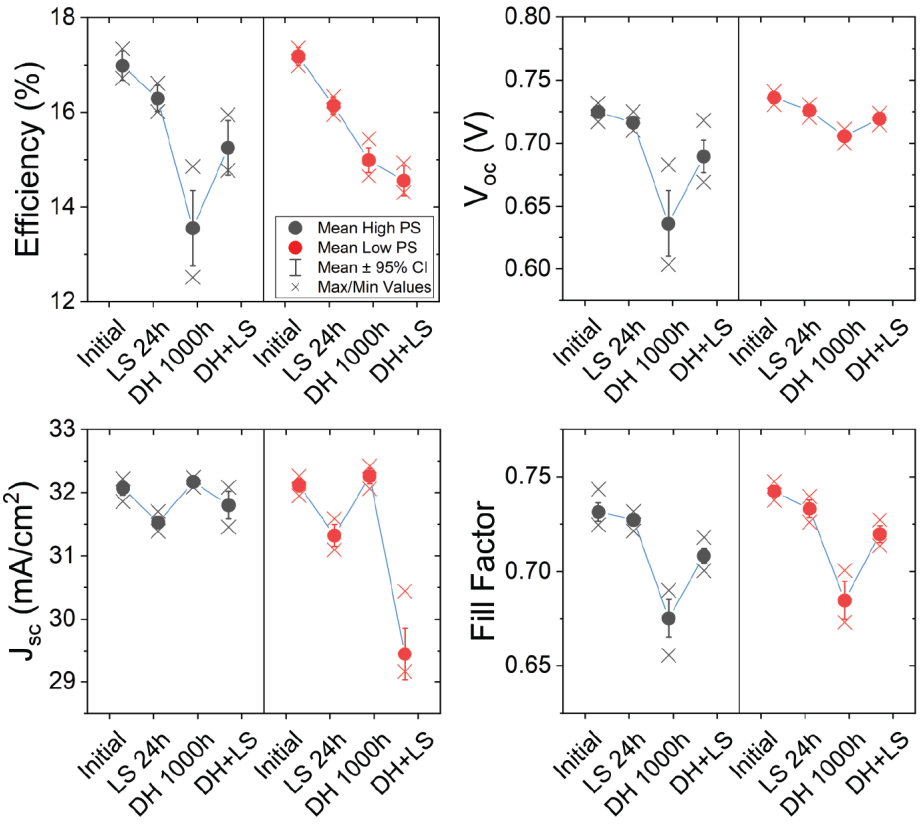

Figure 5.2: J-V characteristics of 7 sister samples to those studied with XRF, shown for the high PS (black, left) and low PS (red, right) samples for efficiency (η), V_{oc}, J_{sc}, and fill factor (FF). Data courtesy of MiaSolè.

J_{sc} values are reduced for both initial state and DH state upon light soaking, yet the drop in J_{sc} is more pronounced in the Low PS case. This is potentially related to the impact that Se concentration on the back contact has on the double-grading of Ga in the absorber depth, which has been shown to relate to V_{oc} and J_{sc} in devices [20]. Nikolaeva *et al.* even related Ga concentration in the depth to reduced electrostatic potential fluctuations after light soaking [25].

XRF/XBIC/XBIV measurements were performed at end station 2-ID-D of the Advanced Photon Source at Argonne National Laboratory. After mapping the samples at room temperature, they were light soaked (LS) ex-situ for 24 hours under 1-sun illumination using an LED lamp as was seen in Figure 5.1, and then remeasured. Sample temperature

was measured regularly during the light soaking process to ensure no sample heating took place. After light soaking, measurements were repeated on the same areas of those measured before LS. Data was fitted and quantified, then corrected for thickness variation by dividing by the total elemental concentrations [118, 154].

5.2 Behavior in High Pre-selenization ACIGS

5.2.1 Role of Compositional Variations

We first consider the mini-modules that have not been exposed to dark heat, denoted as the "initial" case. Figure 5.3 demonstrates the distribution of the Cu and Se areal density before light soaking (top row) and after light soaking (bottom row). The general features and contrast between the two elements do not seem to change significantly after light soaking. Only the Se channel appears to cluster more, seen by the increased range of the data. Calculating the change in the data range for both Cu and Se before and after light soaking,

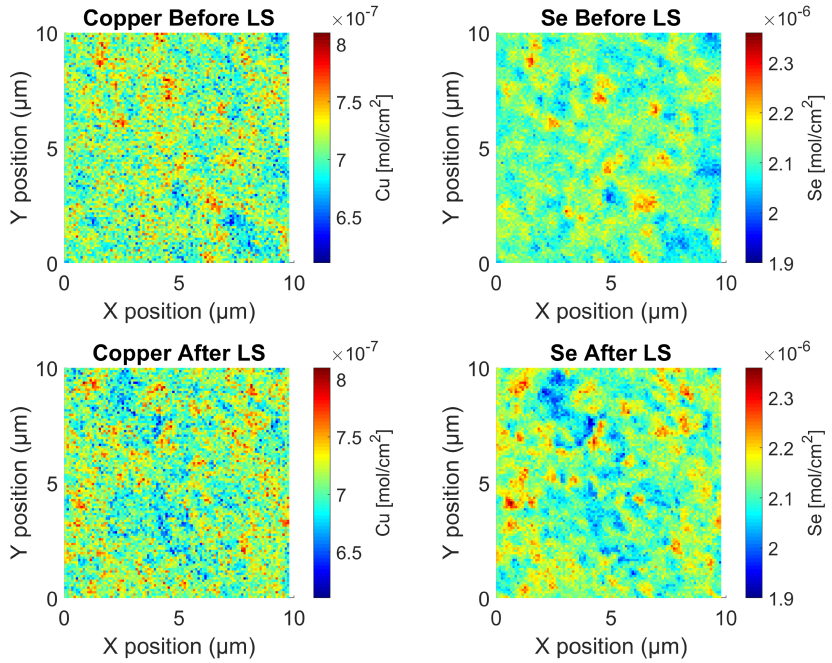

Figure 5.3: Example XRF maps of the distribution of Cu and Se in the high pre-selenization case of the initial samples before and after light soaking.

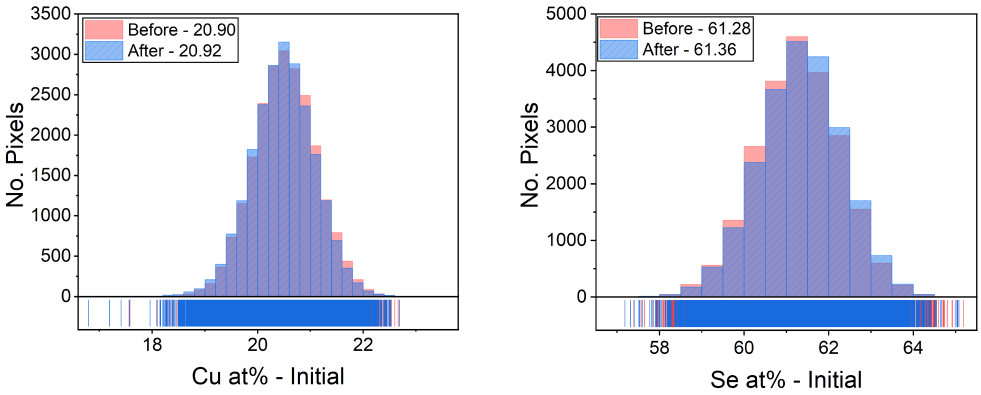

Figure 5.4: Histograms showing the change in the distribution of the Cu and Se atomic percentages (at%) for the high PS sample before (red) and after (blue) light soaking for the initial case. Median values are included in the legend.

it was found that while the distribution of the Cu concentration remains constant, the range of Se concentration increases by up to 40%. This quantifies the observation of increased clustering of Se and indicates that Se may be migrating due to exposure to light soaking. Note that the maps before and after were taken in the same general area, but not exactly the same regions due to limitations in sample registration. Therefore, while the features cannot be directly compared, their shape and distribution has been observed to be similar across different map areas.

Taking into consideration data from multiple maps, the distribution of the Cu and Se concentrations are shown in Figure 5.4. The distribution of the data after light soaking appears to shift slightly for both elements. From the previous calculations, we know that the overall width of the distribution is not changing for the Cu. This further indicates that Se may be moving within the absorber layer. In order to validate Se migration, cross section XRF measurements are planned for future work.

Figure 5.5 shows equivalent histograms for Cu and Se concentration before and after light soaking for the dark heat samples. In this situation, the change in the distribution of Cu and Se does not appear to be significantly changed, even when analyzing over multiple maps representing over 22.5k data points. This highlights the complexity of the metasta-

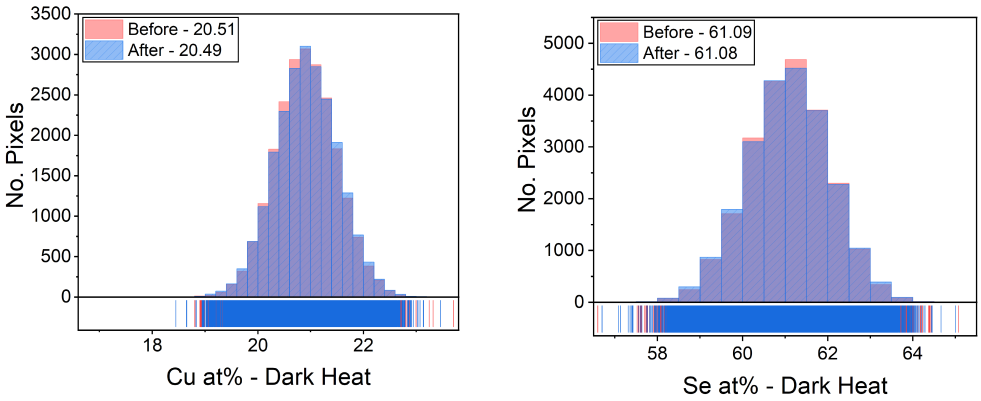

Figure 5.5: Histograms showing the change in the distribution of the Cu and Se atomic percentages (at%) for the high PS sample before (red) and after (blue) light soaking for the DH case. Median values are shown in the legend.

bility in CIGS solar cells.

5.2.2 Relationship of Composition to Performance

Both XBIC and XBIV maps were taken to describe variations in current and voltage. An example of two XBIV maps, before and after light soaking of the dark heat sample are shown in the bottom of Figure 5.6. The maps were measured of the same areas but were slightly shifted, which is exemplified by the white dashed boxes in the images that highlight a feature that is the same in both maps. The maps being of the same area allow us to clearly observe the change in the features upon light soaking. Overall, the XBIV map becomes more blurred with LS, but even the encircled blue feature changes in its overall appearance.

The top row of Figure 5.6 plots the average values for XBIC and XBIV, such that they may be directly related to the bulk JV measurements. Interestingly, the trends observed for J_{sc} and XBIC are very closely related, following the same overall trend. The XBIV signal, on the other hand, has a inverse trend with that observed for the device V_{oc}. Note that because all of the electrical maps were taken using a lock-in amplification setup, the values do not represent the absolute value of the parameter (I,V) at the nano-scale, but

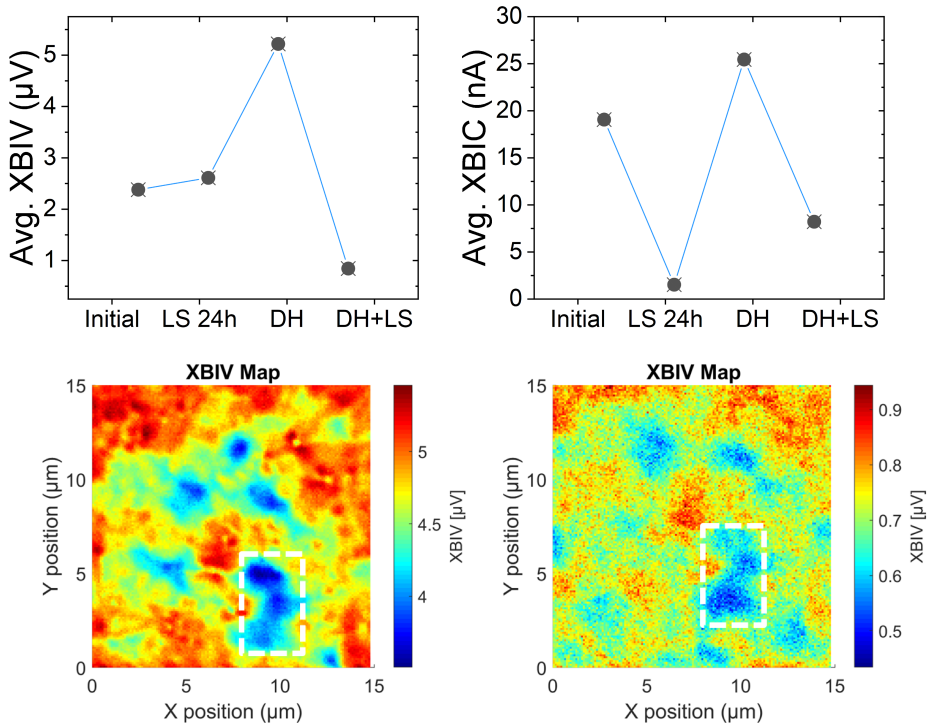

Figure 5.6: The average values (top) of XBIV (left) and XBIC (right) calculated from the nano-scale maps. Example maps for the spatial distribution of the XBIV signal are shown (bottom) for the dark heat high pre-selenization sample, before (left) and after (right) light soaking. The dashed white box marks a distinguishable feature seen in both maps to demonstrate that the data are from the same areas.

rather a signal in a defined frequency band around the reference frequency range. Because of this, and the particular dependence that J_{sc} and V_{oc} have with injection level (linear vs. logarithmic), the XBIC results follow the macro-scale J_{sc} trends, but the XBIV response is more difficult to correlate with V_{oc} as the samples undergo LS and DH. A closer look at the logarithmic dependence of V_{oc} with injection level shows that the rate at which V_{oc} changes with injection in the high injection regime is smaller for good performing cells than for poor performing ones. The importance of such considerations have also been discussed elsewhere with regards to surface photovoltage measurements [175].

The observation of changes in feature sharpness on the nano-scale was observed on CIGS before, however the changes were induced by increasing temperature [176]. In the work by Stuckelberger *et al.*, the XBIV data that became sharper with increasing temper-

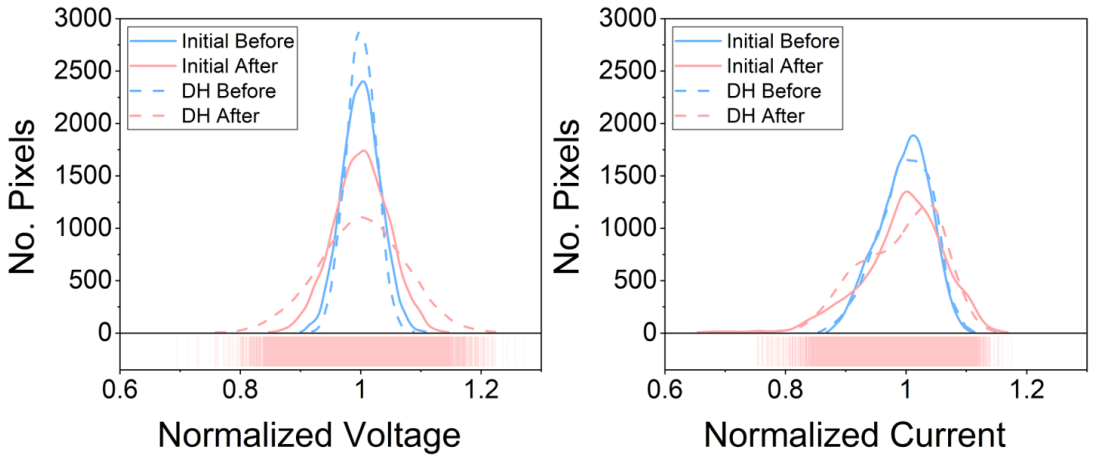

Figure 5.7: Histogram distributions of the median standardized voltage (left) and current (right) signal for the initial sample (solid line) and dark heat sample (dashed line) before (blue) and after (pink) light soaking.

ature was transformed from maps into histograms to visualize the decreasing width. In a similar fashion, the histograms of the XBIV signal are shown in Figure 5.7.

From the histograms, it is clear that with light soaking, the signal is broadened, as was suggested by the blurred appearance of the XBIV map. This broadening may be indicative of a change in the carrier diffusion length: as the diffusion length increases and carriers travel further before being collected, the XBIV measurement becomes less resolved from pixel-to-pixel. This is especially the case if the carrier lifetime begins to surpass the measurement rate in certain areas.

Looking similarly at the XBIC signal, we find that the signal is also broadened with light soaking. Both samples (initial and DH) show a change in the overall shape of the histograms after LS. Both develop a shoulder, however to opposite sides of the mean. The initial case after LS becomes skewed to the right, whereas the DH case after LS becomes skewed to the left, toward lower XBIV signal. The development of such shoulders toward the low XBIC signal was shown in Chapter 4 and was found to be related to compositional inhomogeneity. To isolate the shoulder data from the mean data, K-means clustering was

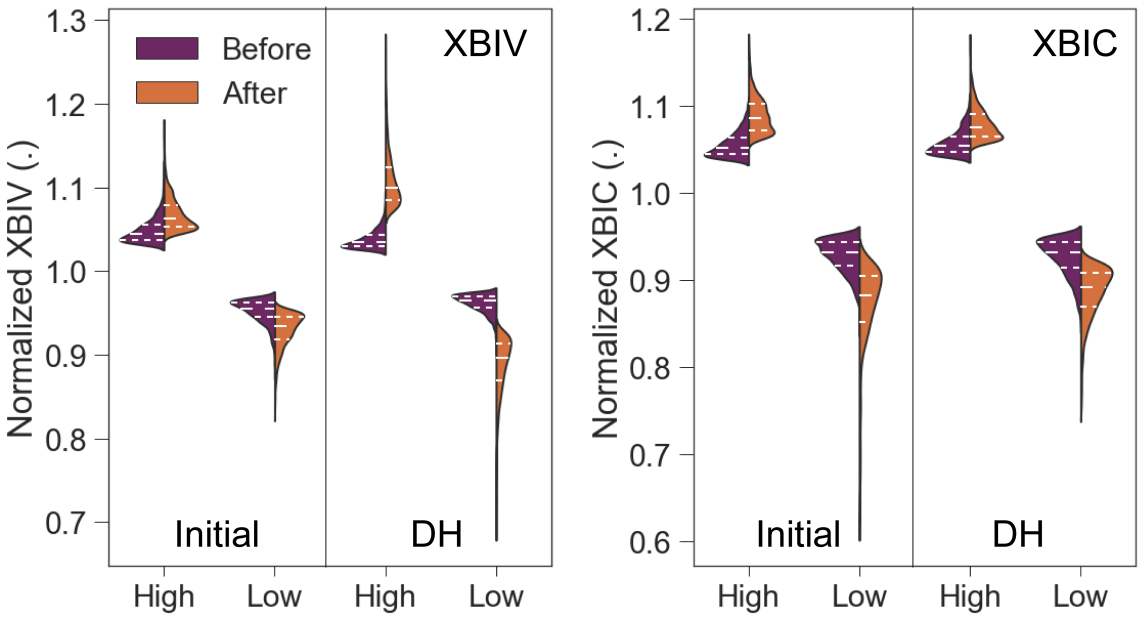

Figure 5.8: Split violin plots for the high and low XBIV (left) and XBIC (right) data, found by taking the data above and below one standard deviation of the normalized electrical signal. The thin dashed lines represent the upper and lower quartiles and the thick dashed line represents the median.

used to separate the electrical maps into two groups of high and low signal.

The electrical data for each group was analyzed and plotted in the form of split violin plots shown in Figure 5.8. Looking first at the XBIV data, there are two trends that stand out. Firstly, light soaking results in a broader distribution for both the high and low areas of both the initial and DH state, in agreement with the previous finding. This validates that the increased distribution in XBIV is occurring due to a greater intensity of pixels in both the high and low XBIV groups, such that the data is broadened symmetrically. Secondly, the impact of light soaking on the distribution of XBIV in the DH is significantly more extreme than in the initial case.

The data for XBIV then become broader symmetrically with light soaking, with the DH case more affected relative to the initial case. The results for XBIC show an opposite behavior. The data are asymmetrically skewed after light soaking, with the low XBIC areas becoming worse to a greater extent than the high XBIC areas become better. The increase

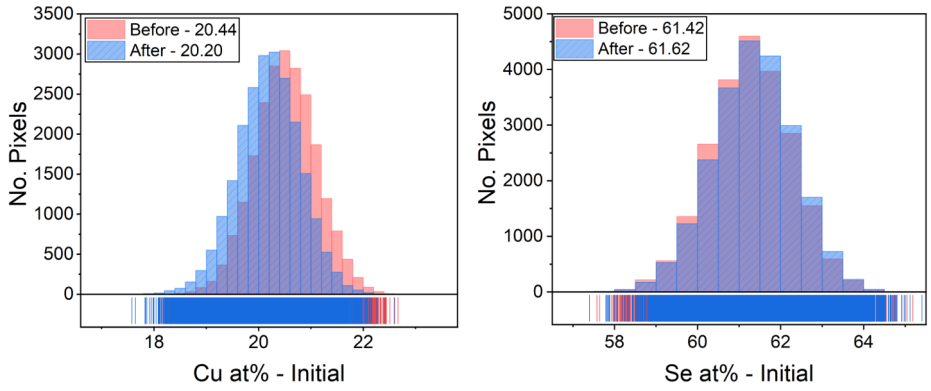

Figure 5.9: Histograms showing the change in the distribution of the Cu and Se atomic percentages (at%) for the low PS sample before (red) and after (blue) light soaking for the initial case.

in the low XBIC tail's distribution with light soaking may be related to what is responsible for the reduced J_{sc} with LS seen from the J-V measurements. Note that the violin plots display histograms fitted with a normal distribution in order to form the violin boundary, which is the reason why the violin plots on the sides that the data is cut off at the limits of one standard deviation is not a sharp line, but rather curved.

In the high pre-selenization sample, Se migration was observed and may be related to the changes in the device performance that occur with dark heat and light soaking. The change in performance was observed to occur through increased carrier diffusion length or lifetime. Increased diffusion length may very well be possible in the instance that certain trap defects are removed with light soaking. However, further analysis of the data is required to directly relate the two observations. Additionally, the importance of excess Se in the proposed process needs to be elucidated to determine if Se migration is limited only to the case of excess Se case (high PS).

5.3 Behavior in Low Pre-Selenization ACIGS

5.3.1 Role of Compositional Variations

The low pre-selenization case demonstrates a different behavior with regards to the chemical composition. Figure 5.9 shows the initial Cu and Se atomic percentages as they change with light soaking. In this sample, the median concentrations shift much more significantly, without a change in the overall distribution. Thus the XRF results would indicate that the sample becomes more Cu poor and Se rich, though this is not possible. Instead, due to the nature of secondary absorption in XRF measurements, a lower Cu signal suggests the movement of Cu toward the back of the cell, deeper into the absorber and thus having less likelihood of exiting the sample to be read by the fluorescence detector.

It is important to note that the concentrations may vary between before and after maps due as the map areas were not representative of the same locations. To validate that direct comparison is accurate, we have checked that the elemental concentrations in $\mu g/cm^2$ of the entire map areas are consistent before and after LS. The samples have also been normalized for thickness variations, through the procedure provided by West *et al.* [154], to prevent any measured change in composition arising due to increased material thickness.

The samples for the DH instead do not change significantly with LS (Figure 5.10) and the median concentrations remain constant. The histograms shown of data for after light soaking (blue) do seem to become broader, however, this is due to a decrease in the dwell time for these maps. The shortened dwell time causes overall reduced signal-to-noise and affects the distribution of the maps. Other map data also confirms that there is minimal change between the Cu and Se distribution before and after light soaking of the dark heat case. The mechanisms through which dark heat may minimize elemental re-distribution is not clear at this time.

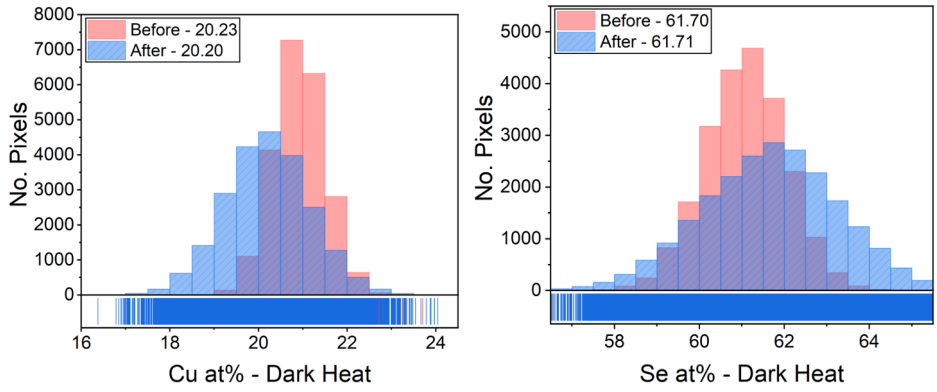

Figure 5.10: Histograms showing the change in the distribution of the Cu and Se atomic percentages (at%) for the low PS sample before (red) and after (blue) light soaking for the DH case.

5.3.2 Relationship of Composition to Performance

The overall trends for the average XBIV and XBIC signal are shown in Figure 5.11. Again, the average XBIC values relate closely to the behavior on the macro-scale, corresponding closely with the J_{sc} values. The V_{oc} again is not related to the XBIV signal, as can be expected. The map data in the bottom of Figure 5.11 also again show an reduced image contrast with light soaking (left).

Unlike in the high PS case, the average XBIC and XBIV signals for the low PS case trend almost perfectly with one another. This can indicate that the measurements are being dominated by the series resistance of the device, which affects both electrical measurements. A change in series resistance with light soaking or dark heat is not unexpected and has been observed in literature before [72, 177, 178]. Series resistance in fully encapsulated devices may be affected a change in the thickness of a MoO_x layer at the back contact [179]. X-ray diffraction measurements used to probe the formation of Mo- and Se-related layers are discussed in the following section.

The histograms of the XBIV signal in the low PS samples observe the same broadening as in the high PS samples. However, the initial and dark heat samples show the same

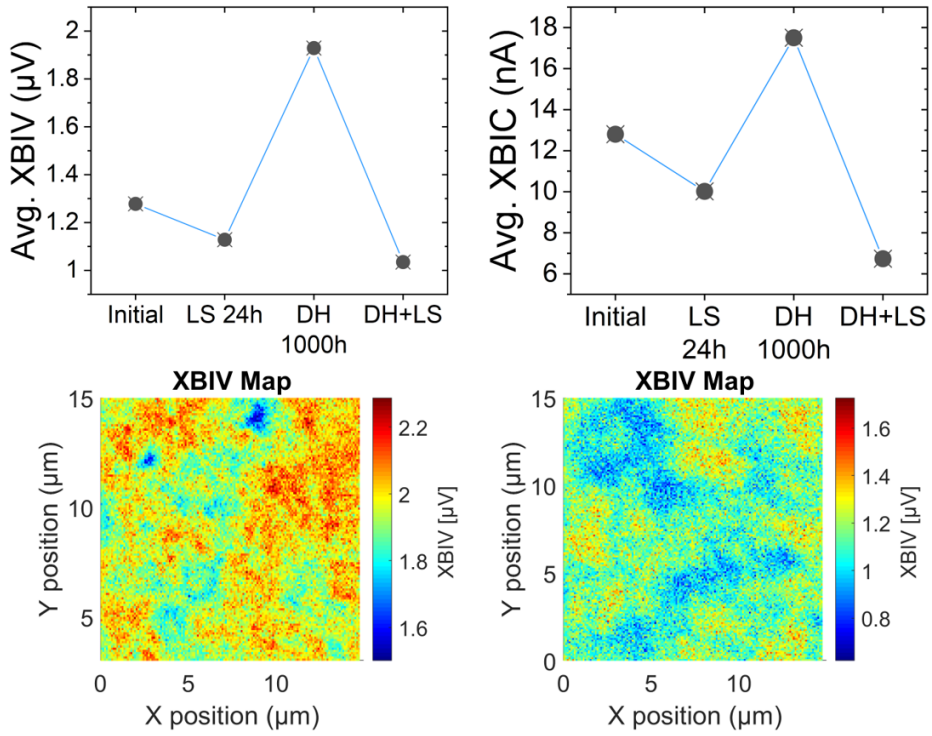

Figure 5.11: The average values (top) of XBIV (left) and XBIC (right) calculated from the nano-scale maps. Example maps for the spatial distribution of the XBIV signal are shown (bottom) for the dark heat low pre-selenization sample, before (left) and after (right) light soaking. The dashed white box marks a distinguishable feature seen in both maps to demonstrate that the data are from the same areas.

behavior in this case, demonstrating almost identical distributions within the before and after light soaking categories. This similarity between the performances of the initial and DH samples would suggest that there is no significant difference in the diffusion length, and in turn the defect chemistry, with dark heat. This could further support the hypothesis that the low PS samples are most greatly affected by increases in series resistance, particularly with DH. It shows that performance variations between initial and DH most likely are not coming from a change in the defect chemistry. Again, greater analysis of XANES measurements will also allow us to validate the absence of significant changes in defects with dark heat, especially.

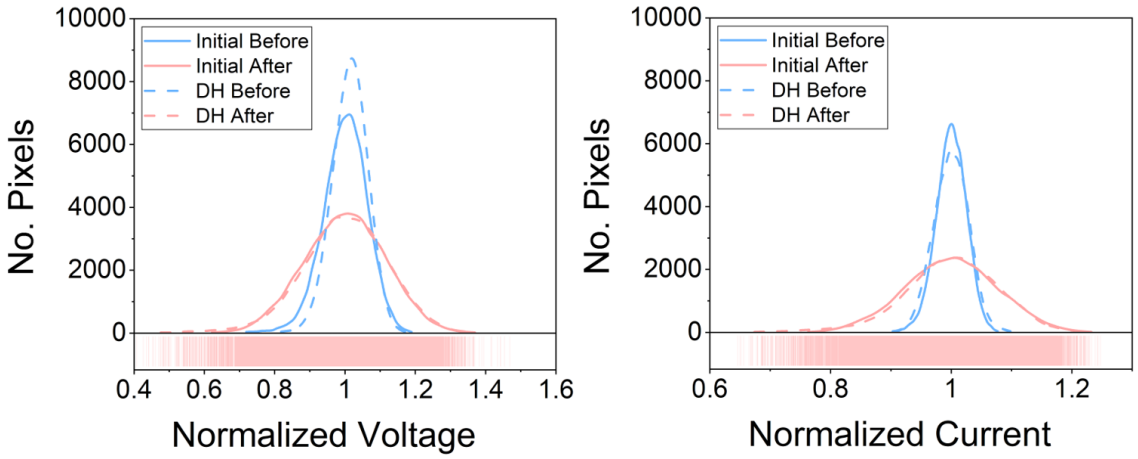

Figure 5.12: Histogram distributions of the median standardized voltage (left) and current (right) signal for the initial sample (solid line) and dark heat sample (dashed line) before (blue) and after (pink) light soaking.

5.4 Contact Quality, Selectivity and Mo-Related Secondary Phases

As evidenced in the previous Chapter in Section 4.5, external radiative efficiency measurements can be useful for narrowing down the culprits of or behind efficiency losses in completed devices. Here, X-ray diffraction was completed to investigate the formation of secondary phases that may influence the contact quality for the high or low pre-selenization samples. A positive relationship between the selenization concentration and secondary phase concentration is expected because as Se is applied to the Mo prior to growth, a thin layer of $MoSe_2$ has been shown to form. that may help to reduce recombination by discouraging the growth of MoO_x [180]. The XRD patterns are shown in Figure 5.13 for the low PS case. Beneath the patterns are simulated patterns of certain commonly observed secondary phases including $KInSe_2$ and In_2Se_3 [103, 158, 181].

The most dominant peak is assigned to the polymer, ethylene-tetrafluoroethylene (ETFE) [182]. The samples studied were fully encapsulated module pieces to retain the direct comparison to industry standards. However, this does limit the interpretation of the XRD data as a portion of the XRD patterns for the CIGS layers are buried beneath the signal from the

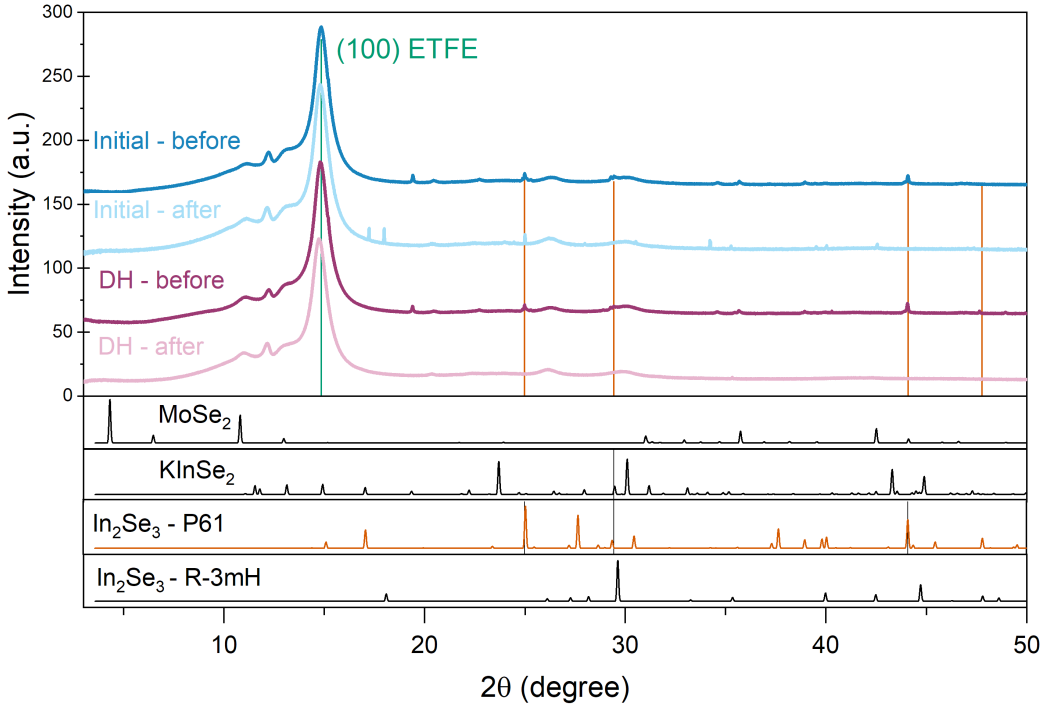

Figure 5.13: X-ray diffraction patterns for the low pre-selenization sample with and without dark heat exposure, and before and after light soaking. Simulated patterns of some expected secondary phases are shown below the figure. The pattern for ACIGS is not observable due to the strong signal coming from the polymer encapsulants, primarily the ETFE. Results courtesy of Dr. Leah Kelly.

encapsulants.

Of the patterns easily distinguished, there are a few things that can be said about the existence and evolution of secondary phases in the devices. In Figure 5.13, some of the peaks corresponding to the secondary phase In_2Se_3 were identified. Alternatively, no peaks were identified for $MoSe_2$. This may be due to the fact that In_2Se_3 is more expected to form at the CIGS surface due to the Cu-poor environment, whereas $MoSe_2$ is expected to be at the back of the CIGS absorber where signal attenuation by the encapsulants makes the signal weaker.

The existence of In_2Se_3 furthermore seems to be more clearly observed prior to light soaking; particularly note the peaks at 30 degrees and 44 degrees fade away after light

soaking. Additionally with light soaking, the ETFE peak shifts slightly to lower 2θ, which would indicate an increase in the interatomic spacing. The shift is more pronounced in the sample that has been previously dark heated. The changes to the polymer can therefore be a symptom of heating [182] or even a change to the structure of the polymer due to light exposure, such as yellowing that has been evidenced to occur in other commonly used solar cell encapsulants [183, 184].

Similar results on In_2Se_3 dissolution with light soaking were observed for the high PS case. This is expected because despite the pre-selenization concentration, the samples were anticipated to be similarly copper poor at the surface. The preliminary indications of a change in secondary phases at the surface suggest that there is a change in the defect environment in the devices as a function of light soaking, as was previously hypothesized.

As was demonstrated in the case of the CIS, Raman spectroscopy can be a useful tool in evaluating secondary phases at the surface of the ACIGS absorber. Figure 5.14 shows the average Raman spectra taken from 2D Raman maps for each of the samples, high and low PS, before light soaking. The spectra show similar peaks for all four samples, suggesting there is no significant contribution from any additional phases. It is important to note again as a reminder that due to the laser wavelength, the Raman measurements are only sensitive within the first 80-100 nm of the ACIGS absorber.

Similar peaks are found for the ACIGS samples as were observed previously in Chapter 4. The A_1 vibration for the CIGS is visible at 174 cm^{-1}, as is the CdS mode at 304 cm^{-1}. The spectra on the right of Figure 5.14 are the acquired Raman results for the various module encapsulants used in the mini-modules. Comparing the left and the right, it is clear that a number of vibrational modes in the polymers interfere with peaks of interest for the CIGS. In particular, the ETFE is again a major limitation to the analysis of the Raman results. The majority of the Raman signal appears to arise from the polymer materials, and due to the peak overlaps, it is a challenge to remove the background signals from the CIGS.

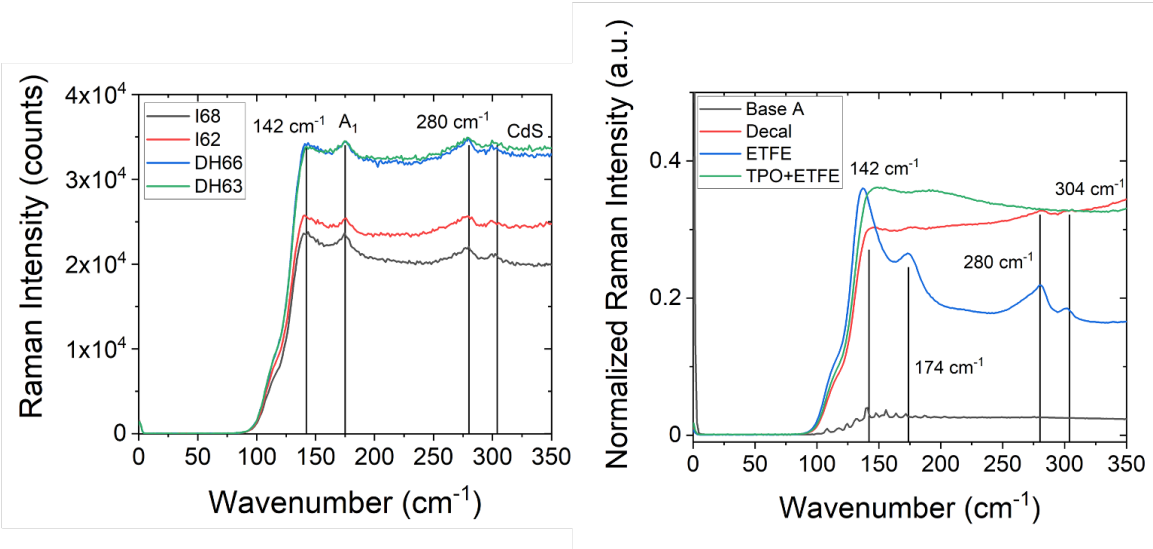

Figure 5.14: Average Raman spectra for the four samples, before light soaking (left). Raman spectra of the encapsulant layers, including the stainless steel denoted as 'decal'. I68, DH66 - high PS; I62, DH63 - low PS.

Although the direct identification of secondary phases that may influence band bending at the contacts is unclear, ERE measurements are still able to clarify if there is any significant influence of contact resistance in any of the devices. Table 5.1 shows the results for the determination of the implied V_{oc} from the ERE measurements of the modules prior to light soaking. The four samples all show similar implied voltages calculated from the ERE results.

Table 5.1: Comparison of Measured Open-Circuit Voltage to Calculated Implied Voltage from ERE in ACIGS Mini-Modules Before Light Soaking

Sample	iV_{oc} (mV)	V_{oc} (mV)	ΔV_{oc} (mV)
Initial, Low PS	660	680	-18
Initial, High PS	668	660	8
DH, Low PS	702	696	6
DH, High PS	689	695	-6

The difference between the implied V_{oc} and measured device V_{oc} are found to be small and within reason of the measurement error (+/- 5mV). This observation suggests that the modules have near-perfect contact selectivity regardless of pre-selenization concentration or dark heat exposure. Near-perfect contact selectivity was also observed for the light

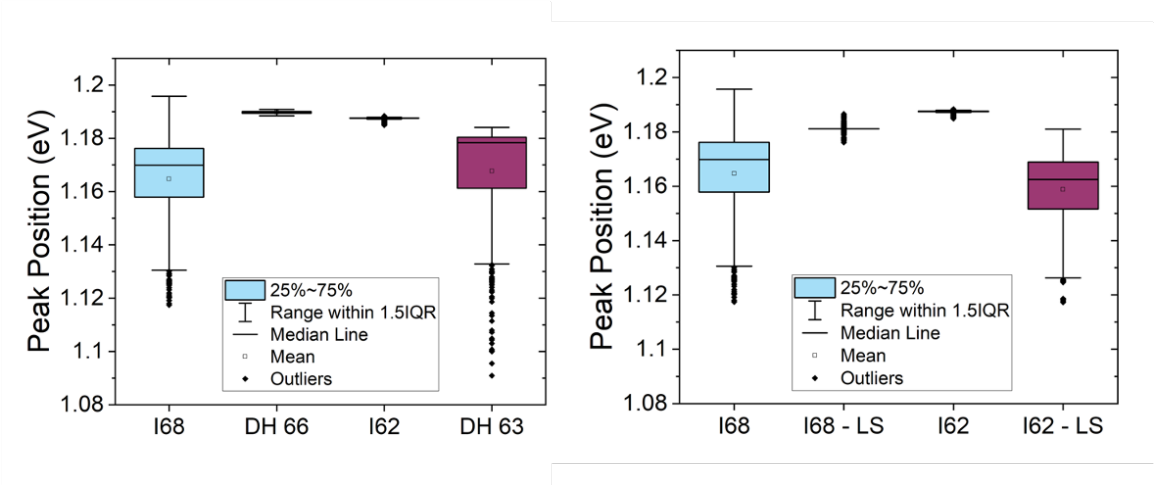

Figure 5.15: PL peak position values calculated from a Gaussian fit of each individual PL spectrum in a 2D PL map of 400 pixels. The left figure compares the change in peak position after the initial samples are dark heated; the right figure compares the peak position after the initial samples are light soaked. I68, DH66 - high PS; I62, DH63 - low PS.

soaked samples. This indicates that the trends in efficiency in Figure 5.2 with light soaking and dark heat are almost entirely caused by the absorber quality itself. In particular, this may further support the hypothesis that metastable defects are responsible for changing the minority carrier concentration after light soaking.

It is important to note that there are limitations to the absolute quantification of the iV_{oc} that may under- or overestimate the actual iV_{oc}. This is exemplified in the initial sample with low PS, which has a large, negative ΔV_{oc} that is hypothesized to arise from inaccurate calculation of the iV_{oc}. The calculation for the implied voltage depends on the theoretical ideal voltage, which is dictated primarly by the absorber bandgap. CIGS absorbers frequently have graded bandgaps that increase in energy toward the center of the absorber due to increased Ga concentration. Bandgap grading makes it difficult to estimate an effective E_g.

The bandgap values used for the estimations in Table 5.1 were found from the average peak position value of 400 PL spectra in each of the modules, taken with a 532 nm green laser. The results from Gaussian fitting of the spectra are shown in boxplots in Figure 5.15.

The mean E_g varies significantly enough between the samples that it influences the iV_{oc} by sometimes 10 mV. The distribution of the calculated E_g for the high PS dark heated sample (DH66) and the low PS initial sample (I62) is very narrow, suggesting a high degree of homogeneity in bandgap for these samples. The other two samples, however, have a wide distribution, which clearly makes it difficult to estimate the bandgap correctly.

The lower estimated bandgap for two of the samples also indicates a difference in the ACIGS composition at the surface near the CdS surface. In particular, a narrower bandgap at the surface would suggest that is additionally Ga-poor and would suggest against the existence of secondary phases such as In_2Se_3 that has a much wider bandgap than CIGS. The compositional variation and corresponding bandgap does not appear to be directly related to the Se pre-selenization concentration, though it may be indicative of how the device responds to dark heat, as the samples showed opposing behaviors with the application of DH. Light soaking was found to influence the bandgap estimations and distributions in the same way as dark heat for the two separate pre-selenization concentrations.

The opposing trend in bandgap with dark heat exposure or light soaking is similar to that from the histograms in the previous sections. The shift to higher or lower Se/Cu concentrations trended oppositely between the pre-selenization groups. Together, these results begin to point selenium content as the origin of the voltage loss. However, taking into the consideration of the ERE results, we can conclude that the impact of Se content is to the absorber quality and not to contact selectivity at either interface. It is likely that the Se content changes the minority carrier population and/or the defect density.

5.5 X-ray Absorption to Study Copper and Selenium Defects

XRF was complimented by X-ray absorption measurements to elucidate the changes in the nearest neighbor environment about the Se atoms. Multiple XANES spectra were taken at the Se absorption edge for statistics. Figure 5.16 shows an example of the XANES

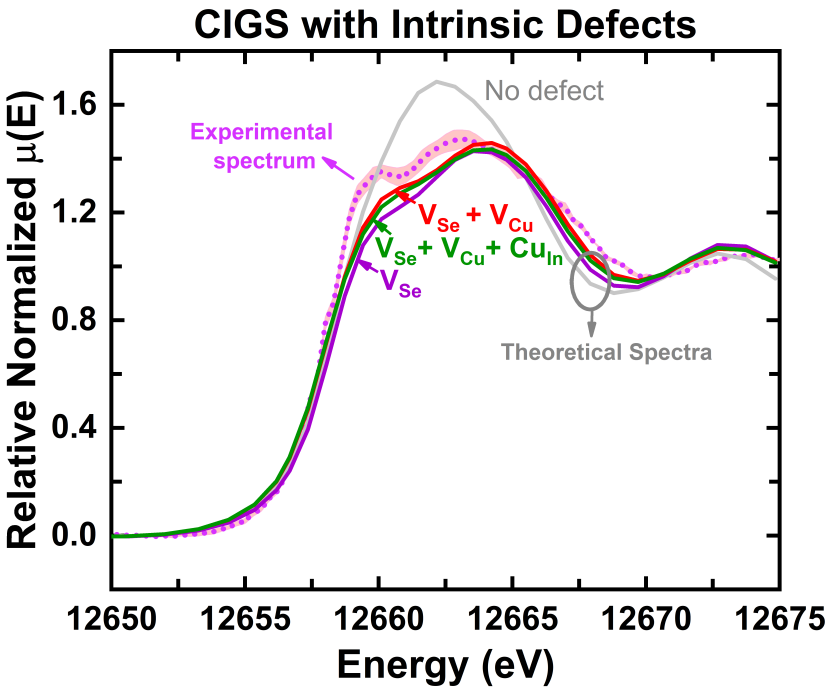

Figure 5.16: XANES spectra of the ideal CIGS structure with no defects (grey), the experimental data of 5 spectra for the low pre-selenization sample before light soaking for the initial case (pink). The shaded border represents the range of the data measured. The solid lines demonstrate the change in the Se XANES spectra with the addition of certain defects. Image courtesy of Srisuda Rojsatein.

measurements taken for the Low PS initial sample. Included in the figure is the theoretical spectrum produced for a pure CIGS structure. The experimental data deviates significantly from the ideal theoretical spectrum, as is expected due to the highly defective nature of CIGS solar cells. The presence of defects was detected in all samples, regardless of the pre-selenization content, the heat exposure (initial or DH), and the light soaking state (soaked or unsoaked).

However, as shown in Figure 5.16, the existence of different defects do change the appearance of the spectra. Their influence is particularly seen as it pertains to the first peak of the Se XANES at 12659 eV. For instance, the first peak becomes sharper with the addition of V_{Cu} to V_{Se}. This demonstrates how the primary information to obtain from

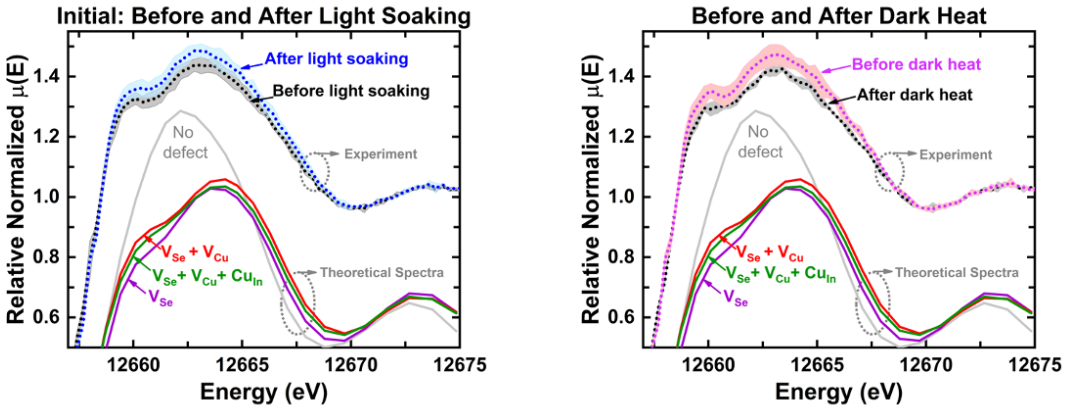

Figure 5.17: Se XANES spectra of the low PS initial sample. Five spectra were measured for each samples and the shaded areas represent the range of the results. The change in the spectra with light soaking (left) and dark heat (right) are shown relative to the corresponding initial case. The solid colored lines (red, green, purple) demonstrate the modeled change in the Se XANES spectra with the addition of certain defects. Image courtesy of Srisuda Rojsatein.

these measurements is through a detailed analysis of the changes in the peak shapes as well as the ratios of the first and second peak.

Figure 5.17 shows the results for the Low PS initial and dark heat Se XANES. The dark heat XANES spectra show a reduction in the variability between measurements as the shaded bands representing the data distribution are narrower. This would suggest that the Se local environment becomes more homogeneous with dark heat exposure. Additionally, the first peak seems to shift to the left and become sharper with dark heat, potentially indicating a relative increase in V_{Se}. The reasoning as to why increased homogeneity may be expected with dark heat needs to be considered as does a more detailed analysis of the ratios of the first and second peak heights as a function of dark heat and light soaking exposure.

5.5.1 Experimental XANES Results in Plan View

Figure 5.18 shows the average Se XANES spectra for the high (left) and low (right) PS samples, before and after light soaking. The general shape of the XANES spectra

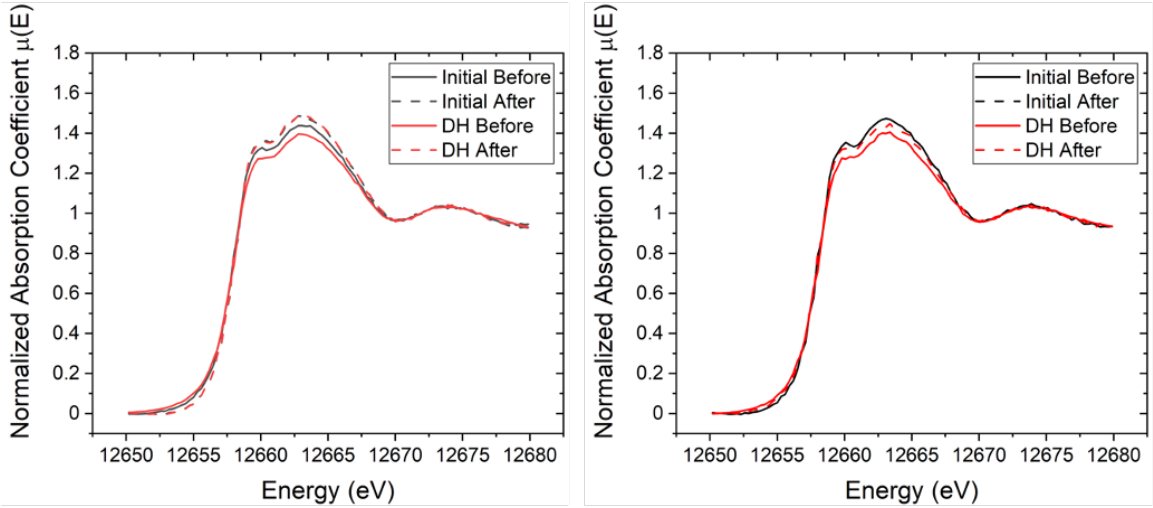

Figure 5.18: Selenium XANES spectra calculated as the average of 5 spectra per sample for the low pre-selenization sample before and after light soaking for the initial and dark heat samples.

indicate that the Se local environment demonstrates similar behavior in the low and high PS situations. The first peak changes most in its sharpness and energy position, seeming to consistently shift to the right after light soaking regardless of the starting condition of the sample. The shift to the right of the first peak was suggested in Figures 5.16 to be from an increase copper vacancies in addition to the already existing Se vacancies.

The spectra shown in Figure 5.18 are the average of XANES spectra taken from different areas of the devices, particularly from both high and low XBIC areas. While subtle changes in the first peak may be noticeable, the averaging of the XANES information in the depth of the device eliminates any nuance in the Se local environment occurring throughout the absorber depth. The elemental migration suggested by the XRF histograms suffered a similar problem due with the plan view measurements. Therefore, the following chapter will look at the XRF distribution and XANES spectra along the depth of the absorber to reveal additional information about the change in the Se local environment particularly at the two ACIGS interfaces.

Chapter 6

CROSS SECTION MICROSCOPY OF METASTABLE DEFECTS

The previous chapter investigated two possible hypotheses for what causes metastable behavior in commercial ACIGS modules. The first is the migration of elements in the depth of the absorber as a function of some external bias, including light or voltage bias. The other is that the predicted copper-selenium vacancy pair, V_{Se}-V_{Cu}, changes in its defect state between an acceptor and donor configuration with the energy provided from light exposure.

Plan view XRF mapping and electrical characterization indicated a slight but significant change in the distribution of Cu and Se concentration as a function of light soaking. The rearrangement of the composition was dependent also on the Se concentration used to create a back surface field on the Mo contact, where samples with low pre-selenization concentration showed a greater rearrangement of Cu atoms than the high pre-selenization case. Furthermore, plan view XANES spectra suggested a potential signature of a change in the defect chemistry with light soaking.

This chapter seeks to directly investigate elemental migration and the metastable defect pair V_{Se}-V_{Cu} by studying devices in cross section before and after light soaking. These two mechanisms are hypothesized to describe the metastable device behavior observed in CIGS upon light soaking and dark heating. A combination of cross section XRF/XBIC and XANES spectra along the absorber depth were used to respectively study the hypotheses. Cross section samples were prepared by cutting 1 cm^2 portions from the modules studied in Chapter 5 and mechanically polishing the exposed absorber edge to create a smooth surface for the XRF measurements. Samples were encapsulated in epoxy to maintain their structure and prevent warping of the steel substrate during polishing. Polishing mats with

decreasing grit size were used without the use of water until the final surface was polished using a 3 μm diamond suspension in ethylene glycol.

As a note, the cross section samples were deemed to be“infinitely thick” to the X-ray beam, meaning that the beam is fully attenuated by the material. This results in an averaging of XRF signal through the cross section. This sample configuration was chosen for a few reasons: 1) to ensure high enough signal of the Se XANES when measured using an only 150 nm spot size; 2) to increase the compositional information by looking at a greater portion of the absorber; and 3) due to limitations in the ability to make very thin samples from encapsulated modules. In other situations, cross section measurements are preferred to be done on TEM windows that are made to be thinner than one grain thick (less than 2 μm in the case of CIGS) because they are better able to resolve individual grain boundaries. This however can result in low signal for both XRF/XANES and XBIC measurements.

6.1 Measurement Background

X-ray fluorescence measurements were done at sector 2-ID-D of the Advanced Photon Source using an incident energy of 12.8 keV (Se_k edge). Measuring at the Se-edge provides simultaneous XRF information on Cu and Se spatial distributions. The same sample areas were measured before and after light soaking for a direct comparison of the changes in composition. Samples were connected using silver paint and metal wiring to the original module metallizations.

An example of the map data is shown in Figure 6.1 for the low pre-selenization sample before light soaking. The white dashed lines are used to delineate the CIGS sample because significant signal was also measured from the top of the module that was facing the XRF detector. The signal from the module surface can be seen to the right of the cross section area. Removing this signal can be extremely difficult as it depends on the sample surface

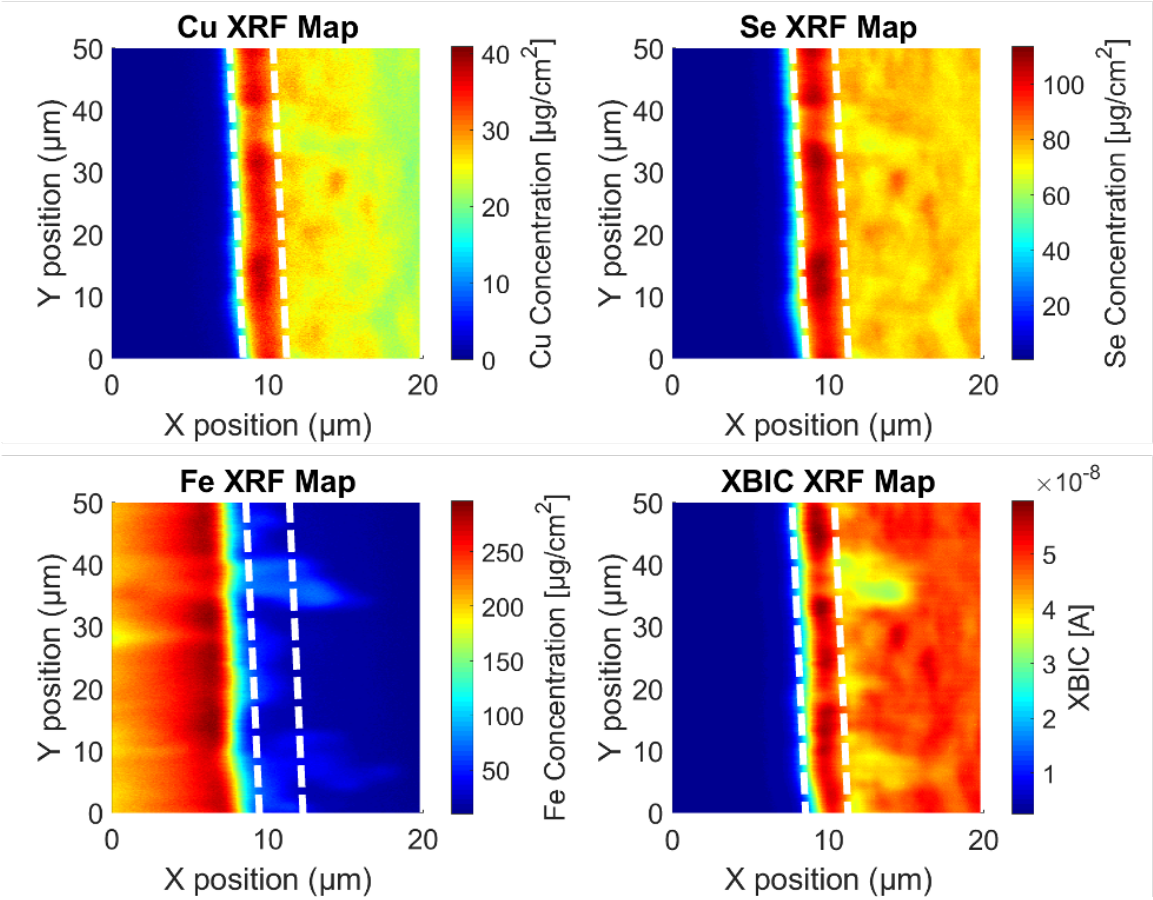

Figure 6.1: XRF maps of Cu and Se (top) and Fe and XBIC (bottom). The sample shown is the initial low PS sample prior to light soaking. White dashed lines are used to delineate the 1.8-2 μm wide ACIGS layer. The fluorescence signal to the right is corresponds to the top of the module.

being perfectly perpendicular to the beam across the entire map. Also in the figure is the map for the Fe signal, which represents the stainless steel back substrate. Not included, but also observable, were the Ti diffusion barrier, the Mo back contact, the CdS junction, and the ZnO TCO.

In the following sections, the XRF and XBIC map data were analyzed by summing the values along the y-axis. The absolute values for the integrated elemental concentrations are useful primarily for identifying and validating the absorber boundary and the Mo and CdS interfaces. The data normalized to the maximum value for each element is more useful in depicting any shifts in the Cu, Se, or XBIC signal.

6.2 Behavior in Low Pre-Selenization ACIGS

Figure 6.2 shows the integration along the y-axis of the cross section maps for the initial low PS case before (top row) and after (bottom row) light soaking. The green dashed lines delineate the same area isolated in the example maps provided in Figure 6.1. In addition to the Cu and Se concentrations, Mo and Cd concentrations were included in the absolute, non-normalized line scans (left column) in order to further mark where the absorber interfaces are.

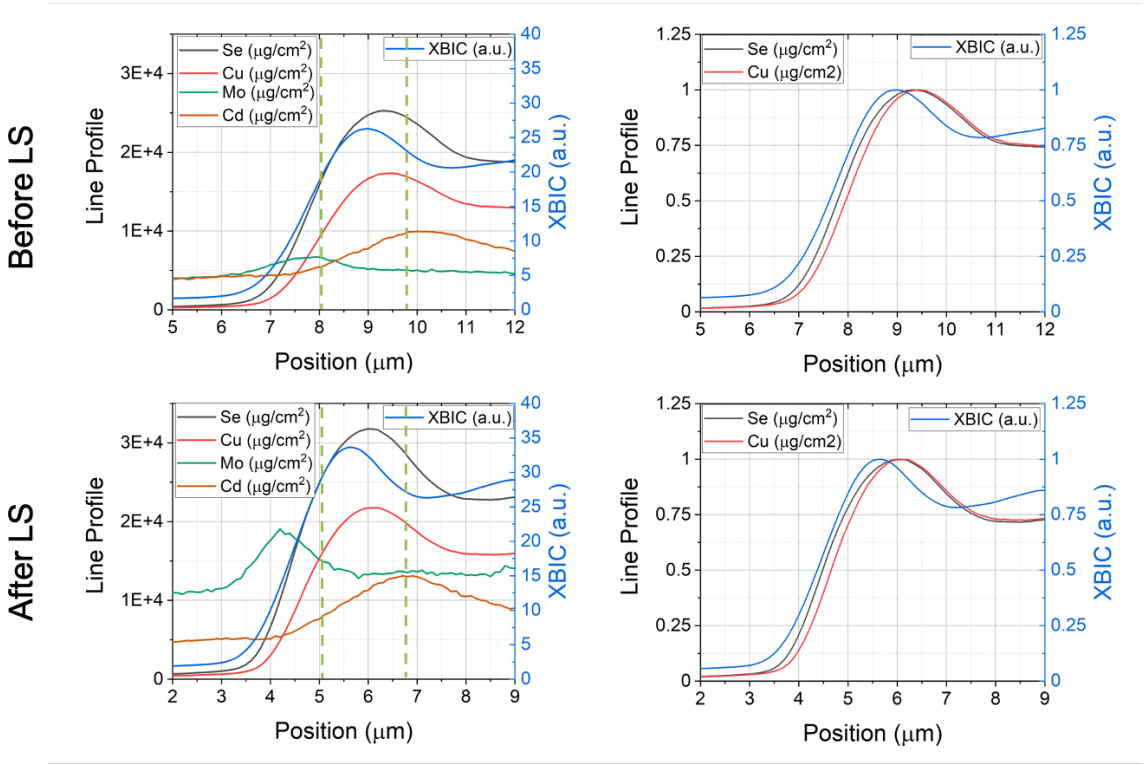

Figure 6.2: Line profiles for the Cu, Se, Cd, and Mo concentrations as well as XBIC signal intensity before (top) and after (bottom) light soaking. The left column is the integrated sum of signal intensity, while the right column shows the normalized profiles. The green dashed lines delineate the ACIGS absorber based on the XRF map and the Cd and Mo peaks.

From the absolute values on the left, it is difficult to observe any significant shifts in the Cu and/or Se positions as a function of light soaking. The right column therefore shows the Cu, Se, and XBIC intensities normalized to their maximum values for direct comparison.

The line profiles before (top) and after (bottom) light soaking appear almost identical. The XBIC peak does not shift after light soaking (it appears slightly offset only due to the slight offset in the centering of the map after light soaking). More importantly, there is no observable change in the maximum Se or Cu concentrations after light soaking. This implies that in the initial sample, with low PS, there is no redistribution of elements along the absorber depth, at least within the sensitivity of the XRF measurements.

The histogram shifts observed in Figure 5.9 showed a significant decrease in the mean Cu concentration with light soaking. Contrasted against the cross section results for the initial low PS sample with light soaking, we conclude that any redistribution of Cu occurs in the lateral direction within the absorber. A lateral rearrangement of atoms in the sample is also supported by the previously shown PL results (Figure 5.15). It was the initial low PS that became significantly more inhomogeneous in terms of bandgap after either dark heat or light soaking. As the measurements are surface-sensitive 2D maps, the boxplot data are more representative of lateral changes within the map area than any changes in the bandgap throughout the absorber depth (measurement only sensitive to the first 80-100nm).

A lack of elemental migration was not demonstrated instead for the dark heat case with low PS. Figure 6.3 shows the normalized line profiles for the dark heat sample before (left) and after light soaking (right). The signal for the lines is not as well defined in the initial case due to natural bending of the substrate during the dark heat treatment. The normalized lines clearly show that prior to light soaking, the Cu concentration is greatest near the Mo and stainless steel substrate. After light soaking, however, the Cu migrates back into the absorber to align almost exactly with the Se concentration.

The movement of Cu, rather than Se, is supported by the boundaries of the Mo and Cd that were used to define the absorber. Furthermore, theoretically Cu is significantly more likely to be the most mobile atom in CIGS. This was observed by Gartsman *et al.* in CIS [81, 82]. Separately, it has been shown that modulating the Na doping concentration helps

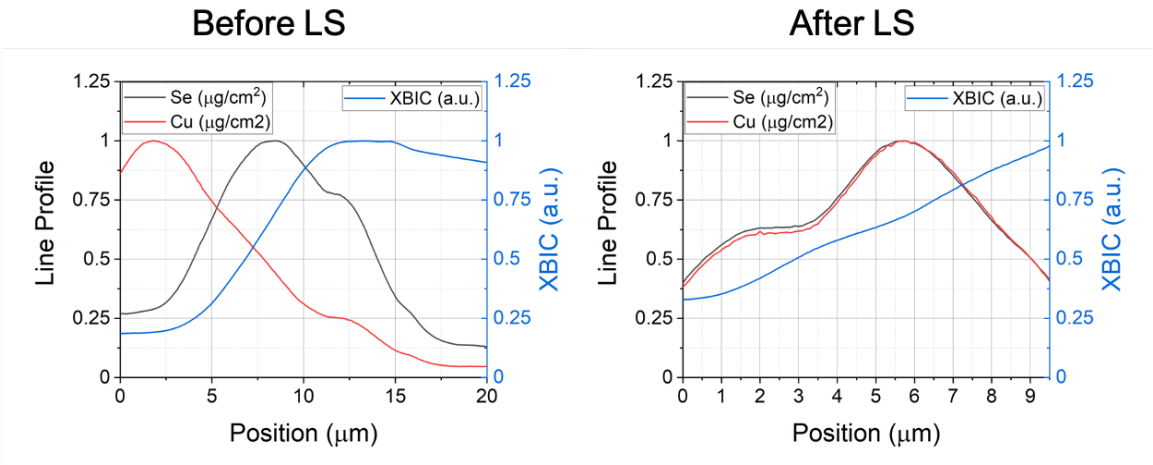

Figure 6.3: Normalized integrated line profiles of the dark heat low PS sample before (left) and after light soaking (right).

to regulate ion migration in CIGS [185]. And lastly, Cu is similarly a very mobile species in CdTe devices [186, 187].

The XBIC signal is blurred in the after light soaking figure potentially due to degradation. It may also represent a shift in the XBIC signal toward the CdS interface. Due to the limitation of the width of the scan, it is not possible to visualize if the XBIC does peak to the right or is blurred out due to the sample. The XBIC signal for the sample prior to light soaking also suggests the signal is focused toward the CdS interface. This is in opposition to what was observed for the initial case, where the XBIC signal peak was slightly away from the ACIGS absorber center toward the Mo-side of the device.

6.3 Behavior in High Pre-Selenization ACIGS

The integrated line profiles for the high PS samples are shown in Figure 6.4. The Cu distribution in the initial case is very skewed from the Se distribution prior to light soaking. After light soaking, the position of the Cu is shifted toward the back of the device, near the Mo interface and the steel substrate. At the same time that the Cu moves, the peak in XBIC signal also shifts slightly toward the Mo interface, away from the CdS interface.

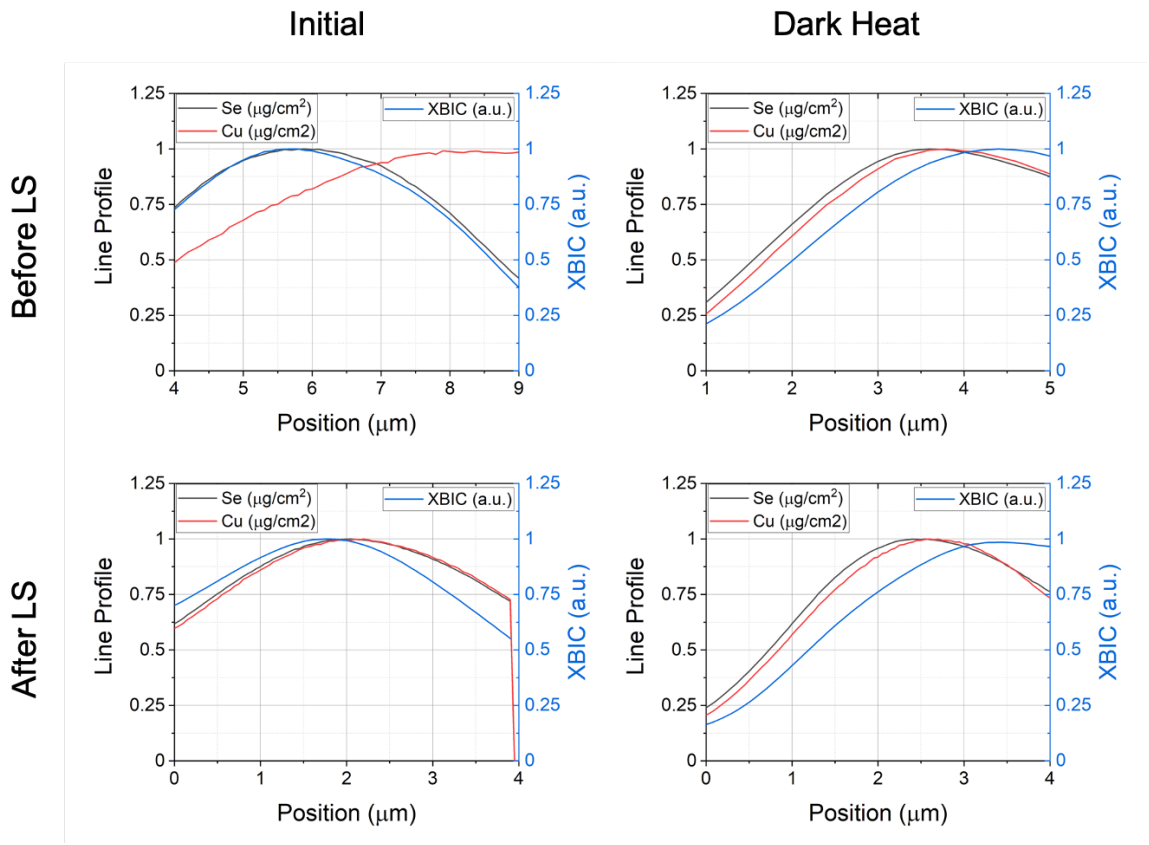

Figure 6.4: Normalized integrated line profiles of the initial (left) and dark heat (right) high PS sample before (top) and after light soaking (bottom).

No change in Cu or Se distribution is observable for the dark heated case. The line profiles for Cu and Se appear consistent before and after light soaking. The XBIC signal instead shifts slightly toward the CdS interface in the light soaked case. This would imply a potential increase in the minority carrier concentration near the CdS, which can be influenced by the change in the electronic configuration of the V_{Se}-V_{Cu} defect pair. This again follows the trend that nano-scale observations in XBIC appear to trend in the opposite direction with light soaking depending on whether the sample was dark heated or not.

A shift in composition only for the initial case and not the dark heated is in agreement with the histogram observations in Section 5.2.1. In the plan view measurements, only the initial case showed a significant shift in composition, which was observed more strongly

in the Se channel. The dark heat composition both in plan view and cross section therefore remained unchanged. This may suggest that the process of dark heat helps to stabilize the composition of the device in the case of high PS content. This is also supported by the significant reduction in the range of calculated bandgap values for this sample.

The mean bandgap value of the initial high PS sample was found to increase upon light soaking. This would suggest that as Cu moves away from the absorber surface, where the PL measurements are sensitive, the bandgap becomes larger, which is in agreement with DFT calculations by Zhao *et al.* that concluded devices with less Cu (or increased Ga) have larger bandgap energies [188]. The movement of copper corresponding to a movement of XBIC also in the same direction implies there is a change to the bandgap that is affecting the generation. Instead, in the dark heat case, the XBIC signal shifts slightly toward the CdS interface despite no observable change in the composition. This indicates more likely a change in either recombination or carrier concentration, both of which could be altered as a result of the V_{Se}-V_{Cu} defect pair.

Similar results for the XBIC peak position were observed in the plan view measurements. The mean normalized current for the initial case shifted down upon light soaking, whereas it shifted up in the dark heated case. The shift in intensity observed for the plan view combined with the knowledge of the peak XBIC position from the cross section measurements demonstrates the influence XBIC position has on XBIC signal measured. Also, the shift in XBIC being unaccompanied by a change in the composition suggests that a change in defect chemistry rather than elemental migration is what is driving the performance changes. If this is the case, it should be made clear by the cross section XANES results that will be discussed in the following section.

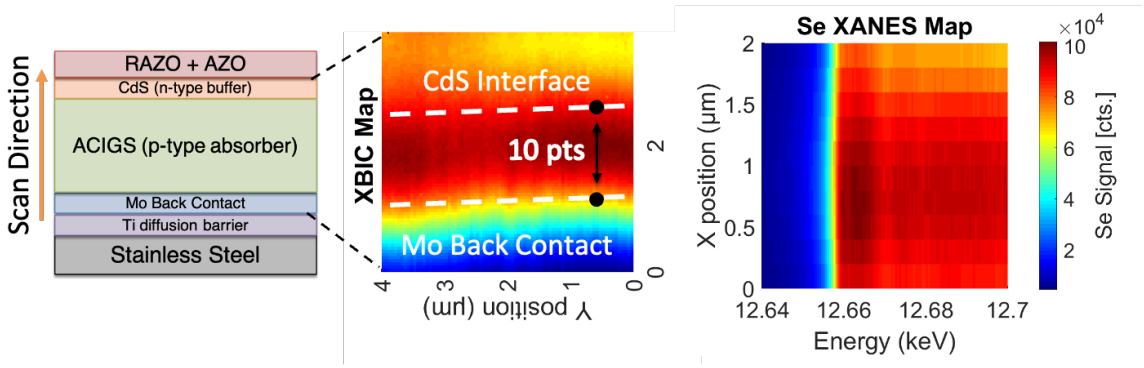

Figure 6.5: A graphical representation of the XANES measurement procedure across the ACIGS absorber and interfaces. The left shows a schematic of the device section viewed in cross section, the center image is of the XBIC signal of the greater ACIGS region, which includes the Mo back contact and the CdS interface. The right image is the point-by-point XANES along the absorber position versus the energy in keV around the Se edge.

6.4 Investigating Metastable Defects by Cross Section XANES

In addition to elemental migration being a potential contributor to light-induced metastability in $Cu(In_{1-x}Ga_x)Se_2$ devices, metastable defects may exist simultaneously or independently of elemental migration. Cross section Se XANES measurements were done of the same samples shown previously, along the same areas. Spectra were taken in steps of 200-400 nm starting on the Mo back contact and across the 2μm thick absorber into the CdS interface. Measurements were deliberately done of the Mo and CdS to understand the appearance of the Se XANES in the absence of significant Se concentrations.

At each point, 60 eV (+/- 30 eV) was measured about the Se absorption edge at 12.67 keV. Figure 6.5 provides a graphic of the measurements as they were done. The map of the XBIC signal in the center delineates where the CIGS absorber was positioned. The white dashed lines outline the 2 μm thick map region of the XANES spectra. The surface plot to the right demonstrates the collapsed XANES spectra line-by-line from the Mo contact (bottom row) to the CdS interface (top row). Towards the middle of the map, the increase in the signal around 12.66 keV is attributed to the center of the ACIGS absorber and represents the strongest signal from the Se XANES. This method of visualization can be useful in future

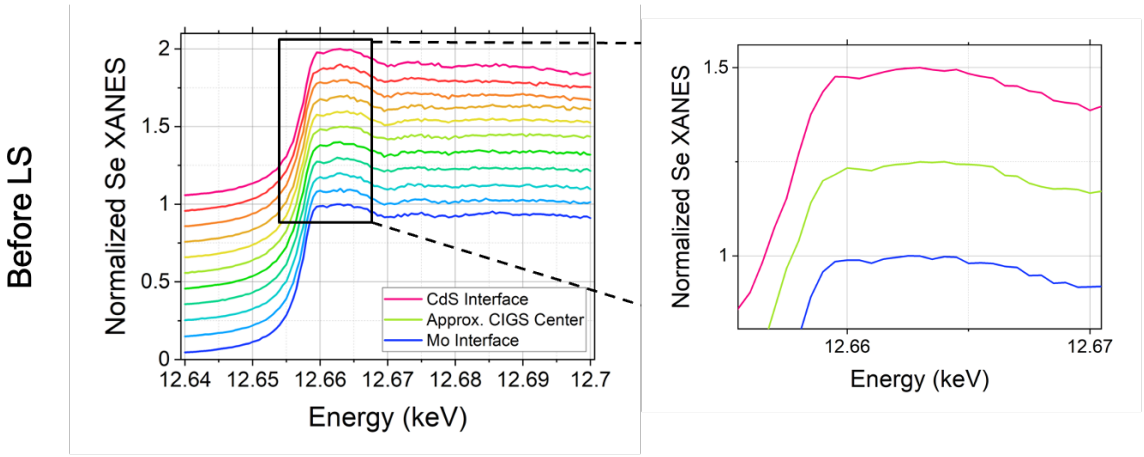

Figure 6.6: XANES spectra across the initial low PS absorber from the Mo interface (blue) to the CdS interface (red). The right figure is a zoom of first peak from the top, bottom, and middle spectra to demonstrate the change in the shape of the peak.

work that incorporates machine learning techniques for spectral unmixing to quantitatively estimate the concentrations of the defects present.

6.4.1 Low Pre-Selenization

In the low PS sample, only the dark heat case showed any elemental migration with light soaking. The use of cross section XANES may help to determine if elemental migration is a connected or an isolated process from the proposed metastable defect behavior involving V_{Se}-V_{Cu}. Figure 6.6 shows the XANES spectra taken point-by-point moving across the ACIGS window from the side of the Mo back contact toward the CdS junction. The figure on the right is a zoom of the first peak of the XANES spectra, where the majority of the changes with light soaking and with absorber position are observed. This again is hypothesized to be due to a change in the relative defect concentrations as was shown in Figure 5.16.

Measuring XANES in cross section clearly provides more evidence than the summary information provided from the plan view measurements. While the plan view measurements indicated just a shift to the right and a sharper 1st peak with light soaking, the cross

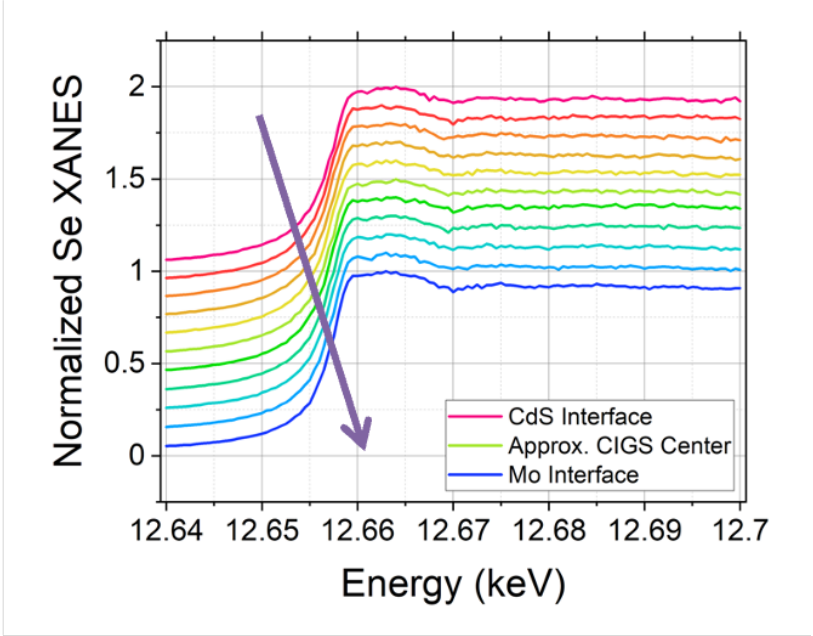

Figure 6.7: XANES spectra taken along the ACIGS cross section for the initial low PS case after light soaking. The purple arrow shows the inversion of the trend in the peak shape compared to the un-light soaked conditions.

section data shown here has a clear, but subtle transition from one peak shape to another. The peak toward the CdS interface is right shifted in the un-light soaked case and then devolves to a left-shifted, rounder peak moving toward the Mo. Based on the theoretical estimations in Figure 5.16, this observation suggests increased copper vacancies toward the CdS interface. This is unsurprising as it is often expected that CIGS absorbers be Cu-poor at the CdS junction.

Figure 6.7 shows the same spectra taken of the sample after light soaking. In this case, the peak at the CdS interface is now much more round and shifted to the left. Instead, the lines toward the Mo interface, particularly the green lines, are much more pointed in shape. The last few lines toward the Mo correspond to spectra taken off of the ACIGS absorber, evidenced by the disappearance of the spectral features. With this, it seems as though the Cu-poor surface is altered after light soaking.

The observation of a change in the defect concentrations across the absorber depth is

in contrast to the lack of elemental migration observed in this sample. This implies that light soaking behavior in the low PS initial case comes almost entirely from a change in defect density. Following the Lany-Zunger model for V_{Se}-V_{Cu}, the change in relative concentrations of the two defects would cause a change in the minority carrier population as the defect switches from a shallow acceptor to a shallow donor[67]. The change in carrier population would be seen in the J_{sc}, which was the case for all of the light soaked situations. As a reminder, in Figure 5.2, the J_{sc} was reduced upon light soaking for all of the samples regardless of pre-selenization concentration or dark heat exposure.

Figure 6.8 shows the similar analysis for the dark heated low PS sample before and after light soaking. The left column shows the spectra normalized to the maximum Se signal for each spectrum with the lines stacked by 0.1. The right column instead shows the spectra without the offset. The XANES spectra for the DH case do not show any significant variation before and after light soaking. In both cases, the peak becomes more shallow moving away from the Mo back contact. This sample showed Cu migration with light soaking. The results for the initial and dark heat would suggest then that elemental migration and metastable defects occur independently and may inhibit each other.

6.4.2 High Pre-Selenization

Based on the behavior observed in the low PS sample, it is hypothesized that the initial sample in the high PS should demonstrate no defect metastability, as it had instead demonstrated Cu migration. Figure 6.9 shows the XANES spectra for the initial sample before and after light soaking. The shape and position of the first peak does not appear to change with the position within the absorber. Rather the peaks, and therefore the defect chemistry, appear to be consistent across the sample and change in shape uniformly after light soaking. The results imply that though the defect concentrations are changing with light soaking, potentially connected to the V_{Se}-V_{Cu} defect pair, they do not change within the

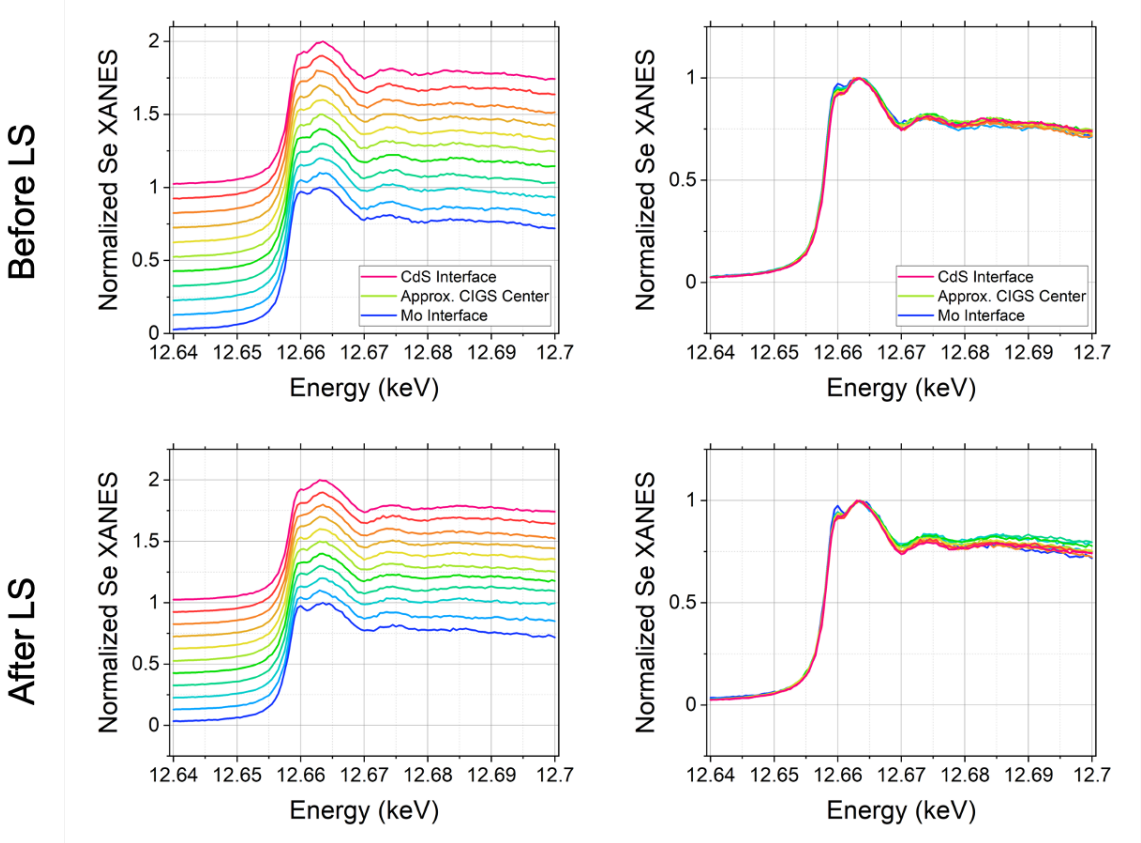

Figure 6.8: XANES spectra taken along the ACIGS cross section for the dark heat low PS case before and after light soaking. The left column demonstrates the spectra using an offset of 0.1. The right column demonstrates all of the data overlayed.

absorber itself and should not be responsible for the shift in XBIC signal seen in Section 6.2.

This change is slight and may be within the statistical error of the measurement. Quantitative analysis will be required to estimate what changes in defect concentrations are necessary to produce the observed peak shifts. Only then can defect metastability in the high PS initial case be ruled out. However, based on the previous observations, it is possible that the initial high PS showed minimal change in the defect chemistry due to the Cu migration previously observed.

In the case of the dark heat sample, shown in Figure 6.10, the first peak appears to have an inversion in shape after light soaking, similarly to the initial low PS case upon light

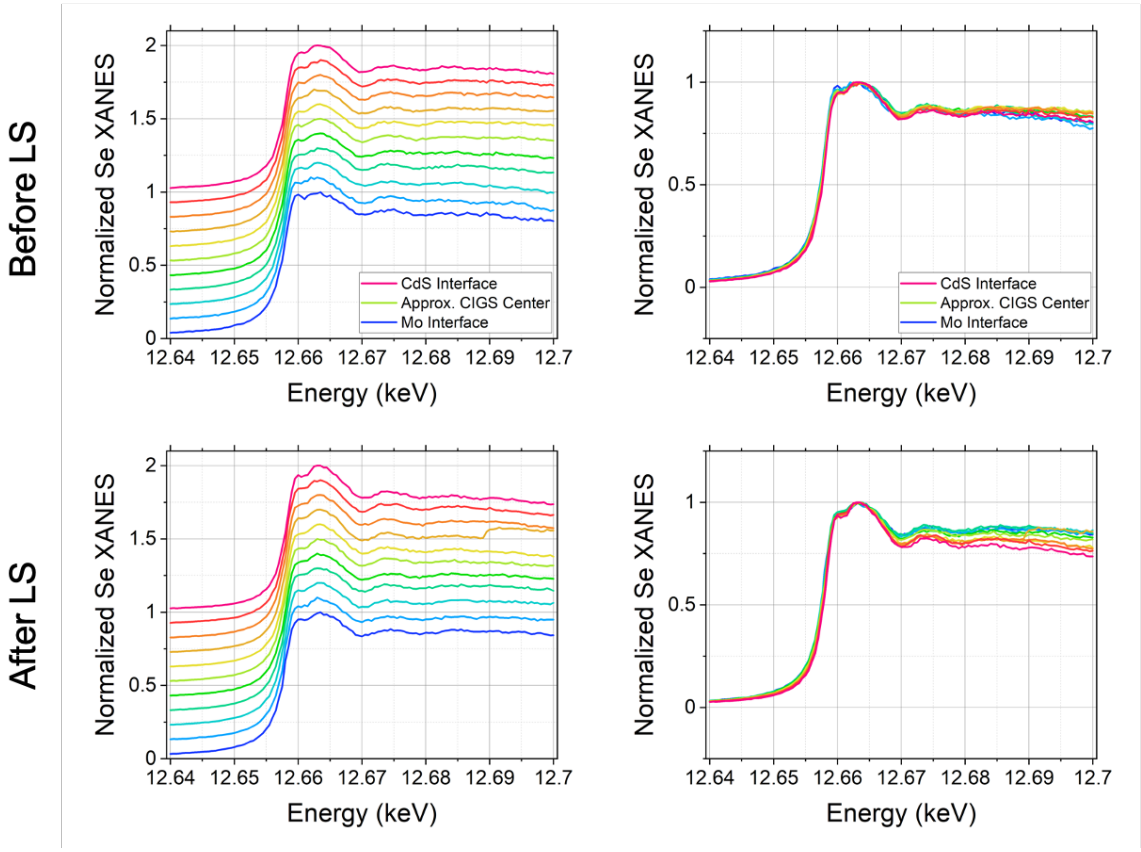

Figure 6.9: XANES spectra taken along the ACIGS cross section for the initial high PS case before and after light soaking. The left column demonstrates the spectra using an offset of 0.1. The right column demonstrates all of the data overlayed.

soaking, again showing that there are similarities between the two. Before light soaking, the first peaks near the Mo interface appear rounded; after light soaking, they become more pointed and pronounced. The second peak also becomes broader for some spectra after light soaking, indicating a change in the second nearest neighbors to Se.

The difference in the shape and height of the first peak across the absorber also becomes more dramatic with light soaking of the DH sample. Where the overlaid spectra of the Se XANES before light soaking show a nearly consistent first peak shape (Figure 6.10, top right), after light soaking (Figure 6.10, bottom right) the first peak shows changes between the CdS in red and the CIGS absorber center in green. A similar discrepancy in the first peak across the absorber was found for the high PS sample but before light soaking. After

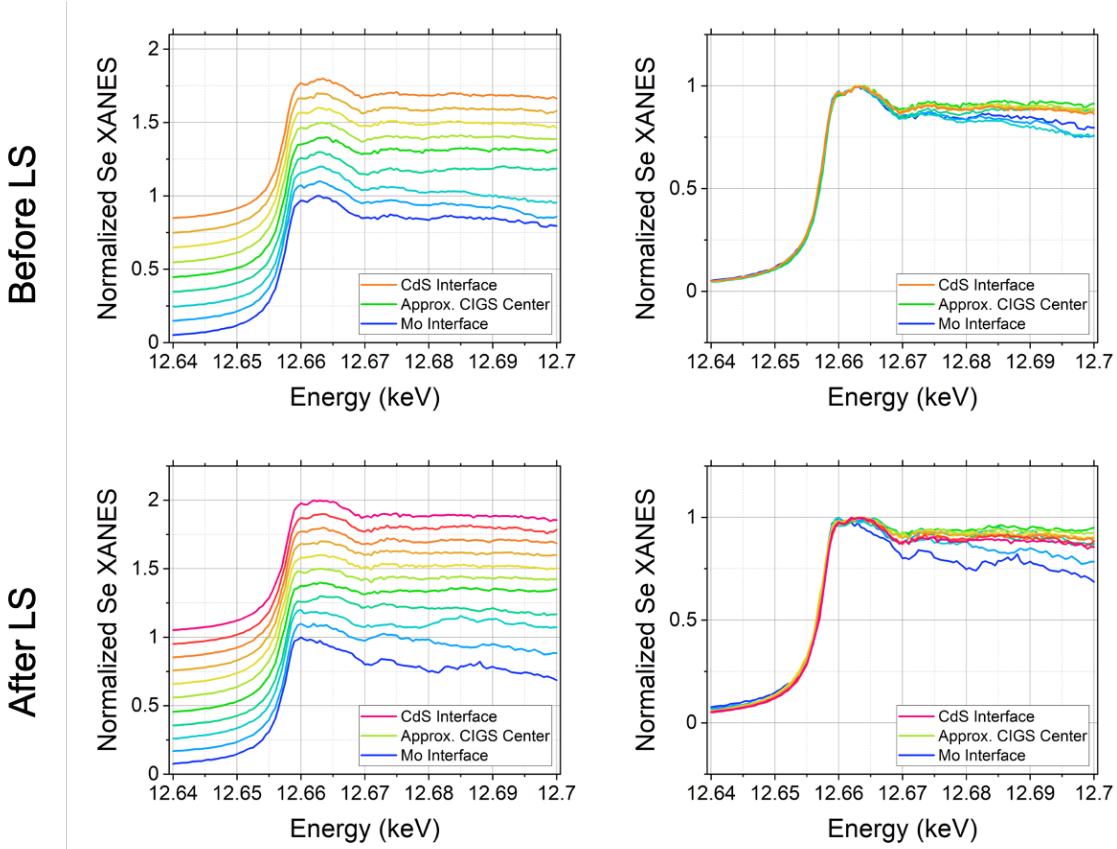

Figure 6.10: XANES spectra taken along the ACIGS cross section for the dark heat high PS case before and after light soaking. The left column demonstrates the spectra using an offset of 0.1. The right column demonstrates all of the data overlayed.

light soaking, instead, the first peak became more similar across the absorber.

This shows there is a change in the local environment within CIGS that changes with light soaking. It also shows that the response to light soaking is influenced by whether or not the sample was dark heated. This finding seems connected to the observations made in Figure 5.2 that demonstrated light soaking causes reduced V_{oc} in the initial high PS sample, but instead causes recovered V_{oc} for light soaked dark heat samples. A priori, this could mean that a grading of the local Se environment across the absorber, rather than a homogenization of the local environment, benefits the device V_{oc} through some mechanism. Fitting the XANES spectra will provide more information on what exactly the offset of the first peak across the absorber means with regards to local environment and

defects. In the future, the results from fitting can also be correlated to results from the XBIC signal that is measured simultaneously with the Se XANES.

6.4.3 Simulation of Defects from Se XANES

Linear combination fitting can be used to quantifiably evaluate the change in defects upon light soaking and depending on the location in the absorber depth. In order to do so, an improved understanding of the simulated CIGS structure is required. The spectra in Figure 6.11(top left) show the simulated perfect CIGS crystal expected for a structure with 100 Se atoms. The relaxed structural models were optimized using density-functional theory (DFT) and the XANES spectra were then simulated using FEFF-9 [189]. The simulated spectra for the perfect crystal are shown as the colored lines and retain the appearance of only one peak as was previously shown in Figure 5.16. Also included in black is an example of the experimental spectra obtained for the previous measurements; spectrum shown is for the initial high PS sample prior to light soaking.

Next, common defects in CIGS were simulated for their affect on the simulated XANES spectra with a focus on V_{Cu} and V_{Se} and also Cu_{In} interstitials, which are also anticipated defects though they are frequently considered to be electronically neutral [58, 190]. The results of the simulated spectra that result from certain defects and concentrations are seen in the remainder of Figure 6.11. The same experimental spectrum is included in each sub-figure for comparison to the shape change in the spectra resulting from the respective defect. For instance, the addition of 10 selenium vacancies appears to be responsible for a pointed first peak, as was observed in some of the experimental data of the previous sections.

From the simulated defect structures, linear combination fitting can be used to find the combination of spectra with distinct defect concentrations that best fit each of the experimental spectra. In the CIGS chalcopyrite structure, Se is four-coordinated, with two sites

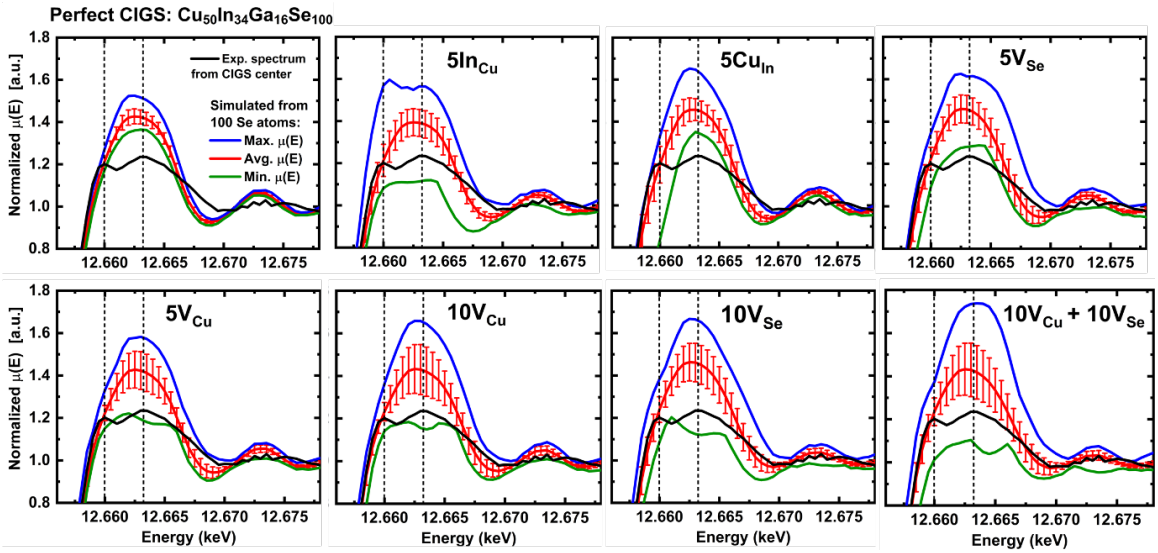

Figure 6.11: Simulated XANES spectra for the perfect CIGS crystal with 100 Se atoms (top right) and then with various quantities of commonly reported CIGS defects. Blue and green curves simulate the maximum possible signal and the minimum possible signal. The black curve in all figures represents an example experimental spectrum acquired. Dashed lines highlight the two peaks found in place of the first peak for the experimental spectra for reference. Results courtesy of Srisuda Rojsatein.

belonging to Cu and the remaining two being some combination of In and Ga depending on the In:Ga ratio. The second nearest neighbors of Se are 12 Se atoms.

Figure 6.12 shows the breakdown of the calculated ratios of Cu, In, and Ga first nearest neighbors to Se in the high PS initial sample, before (top) and after (bottom) light soaking. Looking firstly at the Cu results, there is a clear difference in the number of Cu nearest neighbors present between the Mo interface and the CdS interface. The further away from the Mo and into the CdS side of the device, the increasing concentration of 2Cu and 1Cu neighbors, where 2Cu indicates there are 2 Cu atoms as the nearest neighbor, 1Cu is one nearest, and 0Cu implies a Cu vacancy. On the other hand, the Mo side has increasingly 0 Cu nearest neighbors.

The concentrations of Cu neighbors to Se are also changed after light soaking. The change overall seems to come from a general reduction in Cu vacancies, which occurs more significantly toward the CdS interface than the Mo back contact. Toward the Mo

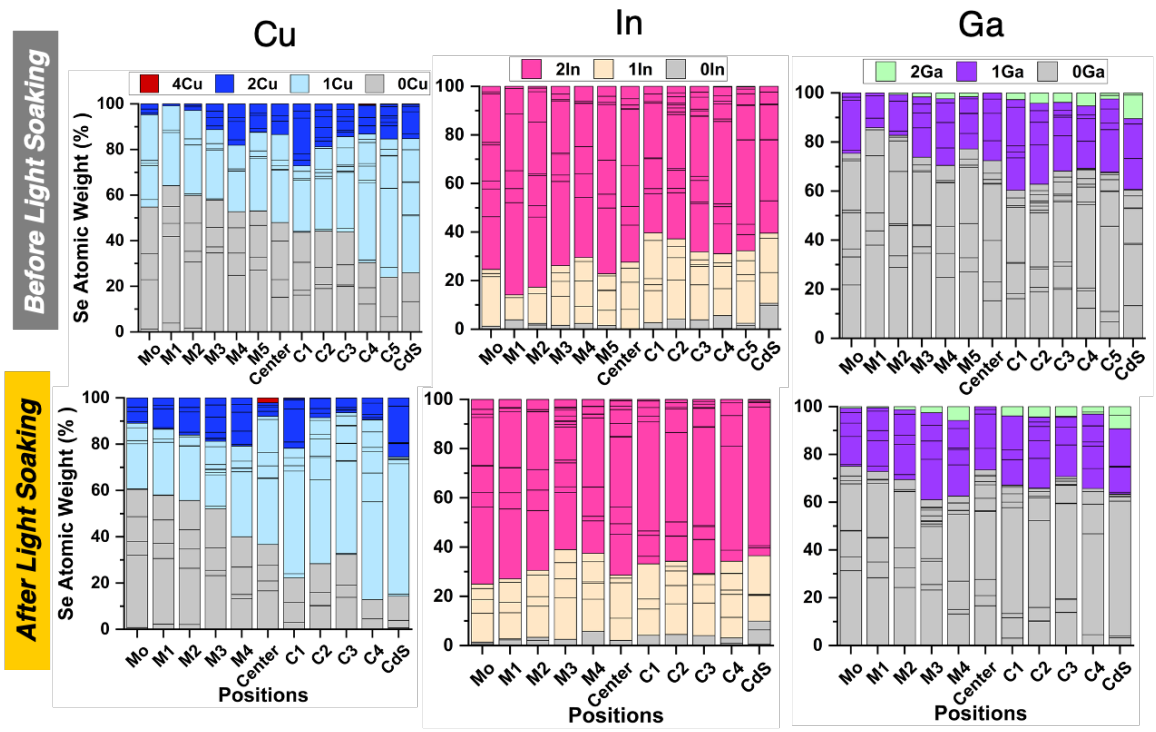

Figure 6.12: Linear combination fitting results for the first nearest neighbors to Se. In the ideal chalcopyrite structure, Se has four nearest neighbors, of which two Cu atoms (2Cu) are anticipated and the other two sites are shared by In and Ga. A 0 indicates a vacancy. Results courtesy of Srisuda Rojsatein.

contact, there is an increase in the number of 2Cu. This is compensated by a significant decline in Cu nearest neighbors toward the center of the absorber. The change in Cu nearest neighbors alone can point to a rearrangement of atoms upon light soaking.

Changes to the In nearest neighbors to Se (center column of Figure 6.12) change minimally with light soaking, but the existence of 1 nearest neighbor does increase toward the Mo contact with light soaking. There is little evidence at all to In vacancies and a major part has 2 In nearest neighbors, implying a $CuInSe_2$ structure. The opposite is true for the Ga nearest neighbors, where the majority is attributed to Ga vacancies, followed by 1 Ga nearest neighbor. Inversely to the In, there is very little existence at all of 2Ga that would imply a $CuGaSe_2$ phase, though the concentration of 2Ga does increase subtly toward the CdS interface. Overall, the changes in the In and Ga nearest neighbors occur much less

significantly with light soaking than those of Cu.

Similar observations in the change in type of defect across the absorber as well as the change in concentration after light soaking was found for In and Ga related defects. These findings are critical in that they directly demonstrate the existence of metastable defects upon light soaking. Expanding the analysis to also look at the second nearest neighbors shows in addition to a change in type of defects present, there is an inverse shift in Se and Cu defects with light soaking. In the initial high PS samples, a decrease in Se atoms as the second nearest neighbor was found after light soaking, which was paired with an increase in Cu atoms, at the Mo back contact. This is exactly like what was found from the cross section XRF line profiles that showed a shift of Cu toward the back of the device, away from the CdS, upon light soaking.

Figure 6.13 shows instead the calculated second nearest neighbors to Se center atoms for before (top) and after (bottom) light soaking of the initial high PS sample. The left column is the weight percent of Se second nearest neighbors to Se, of which 12 are expected in the perfect crystal. The results show the majority of the the Se nearest neighbors are 11 or 10 atoms and relatively zero Se center atoms are perfectly neighbored by 12 Se atoms. The empty sites are then either filled with interstitial atoms or are left as vacancies. After light soaking, the device overall has a greater proportion of Se center atoms that have fewer Se second nearest neighbors.

The reduction in Se second nearest neighbors after light soaking corresponds with a significant increase in two Cu second nearest neighbors. The change happens most toward the CdS interface, where also the greatest concentration of fewer Se second nearest neighbors (red) occur. The changes to the Cu atoms indicate a rearrangement of the structure. In the nearest neighbors to Se, one-fewer Cu atoms were found near the CdS interface. In the second nearest neighbors, however, 2Cu were increasingly observed near the CdS.

The change in the Se second nearest neighbors contains more nuance than can be ex-

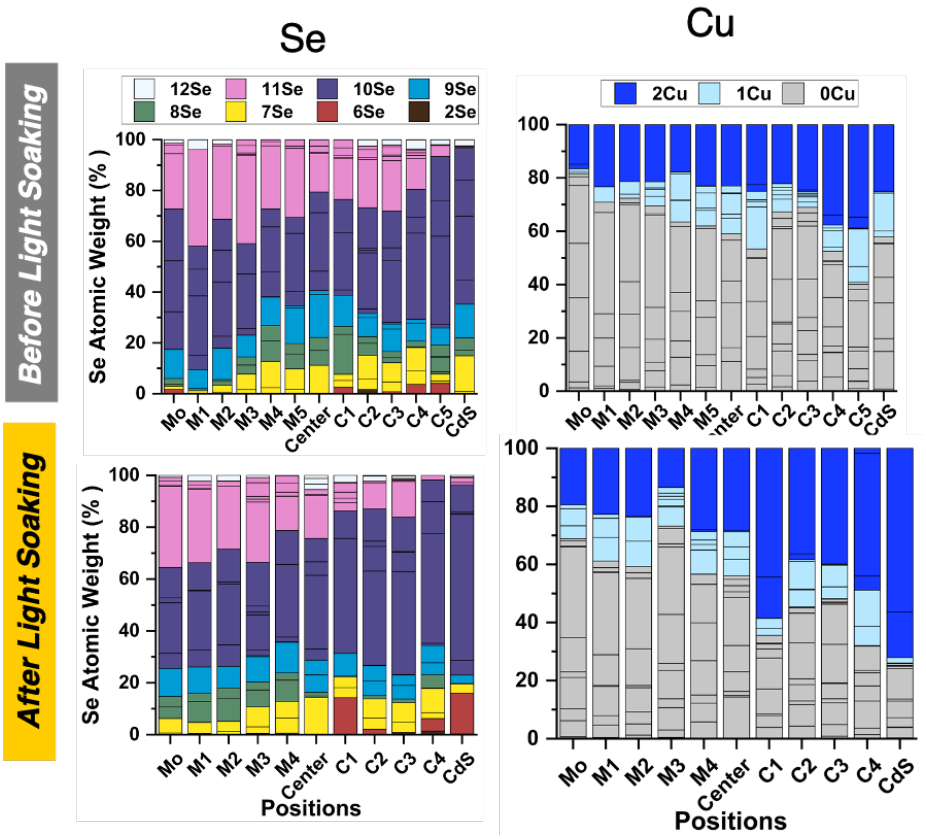

Figure 6.13: Linear combination fitting results shown as the atomic weight percent of the number of Se atoms with each type of second nearest neighbor. In the ideal chalcopyrite structure, Se is expected to have 12 second nearest neighbors that are all Se atoms (white bar). Results courtesy of Srisuda Rojsatein.

tracted solely by the comparison to Cu. Being that there are 12 total sites that can be filled as second nearest neighbors to Se, the change between 6 and 10 Se neighbors can result from any combination of changes to the other elements. In the future, greater analysis can be completed to form a full understanding of the changing chemical environment. These results so far demonstrate that there is a clear influence of light soaking on the chemical environment in the absorber.

Similar analysis of the low PS sample is needed in order to elucidate if the results observed are directly related to the elemental migration of Cu or occur strictly from a change in localized defect metastability. Furthermore, expanding the analysis to the dark heat sam-

ples will demonstrate if dark heat plays a role in metastable defects or if the XANES spectra of the dark heat samples are influenced by distortion in the lattice.

Chapter 7

INTERPRETING X-RAY BEAM INDUCED VOLTAGE

This chapter addresses some considerations as to how to conduct and interpret X-ray beam induced voltage (XBIV) measurements in compliment to the measurement of nano-scale electrical signal by means of X-ray beam induced current (XBIC). In particular, an understanding of what device characteristics (e.g. V_{oc} or J_{sc}) are represented when only a narrow relative fraction of a solar cell is under illumination, as is the case in nano- and micro-scale induced current or voltage measurements. A number of theoretical and experimental approaches were considered in order to develop a deeper understanding of X-ray beam induced current and voltage and the significance of the relationship between the two.

Generally, induced current measurements are well accepted to be representative of local J_{sc}, which is possible in part due to the linear relationship existing between illumination and current [36]. At the same time, however, lifetime is not linearly related to the injection level, represented by the excess minority carrier concentration (Δn) [36]. Compared with current measurements from current-density curves, which use a broad spectrum 1-sun light source, induced current measurements often use a monochromatic incident source with differing power densities. This suggests that a direct translation of the results from any induced current measurement to J_{sc} is still not fully accurate.

One example that demonstrated the limitations in interpretation was work by Jin and Dunham that observed simulated EBIC signals that increase at grain boundaries, but were not found to correspond to greater device I_{sc} [191]. This finding comes also in part due to the narrow spot size used in EBIC measurements. While one of the benefits of induced current measurements is often the narrow spot size that allows for spatial information of the electrical performance, it also serves to complicate the interpretation of the results as

they pertain to bulk device characteristics.

As beam spot sizes are reduced down to μm or nm, the majority of the cell then remains in the dark and this is critical to consider in the interpretation of XBIV and XBIC measurements. Localized current measurements are easier to interpret because it is normalized to the cell area measured. Thus, induced current measurements are still a direct measurement of the carrier collection efficiency that have the added benefit of spatially resolved information on defects and inhomogeneties [192, 193].

Voltage measurements using only partial illumination instead certainly do not relate directly to macro-scale V_{oc} measurements due to the impact of the majority of the cell being in the dark. For thin film devices that have a transparent conducting oxide (TCO) layer, the partial illumination forces an averaging of the quasi-fermi level splitting (QFLS) to occur across the entire device [171]. Vishnoi *et al.* experimentally demonstrated the impact of partial illumination on solar cell parameters using single crystal n^+-p silicon solar cells. The results show that an averaging of voltage occurs as expected, however it is limited by the resistive load of the dark region. This occurs because carrier movement is no longer happening only perpendicular to the junction as is the expected case in full-field illumination, but rather laterally as well [194]. The impact on V_{oc} and J_{sc} was found to be greater when the top contact was in the shaded region. This should not be an issue, however, in thin film solar cells where the top contact is a TCO covering the entirety of the cell.

One way to address this is by biasing devices using a full-field illumination. As an example, El-Hajje *et al.* mapped the QFLS of a CIGS device using calculations from PL with the sample under a source of even illumination equivalent to 450 suns [195]. This is similar to the setup used for the ERE measurement described in previous chapters. It is important to note that as of the time of this writing, all XBIC/XBIV measurements were done in the dark, using no bias lighting and therefore the considerations necessary for the

appropriate interpretation of the results are addressed herein.

7.1 Simulating the Impact of Illumination Size on Device Parameters

An initial understanding of how device parameters scale with illumination area was simulated using the open-source program Quokka [196, 197]. The program solves carrier transport equations in quasi-neutral silicon devices; other programs such as Sentaurus are more appropriate for solving more elaborate situations where the excess electron and hole concentrations are not approximately equal, as well as situations where 2D modelling is required.

The simulations were done using a 150 μm thick, n-type monocrystalline Si solar cell with interdigitated back contacts (IBC) to reduce the impact of shading. The bulk resistivity was held constant at 0.1 Ωcm. The minority carrier lifetime was set to 2.9 ms. Additional parameters including the diffusion and metal geometries were the same as those listed in Table VII of [198].

Figure 7.1 shows the simulated IV parameters (efficiency, V_{oc}, J_{sc}, and FF) as a function of the illumination coverage fraction (x-axis), or the percentage of the cell area illuminated where 100% is equivalent to 1-sun illumination. For a reference, samples studied for XBIC with a spot size of 150 nm were on average 1 cm^2 in active area, which would result in an illumination coverage fraction of <0.01%. For each set of simulations, a range of contact resistivities (ρ_c) were studied. To evaluate the impact of the dark saturation current, J_0, two separate values of "good" (=0 A/cm^2) and "bad" (10^{-10} A/cm^2). Note that in the figures, the x-axis is logarithmic, and therefore the shapes of the lines are in agreement with solar cell equations for the dependence on injection (current is linear, voltage is logarithmic).

The impact saturation current can be clearly seen for its affect on the V_{oc}, where there is an reduction of over 50 mV for a bad J_0. This is unsurprising as it follows directly from the diode equations for a solar cell [36]. Instead, the J_{sc} is largely unaffected by

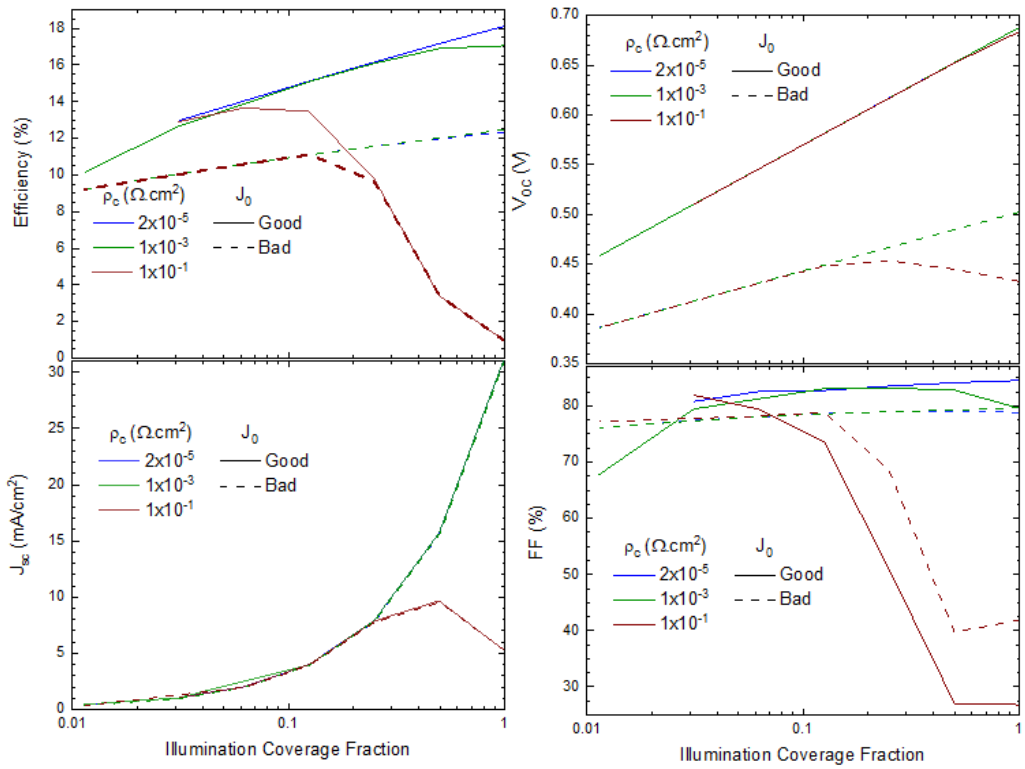

Figure 7.1: Simulated J-V characteristics under 1-sun illumination, efficiency (η), V_{oc}, J_{sc}, and fill factor (FF), as a function of illumination coverage fraction and as they depend on contact resistance (ρ_c) and dark saturation current (J_0). Results courtesy of Barry Hartweg.

the saturation current. Even contact resistance is does not have much impact unless under close-to full illumination conditions, where the majority of the cell is generating current, and only when the contact resistance is especially high. A similar effect of especially high contact resistance tanking the V_{oc} is noticeable as well, simply highlighting the general need for reasonable contacts to be able to extract proper IV curves.

The results in Figure 7.1 for the low illumination coverage fraction show only a difference in the V_{oc} depending on the dark saturation current. The dark saturation current is a descriptor of recombination and depends in part on the material bandgap, but is also found to increase significantly in CIGS with increasing electrostatic potential fluctuations [155]. Electrostatic potential fluctuations were observed previously in Chapter 4 and were

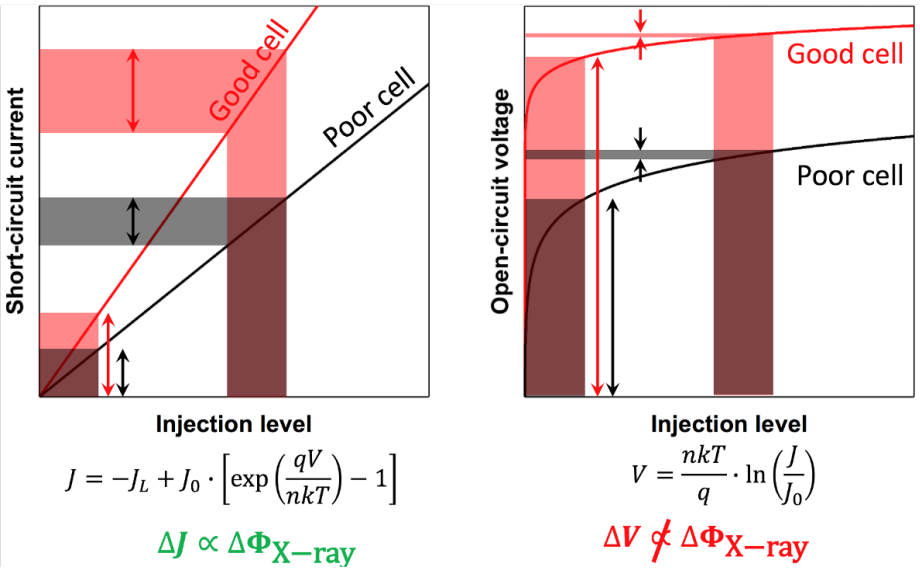

Figure 7.2: Calculated values of J_{sc} and V_{oc} for a good and poor cell as a function of injection level. The equations used are shown below. Figure courtesy of Michael Stuckelberger.

concluded to arise due to inhomogeneities in the CIS when treated for both Ag and KF. Therefore, by producing higher quality devices, for instance through optimizing Ag and KF, it is possible to minimize the saturation current. One such example was shown by Karki *et al.* that studied RbF treated CIGS and found that the alkali treatment successfully reduced the saturation current [199].

The dependence of the current and voltage on injection level is shown again in Figure 7.2. Here, the curves are calculated from the solar cell equations (shown on the bottom) without any modeling. The figure shows a comparison between a good performing and poor performing cell and the expected short-circuit current (left) and open-circuit voltage (right). Due to the linear dependence of the current on injection level, the range of J_{sc} values (shown as the horizontal shaded boxes labeled with arrows) follows linearly, where despite the injection level, the good cell has a greater range of J_{sc} than the poor cell. The right of Figure 7.2 instead shows the V_{oc} and its logarithmic dependence on injection. Depending on the injection conditions, the range of V_{oc} can actually be larger for the poor cell than the good cell, seen for the higher injection level situation. This suggests that XBIV

measurements, which are considered to be low injection conditions for CIGS, are not directly proportional to the V_{oc} of the device under test. J_{sc} and XBIC should be proportional, as was shown in both Figure 7.1 and 7.2.

It is therefore more complicated to relate XBIV measurements to the bulk parameters, in part due to its dependence on dark saturation current and in part due to the logarithmic dependence on injection level. For the time being, the most effective way to utilize the XBIV data is by focusing only on relative changes within individual maps and directly correlating to XBIC. Only once injection level studies of XBIV have been completed will there be a better understanding of its appropriate interpretation.

7.2 Interpreting Correlative XBIC/XBIV

Determining the appropriate way to interpret results from XBIC vs. XBIV measurements depends on an understanding of the device J-V parameters prior to measuring. This means that, first, an understanding of the losses of the device (shunt resistance, series resistance, and dark saturation current) need to be considered. This is partly because the efficiency of devices with higher shunt resistances is reduced to a lesser degree in low injection conditions than devices with low shunt resistance. This is well exemplified in the case of concentrator solar cells, that demonstrate the higher the shunt resistance under cloudy conditions, the less the device efficiency is reduced based on the injection level [200].

On the other hand, under high injection conditions, devices become more dependent on their series resistance[200]. Thus it is also important to calculate the approximate injection conditions expected for the absorber type (CdTe, CIGS, perovskites, etc.). This is done by first measuring the flux of the X-ray beam used for the electrical measurements. A calibrated PIN-diode is used to detect the X-ray photons downstream of the X-ray optics. The signal from the pin diode, in counts, is measured with the beam on and off and the

difference is calculated to remove the background signal from the actual signal induced by the X-ray beam.

The flux can then be converted to an approximate value for the injection level by converting the counts to V, a value set by the beamline for the scalar channels, and then V to A based on the Stanford pre-amplifier settings used[124]. The signal now in amps is multiplied to the calibrated sensitivity of the pin-diode (measured to be 2178 photons/s/pA at the Se-edge at 12.8 keV) to calculate the photon flux in photons/s.

Lastly, using the Equation 7 from Stuckelberger *et al.* for the material-specific correction factor and multiplying it by the incident photon flux calculated before, the injection level of the X-ray beam can be estimated [34]. For the majority of the experiments described herein, which used an incident X-ray energy above the Se-K edge, a photon flux of approximately 5E8 photons/s was calculated. This equates to an injection level in the range of 1E12 cm^{-3}.

For CIGS, doping densities are frequently in the range of 10^{15} to 10^{16} cm^{-3}[201, 202], but may even be up to 10^{18} cm^{-3}[127]. This means that most likely, X-ray beam induced electrical measurements are operating under low injection conditions, and the more susceptible the measurements are to the shunt resistance. Similar to what was concluded for the dark saturation current, the sensitivity to shunt resistance should be equally applied to the device, meaning that relative changes in higher or lower XBIV signal do represent a true observation.

With this information, we conclude that the comparison of *relative* changes in XBIC or XBIV maps are representative of local variations in J_{sc} and V_{oc}. An example of the direct correlation of XBIC and XBIV *within maps* is demonstrated in Figure 7.3. The example shows the correlation of XBIV to XBIC for the low PS modules studied in plan view, before (left) and after (right) light soaking. The appearance of the correlations before and after light soaking (comparing corresponding left and right images) can be directly

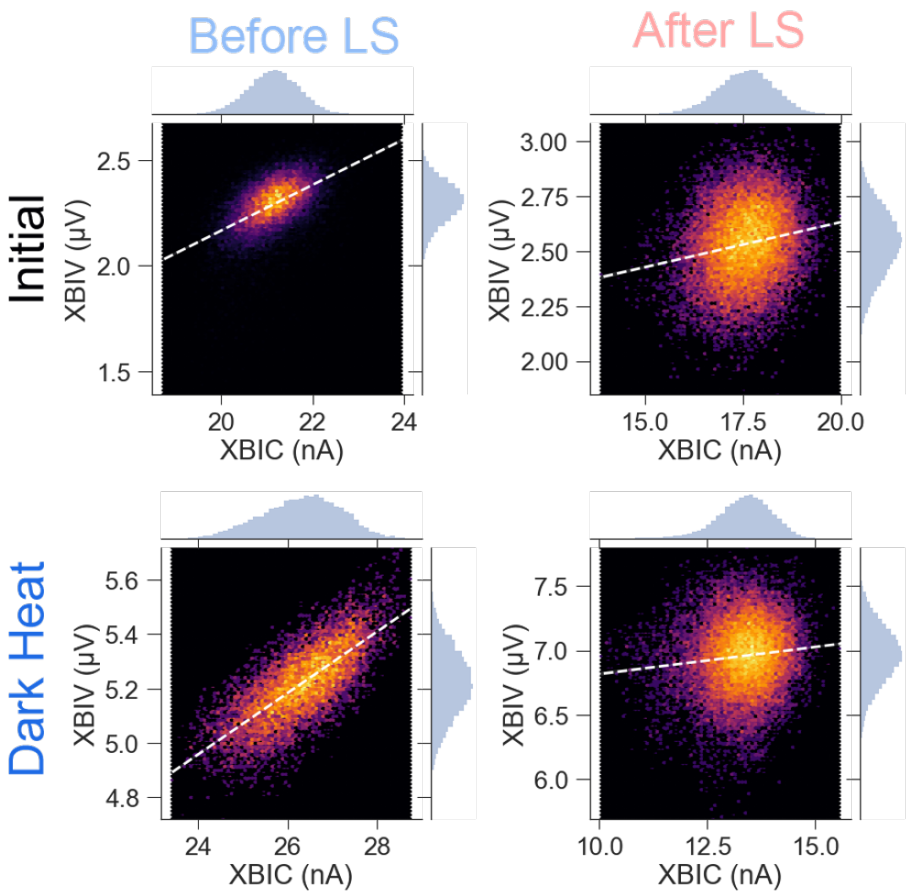

Figure 7.3: Hexbin plots to show the correlation of XBIV vs. XBIC for the initial (top) and dark heat (bottom) low PS sample before (left) and after (right) light soaking. Increasing brightness from purple to yellow indicates a greater denisity of data points within the pixel bin. Dashed white lines are the least mean square regression.

compared as they are taken from the exact same samples, in nearby areas, using the same lock-in settings.

The correlations indicate a clear change in the electrical behavior after light soaking and occurring independently of dark heat exposure. The slope of the correlation becomes more flat with light soaking, which suggests that the current current is no longer as spatially related to the voltage. The slope flattening out is a result of both the XBIC and XBIV signals becoming broader. Both signals become broader to create a rounded cluster of data, and the line, calculated by least mean squares, only minimizes the distance of the points from the line. Therefore, what is primarily occurring is the broadening of these signals in

2D space.

From the histograms in Figure 5.12 for the low PS case, we observed an increased the width for both XBIV and XBIC with light soaking. Since the electrical measurements are done using a lock-in amplifier, the signal observed is dependent upon the optical chopper frequency and the measurement dwell time. If the two parameters are not well matched, the transient decay of the electrical signal can be observed. What we can conclude from the increased distribution of the histograms and the broadening of the hexbin plots is that the diffusion length of the carriers has changed. This is because the lock-in parameters were maintained exactly the same, including the chopper frequency, and thus an increase in the broadness of XBIC/XBIV comes from carriers traveling farther than before and contributing to a ”blurred” image.

An increase in diffusion length with light soaking has recently been proposed by other groups as well [25]. In the work by Nikolaeva *et al.*, the diffusion length was found to increase after even brief light soaking, which was attributed to the filling of defect states close to the CdS buffer interface. The observation in XBIC/XBIV of increased diffusion length also corresponds with preliminary XANES findings that there is a change in the defects present at the CdS interface after light soaking.

Separately, in both the initial and dark heat samples, the XBIC signal is reduced overall after light soaking. The fact that the lower XBIC does not correspond with lower XBIV suggests that it is not driven by an increase in recombination, but rather must come from a change in the minority carrier concentration after light soaking. This may also be connected to the change in defects and their position in the absorber after light soaking, as was proposed by the XANES results.

Similar work done by Heise *et al.* observed an almost directly opposite trend in CIGS. With light soaking, samples instead showed an increase in minority carrier concentration and at the same time, a reduction in diffusion length [73]. These behaviors were concluded

to compete against each other, resulting in a simultaneous increase in V_{oc} and decrease in J_{sc}. Though the trends in minority carrier concentration and diffusion length were found to be opposite to those observed here, it is very likely that this arises from a difference in composition. In particular, the study of pre-selenized CIGS films changes the chemistry of the absorber and the resulting defect concentrations quite significantly compared to samples with no excess Se.

While this chapter has sought to address some of the considerations necessary for nano-scale electrical measurements, additional progress is required for a complete understanding of how to connect multi-scale characterization techniques. Studying samples directly for diffusion length or lifetime as a function of light soaking would be useful. While the slope and distribution of the XBIC and XBIV are most likely equally informative of changes in diffusion length, the XBIC signal is more sensitive to changes in the minority carrier concentration and diffusion length. The addition of contactless measurements such as ERE and PL are also highly necessary prior to the interpretation of XBIC/XBIV results in that they describe if the X-ray electrical measurements are dominated by the absorber quality, similarly to what has been discussed here, or if they are dominated by contact resistances. This section focused only on changes in the absorber quality because previous ERE measurements shown in Section 5.4 demonstrated no issues with contact quality for these devices.

Chapter 8

CONCLUSIONS

The goal of this work was to apply an array of characterization techniques in order to understand the impact that the incorporation of additional elements to $Cu(In_{1-x}Ga_x)Se_2$ thin film solar cells has on the film properties and the resulting device performance. The use of a multi-scale characterization framework demonstrated its ability to highlight the primary sources of reduced performance in an otherwise complex and intricate material system.

The proposed framework can be broken into primary characterization techniques and secondary ones. Primary techniques are those that should be used in almost every instance to create an initial understanding of the film quality and the device. Included here is the use of current-voltage measurements (IV), external radiative efficiency (ERE), and photoluminescence (PL) to diagnose the absorber quality for recombination and the quality of the contact selectivity. ERE in particular is the ideal starting point for characterization by indicating whether the performance is limited more by the contacts or by the absorber properties. This was demonstrated by the ERE of ACIS+KF samples versus commercial ACIGS samples. While the ACIS+KF V_{oc} loss was able to be attributed to the contact quality through ERE, commercial modules instead showed the device properties were almost entirely described by issues in the absorber quality.

The addition of nano-scale XRF and XBIC/XBIV is also useful in complimenting the conclusions from ERE/PL. The simultaneous mapping of the film composition and device performance allows for the identification of compositional inhomogeneities and their connection to collection efficiency. In general, 2D mapping techniques provide additional information than generalized measurements such as ERE and IV. XBIC/XBIV mapping

can be used to identify local shunted regions, defect clusters, or pinholes due to incomplete film coverage (as can be the case for CdS).

One major challenge to correlative X-ray microscopy (XRM) is the limited sample areas studied. Increasing measurement speeds at various beamlines are allowing for higher through-puts and therefore increased statistics, however, the area studied relative to the device size remains small and limits how representative such measurements can be, especially in the case of commercial modules. Therefore, complimenting nano-scale mapping techniques such as XRM with broader scale mapping techniques, such as electroluminescence or full-field photoluminescence can help diagnose shunting and recombination within the entire module but with limited resolution and information.

Secondary techniques may include those such as Raman spectroscopy, X-ray diffraction, and X-ray absorption near edge structure (XANES). They are can be used to identify specifically the sources of recombination, shunting, or limitations in contact selectivity. For example, when ERE indicated that the ACIS+KF sample was limited by contact selectivity and XRM found increased compositional inhomogeneity within the sample, Raman spectroscopy then identified a surface phase of cation ordered chalcopyrite CIS. Secondary techniques take the critical knowledge acquired from primary techniques and specify the defects or phases in the absorber or at the interfaces that are responsible for device performance. Knowing the phases or defects that form then dictates the changes that need to be made to the growth procedure in order to avoid them.

8.1 Recommended Future Work

One area of focus that may be of interest to consider next is the distribution and effect of Ga in CIGS or ACIGS absorbers. Ga-grading in CIGS is frequently used to create a different absorber bandgap throughout the absorber depth. With Ga-doping also comes increased potential defects as well as lattice compression due to the smaller Ga atoms replacing In.

The behavior of Ga could be understood using the same techniques outlined in the document, including X-ray diffraction to look at the structural change with Ga incorporation and Ga XANES to understand the chemical environment, and in turn defects. Injection and temperature-dependent PL measurements would also contribute to a knowledge of the defects states that exist with the addition of Ga, but also Ag and alkali post-deposition treatments.

Raman and PL measurements using multiple incident wavelengths would also provide additional information on the structure and recombination at various points in the depth of the absorber. Herein, only a surface-sensitive, green laser (wavelength 532 nm) was used. However, in Ga-graded devices, the PL results are not representative of the entire device stack and the calculated peak positions actually only account for the surface of the absorber. Incident lasers such as red (633 nm) or near-infrared (785 nm) have greater penetration depths in CIGS. Therefore, it would be ideal to conduct PL and Raman mapping with additional wavelengths.

Lastly, studying the effects of light soaking and dark heat can be improved by increasing the measurement frequency. The multi-scale characterization framework should be applied to devices and cells light soaked for different time scales, from a minutes to a few hours. This is necessary to address the knowledge gap of the time scale of defect metastability. As of this writing, it is unclear how quickly defects change in their electronic state and how quickly they are capable of returning to their initial state. The same is true for sample dark heating. Dark heating for 1000h is not a feasible time length if dark heating is to be used as a potential field process for undoing the effects of light soaking during module operation. Therefore, the minimum time required for dark heating to recover device performance should be understood.

8.1.1 Sample Preparation and Measurement Work-flow

The ability to directly correlate measurements of various length scales is still limited due primarily to the inability to identify the same measurement regions across characterization techniques. This is in part due to the measurements themselves, which identify different material properties (e.g. composition from XRF vs. recombination from PL) and that do not necessarily have the same features. Furthermore, the change in resolution also results in features being more or less visible depending on the measurement spot size. To aid in cross-measurement compatibility, the advancement of fiducial markers is required. This is especially important for larger devices, such as mini-modules.

8.1.2 Improving XBIC/XBIV Measurements

The considerations for XBIV in Chapter 7 demonstrate the benefit that can come from conducting XBIV measurements under light bias. In doing so, the XBIV measurement can become sensitive to spatial variations the quasi-fermi level splitting. Detailed analysis should be done in the future to evaluate the difference in spatial resolution and spatial correlation to XBIC found from doing biased and un-biased XBIV measurements.

More reliable electrical contacting can also help with improving the overall results achieved from XBIC/XBIV measurements. Limitations exist as to the use of Ag paint particularly to the extent that its application can cause local shunting to the device. Deposited metal contacts or metal wiring such as busbars help to reduce the risk of device damage by the use of Ag paint.

Little understanding exists as to the importance of the distance between the metallizations and the measurement area. The electrical measurements are in part limited by the minority carrier diffusion length, the contact resistivities (especially of the TCO), and the contact selectivity. XBIC signal may be effected by the distance between the X-ray beam

and the contacts. Therefore, an experimental study of XBIC and XBIV as a function of spacing between metallization is recommended.

8.1.3 Data Analysis and Processing

Significant improvements can be made to reduce data processing times by the automation of data analysis and visualization. Specifically, the Python and MatLab codes used for handling the data should be generalized to allow for more variation in the measurements obtained. The addition furthermore of more "intelligent" tools, such as appropriate clustering algorithms and machine learning techniques should be evaluated and selected. The same is true for a faster approach to image registration.

Even with the use of fiducial markers, image registration is required for more exact analysis and correlation of map data. As repeated maps are taken, for instance XBIC then XBIV maps or PL then Raman maps, stage precision is not enough to ensure that the maps are perfectly overlaid. By correcting for shifts in repeated measurement areas, the strength of the pixel-by-pixel correlation can be improved, but current approaches for image registration often involve a high degree of user input.

REFERENCES

[1] L. Cozzi, O. Chen, H. Daly, A. Koh, Population without access to electricity falls below 1 billion – Analysis, en-GB, Library Catalog: www.iea.org, 2018.

[2] U. C. Bureau, Estimated 7.58B People on Earth on World Population Day July 11, EN-US, Library Catalog: www.census.gov Section: Government, 2019.

[3] Annual Energy Outlook 2020 with projections to 2050, 2020.

[4] D. S. Philipps, F. Ise, W. Warmuth, P. P. GmbH, 2020, 48.

[5] T. D. Lee, A. U. Ebong, Renewable and Sustainable Energy Reviews 2017, 70, 1286–1297.

[6] F. Haase, C. Hollemann, S. Schäfer, A. Merkle, M. Rienäcker, J. Krügener, R. Brendel, R. Peibst, Solar Energy Materials and Solar Cells 2018, 186, 184–193.

[7] K. Yoshikawa, W. Yoshida, T. Irie, H. Kawasaki, K. Konishi, H. Ishibashi, T. Asatani, D. Adachi, M. Kanematsu, H. Uzu, K. Yamamoto, Solar Energy Materials and Solar Cells, Proceedings of the 7th international conference on Crystalline Silicon Photovoltaics 2017, 173, 37–42.

[8] E. E. Perl, J. Simon, D. J. Friedman, N. Jain, P. Sharps, C. McPheeters, Y. Sun, M. L. Lee, M. A. Steiner, IEEE Journal of Photovoltaics 2018, 8, 640–645.

[9] J. F. Geisz, R. M. France, K. L. Schulte, M. A. Steiner, A. G. Norman, H. L. Guthrey, M. R. Young, T. Song, T. Moriarty, Nature Energy 2020, 5, 326–335.

[10] F. Kessler, D. Rudmann, Solar Energy, Thin Film PV 2004, 77, 685–695.

[11] P. Reinhard, A. Chirila, P. Blösch, F. Pianezzi, S. Nishiwaki, S. Buechelers, A. N. Tiwari in 2012 IEEE 38th Photovoltaic Specialists Conference (PVSC) PART 2, 2012, pp. 1–9.

[12] A. Polman, M. Knight, E. C. Garnett, B. Ehrler, W. C. Sinke, Science 2016, 352.

[13] M. Stoppa, A. Chiolerio, Sensors (Basel Switzerland) 2014, 14, 11957–11992.

[14] S. Hegedus, Progress in Photovoltaics: Research and Applications 2006, 14, 393-411.

[15] MiaSole Breaks World Record Again: Large Area Flexible Photovoltaic Module with 18.64% Efficiency, en-US, Library Catalog: miasole.com Section: In the News, 2019.

[16] J. Jean, P. R. Brown, R. L. Jaffe, T. Buonassisi, V. Bulović, Energy & Environmental Science 2015, 8, 1200–1219.

[17] G. M. Wilson, M. M. Al-Jassim, W. K. Metzger, S. W. Glunz, P. Verlinden, X. Gang, L. M. Mansfield, B. J. Stanbery, K. Zhu, Y. Yan, J. J. Berry, A. J. Ptak, F. Dimroth, B. M. Kayes, A. C. Tamboli, R. Peibst, K. R. Catchpole, M. Reese, C. Klinga, P. Denholm, M. Morjaria, M. G. Deceglie, J. M. Freeman, M. A. Mikofski, D. C. Jordan, G. TamizhMani, D. B. Sulas, Journal of Physics D: Applied Physics 2020.

[18] S. Siebentritt, Solar Energy Materials and Solar Cells, Special Issue : Thin film and nanostructured solar cells 2011, 95, 1471–1476.

[19] T. Feurer, R. Carron, G. T. Sevilla, F. Fu, S. Pisoni, Y. E. Romanyuk, S. Buecheler, A. N. Tiwari, Advanced Energy Materials 2019, 9, 1901428.

[20] Y. Kawano, J. Chantana, T. Nishimura, A. Mavlonov, T. Minemoto, Solar Energy 2020, 204, 231–237.

[21] A. Chirila, S. Buecheler, F. Pianezzi, P. Bloesch, C. Gretener, A. R. Uhl, C. Fella, L. Kranz, J. Perrenoud, S. Seyrling, R. Verma, S. Nishiwaki, Y. E. Romanyuk, G. Bilger, A. N. Tiwari, Nature Materials 2011, 10, 857–861.

[22] F. Babbe, L. Choubrac, S. Siebentritt, Applied Physics Letters 2016, 109, 082105.

[23] S. Siebentritt, L. Gütay, D. Regesch, Y. Aida, V. Deprédurand, Solar Energy Materials and Solar Cells, Thin-film Photovoltaic Solar Cells 2013, 119, 18–25.

[24] M. Nakamura, K. Yamaguchi, Y. Kimoto, Y. Yasaki, T. Kato, H. Sugimoto, IEEE Journal of Photovoltaics 2019, 9, 1863–1867.

[25] A. Nikolaeva, M. Krause, N. Schäfer, W. Witte, D. Hariskos, T. Kodalle, C.A. Kaufmann, N. Barreau, D. Abou-Ras, Progress in Photovoltaics: Research and Applications 2020, 1–16.

[26] M. J. Hetzer, Y. M. Strzhemechny, M. Gao, M. A. Contreras, A. Zunger, L. J. Brillson, Applied Physics Letters 2005, 86, 162105.

[27] D. Colombara, K. Conley, M. Malitckaya, H.-P. Komsa, M. J. Puska, Journal of Materials Chemistry A 2020, 8, 6471–6479.

[28] B. West, PhD thesis, Arizona State University, 2018.

[29] M. I. Bertoni, D. P. Fenning, M. Rinio, V. Rose, M. Holt, J. Maser, T. Buonassisi, Energy & Environmental Science 2011, 4, 4252.

[30] D. P. Fenning, J. Hofstetter, M. I. Bertoni, S. Hudelson, M. Rinio, J. F. Lelièvre, B. Lai, C. del Cañizo, T. Buonassisi, Applied Physics Letters 2011, 98, 162103.

[31] O. F. Vyvenko, T. Buonassisi, A. A. Istratov, H. Hieslmair, A. C. Thompson, R. Schindler, E. R. Weber, Journal of Applied Physics 2002, 91, 3614–3617.

[32] B. M. West, M. Stuckelberger, B. Lai, J. Maser, M. I. Bertoni, The Journal of Physical Chemistry C 2018, 122, 22897–22902.

[33] M. E. Stuckelberger, T. Nietzold, B. West, R. Farshchi, D. Poplavskyy, J. Bailey, B. Lai, J. M. Maser, M. I. Bertoni, IEEE Journal of Photovoltaics 2018, 8, 278–287.

[34] M. Stuckelberger, B. West, T. Nietzold, B. Lai, J. M. Maser, V. Rose, M. I. Bertoni, Journal of Materials Research 2017, 32, 1825–1854.

[35] F. Wang, X.-K. Liu, F. Gao in Advanced Nanomaterials for Solar Cells and Light Emitting Diodes, (Ed.: F. Gao), Micro and Nano Technologies, 2019, pp. 1–35.

[36] P. Würfel, U. Würfel, Physics of Solar Cells: From Basic Principles to Advanced Concepts, John Wiley & Sons, 2016.

[37] S. Rühle, Solar Energy 2016, 130, 139–147.

[38] W. Shockley, H. J. Queisser, Journal of Applied Physics 1961, 32, 510–519.

[39] M. Gloeckler, J. R. Sites, W. K. Metzger, Journal of Applied Physics 2005, 98, 113704.

[40] W. K. Metzger, I. L. Repins, M. Romero, P. Dippo, M. Contreras, R. Noufi, D. Levi, Thin Solid Films, Thin Film Chalogenide Photovoltaic Materials (EMRS, Symposium L) 2009, 517, 2360–2364.

[41] B. I. Shklovskii, A. L. Efros, Electronic Properties of Doped Semiconductors, (Eds.: M. Cardona, P. Fulde, H.-J. Queisser), Springer Berlin Heidelberg, Berlin, Heidelberg, 1984.

[42] I. Dirnstorfer, M. Wagner, D. M. Hofmann, M. D. Lampert, F. Karg, B. K. Meyer, physica status solidi (a) 1998, 168, 163–175.

[43] J.-F. Guillemoles, P. Cowache, A. Lusson, K. Fezzaa, F. Boisivon, J. Vedel, D. Lincot, Journal of Applied Physics 1996, 79, 7293–7302.

[44] S. Aksu, S. Pethe, A. Kleiman-Shwarsctein, S. Kundu, M. Pinarbasi in 2012 38th IEEE Photovoltaic Specialists Conference, 2012, pp. 003092–003097.

[45] V. S. Saji, I.-H. Choi, C.-W. Lee, Solar Energy 2011, 85, 2666–2678.

[46] H. Li, F. Qu, H. Luo, X. Niu, J. Chen, Y. Zhang, H. Yao, X. Jia, H. Gu, W. Wang, Results in Physics 2019, 12, 704–711.

[47] C.-H. Huang, W.-J. Chuang, C.-P. Lin, Y.-L. Jan, Y.-C. Shih, Crystals 2018, 8, 296.

[48] M. Behr, M. Sharma, S. Sprague, N. Shinkel, J. Kerbleski, C. Alvey, S. Rozeveld, T. Hasan, C. Wintland, M. Mushrush, A. Wall, Thin Solid Films 2018, 665, 36–45.

[49] N. Weinberger, D. Stock, C. A. Kaufmann, T. Kodalle, M. D. Heinemann, D. Huber, M. Harnisch, A. Zimmermann, G. N. Strauss, R. Lackner, Journal of Vacuum Science & Technology A 2020, 38, 033201.

[50] P. Pistor, S. Zahedi-Azad, S. Hartnauer, L. A. Wägele, E. Jarzembowski, R. Scheer, physica status solidi (a) 2015, 212, 1897–1904.

[51] U. Rau, J. H. Werner, Applied Physics Letters 2004, 84, 3735–3737.

[52] C. D. R. Ludwig, T. Gruhn, C. Felser, J. Windeln in 2011 37th IEEE Photovoltaic Specialists Conference, 2011, pp. 002757–002762.

[53] H. Ru Hsu, S. Chun Hsu, Y.-S. Liu, Applied Physics Letters 2012, 100, 233903.

[54] Y.-C. Lin, K.-T. Liu, T.-P. Hsieh, H.-R. Hsu, Materials Science in Semiconductor Processing 2019, 94, 151–155.

[55] P. Jackson, D. Hariskos, R. Wuerz, O. Kiowski, A. Bauer, T. M. Friedlmeier, M. Powalla, physica status solidi (RRL) – Rapid Research Letters 2015, 9, 28–31.

[56] M. Turcu, O. Pakma, U. Rau, Applied Physics Letters 2002, 80, 2598–2600.

[57] A. Sharan, F. P. Sabino, A. Janotti, N. Gaillard, T. Ogitsu, J. B. Varley, Journal of Applied Physics 2020, 127, 065303.

[58] S. B. Zhang, S.-H. Wei, A. Zunger, H. Katayama-Yoshida, Physical Review B 1998, 57, 15.

[59] J. Pohl, K. Albe, Physical Review B 2013, 87, 245203.

[60] G. Dagan, F. Abou-Elfotouh, D. J. Dunlavy, R. J. Matson, D. Cahen, Chemistry of Materials 1990, 2, 286–293.

[61] J. H. Schön, V. Alberts, E. Bucher, Semiconductor Science and Technology 1999, 14, 657–659.

[62] L. E. Oikkonen, M. G. Ganchenkova, A. P. Seitsonen, R. M. Nieminen, Journal of Physics: Condensed Matter 2014, 26, 345501.

[63] M. Igalson, P. Zabierowski, D. Przado, A. Urbaniak, M. Edoff, W. N. Shafarman, Solar Energy Materials and Solar Cells 2009, 93, 1290–1295.

[64] R. Farshchi, B. Hickey, G. Zapalac, J. Bailey, D. Spaulding, D. Poplavskyy in 2016 IEEE 43rd Photovoltaic Specialists Conference (PVSC), IEEE, Portland, OR, USA, 2016, pp. 2157–2160.

[65] A. Ferguson, Proceedings of the 45th IEEE Photovoltaic Specialist Conference Waikoloa Hawaii 2018, 5.

[66] J. T. Heath, J. D. Cohen, W. N. Shafarman, Journal of Applied Physics 2004, 95, 1000–1010.

[67] S. Lany, A. Zunger, Journal of Applied Physics 2006, 100, 16.

[68] R. Arndt, D. I. R. Puto, Basic Understanding of IEC Standard Testing for Photovoltaic Panels, en-US.

[69] A. J. Ferguson, R. Farshchi, P. K. Paul, P. Dippo, J. Bailey, D. Poplavskyy, A. Khanam, F. Tuomisto, A. R. Arehart, D. Kuciauskas, Journal of Applied Physics 2020, 127, 215702.

[70] R. Farshchi, D. Poplavskyy in 2018 IEEE 7th World Conference on Photovoltaic Energy Conversion (WCPEC) (A Joint Conference of 45th IEEE PVSC, 28th PVSEC & 34th EU PVSEC), IEEE, Waikoloa Village, HI, 2018, pp. 2616–2619.

[71] I. Khatri, K. Shudo, J. Matsuura, M. Sugiyama, T. Nakada, Progress in Photovoltaics: Research and Applications 2018, 26, 171–178.

[72] J. Nishinaga, T. Koida, S. Ishizuka, Y. Kamikawa, H. Takahashi, M. Iioka, H. Higuchi, Y. Ueno, H. Shibata, S. Niki, Applied Physics Express 2017, 10, 092301.

[73] S. J. Heise, V. Gerliz, M. S. Hammer, J. Ohland, J. Keller, I. Hammer-Riedel, Solar Energy Materials and Solar Cells 2017, 163, 270–276.

[74] M. Gostein, L. Dunn in 2011 37th IEEE Photovoltaic Specialists Conference, 2011, pp. 003126–003131.

[75] J. T. Heath, J. D. Cohen, W. N. Shafarman, Thin Solid Films, Proceedings of Symposium B, Thin Film Chalcogenide Photovoltaic Materials, E-MRS Spring Meeting 2003, 431-432, 426–430.

[76] J. Bailey, G. Zapalac, D. Poplavskyy in 2016 IEEE 43rd Photovoltaic Specialists Conference (PVSC), IEEE, Portland, OR, USA, 2016, pp. 2135–2140.

[77] M. Igalson, M. Maciaszek, K. Macielak, A. Czudek, M. Edoff, N. Barreau, Thin Solid Films 2019, 669, 600–604.

[78] J.-F. Guillemoles, L. Kronik, D. Cahen, U. Rau, A. Jasenek, H.-W. Schock, The Journal of Physical Chemistry B 2000, 104, 4849–4862.

[79] S. Soltanmohammad, J. Wands, R. Farshchi, D. Poplavskyy, A. Rockett in 2018 IEEE 7th World Conference on Photovoltaic Energy Conversion (WCPEC), IEEE, Waikoloa Village, HI, 2018, pp. 0852–0855.

[80] A. Duchatelet, G. Savidand, R. N. Vannier, D. Lincot, Thin Solid Films 2013, 545, 94–99.

[81] K. Gartsman, L. Chernyak, V. Lyahovitskaya, D. Cahen, V. Didik, V. Kozlovsky, R. Malkovich, E. Skoryatina, V. Usacheva, Journal of Applied Physics 1997, 82, 4282–4285.

[82] L. Chernyak, K. Gartsman, D. Cahen, O. M. Stafsudd, Journal of Physics and Chemistry of Solids 1995, 56, 1165–1191.

[83] M. Malitckaya, H.-P. Komsa, V. Havu, M. J. Puska, The Journal of Physical Chemistry C 2017, 121, 15516–15528.

[84] J.-F. Guillemoles, U. Rau, L. Kronik, H.-W. Schock, D. Cahen, Advanced Materials 1999, 11, 957–961.

[85] G. Dagan, T. F. Ciszek, D. Cahen, The Journal of Physical Chemistry 1992, 96, 11009–11017.

[86] Y. Sun, S. Lin, W. Li, S. Cheng, Y. Zhang, Y. Liu, W. Liu, Engineering 2017, 3, 452–459.

[87] C.-H. Hsu, Y.-S. Su, S.-Y. Wei, C.-H. Chen, W.-H. Ho, C. Chang, Y.-H. Wu, C.-J. Lin, C.-H. Lai, Progress in Photovoltaics: Research and Applications 2015, 23, 1621–1629.

[88] W. Thongkham, A. Pankiew, K. Yoodee, S. Chatraphorn, Solar Energy 2013, 92, 189–195.

[89] R. Kimura, T. Nakada, P. Fons, A. Yamada, S. Niki, T. Matsuzawa, K. Takahashi, A. Kunioka, Solar Energy Materials and Solar Cells, PVSEC 11 - PART III 2001, 67, 289–295.

[90] F. Babbe, H. Elanzeery, M. Melchiorre, A. Zelenina, S. Siebentritt, Physical Review Materials 2018, 2, 105405.

[91] T. Feurer, F. Fu, T. P. Weiss, E. Avancini, J. Löckinger, S. Buecheler, A. N. Tiwari, Thin Solid Films 2019, 670, 34–40.

[92] D. Hauschild, D. Kreikemeyer-Lorenzo, P. Jackson, T. M. Friedlmeier, D. Hariskos, F. Reinert, M. Powalla, C. Heske, L. Weinhardt, ACS Energy Letters 2017, 2, 2383– 2387.

[93] P. Jackson, R. Wuerz, D. Hariskos, E. Lotter, W. Witte, M. Powalla, physica status solidi (RRL) – Rapid Research Letters 2016, 10, 583–586.

[94] P. Schöppe, S. Schönherr, M. Chugh, H. Mirhosseini, P. Jackson, R. Wuerz, M. Ritzer, A. Johannes, G. Martínez-Criado, W. Wisniewski, T. Schwarz, C. T. Plass, M. Hafermann, T. D. Kühne, C. S. Schnohr, C. Ronning, Nano Energy 2020, 71, 104622.

[95] J. Hedstrom, H. Ohlsen, M. Bodegard, A. Kylner, L. Stolt, D. Hariskos, M. Ruckh, H.-W. Schock in Conference Record of the Twenty Third IEEE Photovoltaic Specialists Conference - 1993 (Cat. No.93CH3283-9), 1993, pp. 364–371.

[96] Y. Kamikawa, J. Nishinaga, S. Ishizuka, T. Tayagaki, H. Guthrey, H. Shibata, K. Matsubara, S. Niki, Journal of Applied Physics 2018, 123, 093101.

[97] D. Colombara, J.-N. Audinot, D. Aureau, F. Babbe, P. J. Dale, H. El Anzeery, H. Guthrey, N. Nicoara, S. Sadewasser, D. Sharma, N. Valle, T. Wirtz, A. Zelenina in 2019 IEEE 46th Photovoltaic Specialists Conference (PVSC), 2019, pp. 0182–0184.

[98] P. Reinhard, B. Bissig, F. Pianezzi, E. Avancini, H. Hagendorfer, D. Keller, P. Fuchs, M. Döbeli, C. Vigo, P. Crivelli, S. Nishiwaki, S. Buecheler, A. N. Tiwari, Chemistry of Materials 2015, 27, 5755–5764.

[99] O. Donzel-Gargand, F. Larsson, T. Törndahl, L. Stolt, M. Edoff, Progress in Photovoltaics: Research and Applications 2019, 27, 220–228.

[100] C. P. Muzzillo, J. D. Poplawsky, H. M. Tong, W. Guo, T. Anderson, Progress in Photovoltaics: Research and Applications 2018, 26, 825–834.

[101] C. P. Muzzillo, L. M. Mansfield, K. Ramanathan, T. J. Anderson, Journal of Materials Science 2016, 51, 6812–6823.

[102] E. Handick, P. Reinhard, J.-H. Alsmeier, L. Köhler, F. Pianezzi, S. Krause, M. Gorgoi, E. Ikenaga, N. Koch, R. G. Wilks, S. Buecheler, A. N. Tiwari, M. Bär, ACS Applied Materials & Interfaces 2015, 7, 27414–27420.

[103] T. Lepetit, S. Harel, L. Arzel, G. Ouvrard, N. Barreau, Progress in Photovoltaics: Research and Applications 2017, 25, 1068–1076.

[104] T. Kodalle, L. Choubrac, L. Arzel, R. Schlatmann, N. Barreau, C. A. Kaufmann, Solar Energy Materials and Solar Cells 2019, 200, 109997.

[105] S. Siebentritt, E. Avancini, M. Bär, J. Bombsch, E. Bourgeois, S. Buecheler, R. Carron, C. Castro, S. Duguay, R. Félix, E. Handick, D. Hariskos, V. Havu, P. Jackson, H.-P. Komsa, T. Kunze, M. Malitckaya, R. Menozzi, M. Nesladek, N. Nicoara, M. Puska, M. Raghuwanshi, P. Pareige, S. Sadewasser, G. Sozzi, A. N. Tiwari, S. Ueda, A. Vilalta-Clemente, T. P. Weiss, F. Werner, R. G. Wilks, W. Witte, M. H. Wolter, Advanced Energy Materials 2020, 10, 1903752.

[106] M. Chugh, T. D. Kühne, H. Mirhosseini, ACS Applied Materials & Interfaces 2019, 11, 14821–14829.

[107] D. Abou-Ras, A. Nikolaeva, S. C. Dávila, M. Krause, H. Guthrey, M. Al-Jassim, M. Morawski, R. Scheer, Solar RRL 2019, 3, 1900095.

[108] I. Khatri, M. Sugiyama, T. Nakada, Progress in Photovoltaics: Research and Applications 2017, 25, 10, 871-877.

[109] J. Dik, K. Janssens, G. Van Der Snickt, L. van der Loeff, K. Rickers, M. Cotte, Analytical Chemistry 2008, 80, 6436–6442.

[110] M. Mantler, M. Schreiner, X-Ray Spectrometry 2000, 29, 3–17.

[111] P. M. Kopittke, T. Punshon, D. J. Paterson, R. V. Tappero, P. Wang, F. P. C. Blamey,A. v. d. Ent, E. Lombi, Plant Physiology 2018, 178, 507–523.

[112] M. A. Ashraf, K. Umetsu, O. Ponomarenko, M. Saito, M. Aslam, O. Antipova, N. Dolgova, C. D. Kiani, S. Nezhati, K. Tanoi, K. Minegishi, K. Nagatsu, T. Kamiya, T. Fujiwara, C. Luschnig, K. Tanino, I. Pickering, G. N. George, A. Rahman, bioRxiv 2019, 710160.

[113] S. Kapishnikov, D. Grolimund, G. Schneider, E. Pereiro, J. G. McNally, J. Als-Nielsen, L. Leiserowitz, Scientific Reports 2017, 7.

[114] G. Kaur, O. Ponomarenko, J. R. Zhou, D. P. Swanlund, K. L. Summers, N. V. Dolgova, O. Antipova, I. J. Pickering, G. N. George, E. M. Leslie, Chemico-Biological Interactions 2020, 327, 109162.

[115] K. Poropatich, T. Paunesku, A. Zander, B. Wray, M. Schipma, P. Dalal, M. Agulnik, S. Chen, B. Lai, O. Antipova, E. Maxey, K. Brown, M. B. Wanzer, D. Gursel, H. Fan, A. Rademaker, G. E. Woloschak, B. B. Mittal, Scientific Reports 2019, 9, 16965.

[116] E. Y. Brister, Z. Vasi, O. Antipova, A. Robinson, X. Tan, A. Agarwal, S. R. Stock, A. Carriero, C.-P. Richter, Hearing Research 2020, 391, 107948.

[117] M. Uo, T. Wada, T. Sugiyama, Japanese Dental Science Review 2015, 51, 2–9.

[118] T. Nietzold, B. M. West, M. Stuckelberger, B. Lai, S. Vogt, M. I. Bertoni, Journal of Visualized Experiments 2018, e56042.

[119] S. Vogt, J. Maser, C. Jacobsen, Journal de Physique IV (Proceedings) 2003, 104, 617–622.

[120] H. Yan, X. Huang, Y. S. Chu, A. Pattammattel, E. Nazaretski, P. Ill in X-Ray Nanoimaging: Instruments and Methods IV, Vol. 11112, International Society for Optics and Photonics, 2019, p. 1111202.

[121] A. E. Morishige, H. S. Laine, M. A. Jensen, P. X. T. Yen, E. E. Looney, S. Vogt, B. Lai, H. Savin, T. Buonassisi in 2016 IEEE 43rd Photovoltaic Specialists Conference (PVSC), 2016, pp. 2006–2010.

[122] K. Medjoubi, N. Leclercq, F. Langlois, A. Buteau, S. Lé, S. Poirier, P. Mercère, M. C. Sforna, C. M. Kewish, A. Somogyi, Journal of Synchrotron Radiation 2013, 20, 293–299.

[123] J. H. Hubbell, P. N. Trehan, N. Singh, B. Chand, D. Mehta, M. L. Garg, R. R. Garg, S. Singh, S. Puri, Journal of Physical and Chemical Reference Data 1994, 23, 339– 364.

[124] C. Ossig, T. Nietzold, B. West, M. Bertoni, G. Falkenberg, C. G. Schroer, M. E. Stuckelberger, Journal of Visualized Experiments 2019, e60001.

[125] B. M. West, M. Stuckelberger, H. Guthrey, L. Chen, B. Lai, J. Maser, V. Rose, W. Shafarman, M. Al-Jassim, M. I. Bertoni, Nano Energy 2017, 32, 488–493.

[126] T. Nietzold, M. Stuckelberger, T. Walker, N. Valdes, B. M. West, B. Lai, W. N. Shafarman, M. I. Bertoni in 2019 IEEE 46th Photovoltaic Specialists Conference (PVSC), 2019, pp. 2164–2166.

[127] A. K. Ehemba, M. M. Socé, J. J. Domingo, S. Cisse, M. Dieng, American Journal of Energy Research 2017, 5, 57–62.

[128] S. V. Firstov, S. V. Alyshev, A. V. Kharakhordin, K. E. Riumkin, E. M. Dianov, Optical Materials Express 2017, 7, 3422–3432.

[129] S.-H. Chen, W.-T. Lin, S.-H. Chan, S.-Z. Tseng, C.-C. Kuo, S.-C. Hu, W.-H. Peng, Y.-T. Lu, ECS Journal of Solid State Science and Technology 2015, 4, P347–P350.

[130] H. Guthrey, J. Moseley, J. Nishinaga, H. Shibata, H. Takahashi, M. Al-Jassim in Physics, Simulation, and Photonic Engineering of Photovoltaic Devices VIII, Vol. 10913, International Society for Optics and Photonics, 2019, p. 1091308.

[131] E. Rudigier, I. Luck, R. Scheer, Applied Physics Letters 2003, 82, 4370–4372.

[132] H. Tanino, H. Fujikake, T. Maeda, H. Nakanishi, Journal of Applied Physics 1993, 74, 2114–2116.

[133] T. Schmid, N. Schäfer, S. Levcenko, T. Rissom, D. Abou-Ras, Scientific Reports 2015, 5, 1–7.

[134] J. R. Ferraro, K. Nakamoto, C. W. Brown, Introductory Raman spectroscopy, 2nd, Academic Press, Amsterdam ; Boston, 2003.

[135] C. Rincón, F. J. Ramírez, Journal of Applied Physics 1992, 72, 4321–4324.

[136] N. H. Valdes, J. Lee, W. N. Shafarman, IEEE Journal of Photovoltaics 2019, 9, 906–911.

[137] C.-M. Xu, X.-L. Xu, J. Xu, X.-J. Yang, J. Zuo, N. Kong, W.-H. Huang, H.-T. Liu, Semiconductor Science and Technology 2004, 19, 1201–1206.

[138] X. Lyu, D. Zhuang, M. Zhao, N. Zhang, X. Yu, L. Zhang, R. Sun, Y. Wei, X. Peng, Y. Wu, G. Ren, J. Wei, Applied Surface Science 2019, 473, 848–854.

[139] S. Mishra, A. Ingale, U. N. Roy, A. Gupta, Thin Solid Films 2007, 516, 91–98.

[140] Y. Jiang, T. Feurer, R. Carron, G. T. Sevilla, T. Moser, S. Pisoni, R. Erni, M. D. Rossell, M. Ochoa, R. Hertwig, A. N. Tiwari, F. Fu, ACS Nano 2020, 14, 7502–7512.

[141] S. Albrecht, B. Rech, Nature Energy 2017, 2, 1–2.

[142] T. Feurer, B. Bissig, T. P. Weiss, R. Carron, E. Avancini, J. Löckinger, S. Buecheler, A. N. Tiwari, Science and Technology of Advanced Materials 2018, 19, 263–270.

[143] M. Langenhorst, B. Sautter, R. Schmager, J. Lehr, E. Ahlswede, M. Powalla, U. Lemmer, B. S. Richards, U. W. Paetzold, Progress in Photovoltaics: Research and Applications 2019, 27, 290–298.

[144] T. Kato, Japanese Journal of Applied Physics 2017, 56, 04CA02.

[145] L. Chen, J. Lee, W. N. Shafarman, IEEE Journal of Photovoltaics 2014, 4, 447–451.

[146] A. Chirila, P. Reinhard, F. Pianezzi, P. Bloesch, A. R. Uhl, C. Fella, L. Kranz, D. Keller, C. Gretener, H. Hagendorfer, D. Jaeger, R. Erni, S. Nishiwaki, S. Buecheler, A. N. Tiwari, Nature Materials 2013, 12, 1107–1111.

[147] N. Valdes, J. Lee, W. Shafarman, Solar Energy Materials and Solar Cells 2019, 195, 155–159.

[148] P. T. Erslev, J. Lee, G. M. Hanket, W. N. Shafarman, J. D. Cohen, Thin Solid Films 2011, 519, 7296–7299.

[149] I. V. Bodnar, I. A. Viktorov, S. L. Sergeev-Nekrasov, Crystal Research and Technology 1998, 33, 885–890.

[150] D. Shin, J. Kim, T. Gershon, R. Mankad, M. Hopstaken, S. Guha, B. T. Ahn, B. Shin, Solar Energy Materials and Solar Cells 2016, 157, 695–702.

[151] N. H. Valdes, K. J. Jones, R. L. Opila, W. N. Shafarman, IEEE Journal of Photovoltaics 2019, 9, 1846–1851.

[152] K. Sopiha, J. K Larsen, O. Donzel-Gargand, F. Khavari, J. Keller, M. Edoff, C. Platzer-Björkman, C. Persson, J. Scragg, Journal of Materials Chemistry A 2020, 8, 8740–8751.

[153] B. H. Toby, R. B. Von Dreele, Journal of Applied Crystallography 2013, 46, 544–549.

[154] B. M. West, M. Stuckelberger, A. Jeffries, S. Gangam, B. Lai, B. Stripe, J. Maser, V. Rose, S. Vogt, M. I. Bertoni, Journal of Synchrotron Radiation 2017, 24, 288–295.

[155] J. H. Werner, J. Mattheis, U. Rau, Thin Solid Films, EMRS 2004 2005, 480-481, 399–409.

[156] E. Handick, P. Reinhard, R. G. Wilks, F. Pianezzi, T. Kunze, D. Kreikemeyer-Lorenzo, L. Weinhardt, M. Blum, W. Yang, M. Gorgoi, E. Ikenaga, D. Gerlach, S. Ueda, Y. Yamashita, T. Chikyow, C. Heske, S. Buecheler, A. N. Tiwari, M. Ba ¨r, ACS Applied Materials & Interfaces 2017, 9, 3581–3589.

[157] Y. Zhang, R. E. Bartolo, S. J. Kwon, M. Dagenais, IEEE Journal of Photovoltaics 2017, 7, 676–683.

[158] J. Chen, H. Shen, Z. Zhai, F. Liu, Z. Zhu, M. Luo, Materials Letters 2020, 127749.

[159] J. H. Boyle, B. E. McCandless, G. M. Hanket, W. N. Shafarman, Thin Solid Films, Proceedings of the EMRS 2010 Spring Meeting Symposium M: Thin Film Chalcogenide Photovoltaic Materials 2011, 519, 7292–7295.

[160] J. H. Boyle, B. E. McCandless, W. N. Shafarman, R. W. Birkmire, Journal of Applied Physics 2014, 115, 223504.

[161] A. Abdi, L. V. Titova, L. M. Smith, H. E. Jackson, J. M. Yarrison-Rice, J. L. Lensch, L. J. Lauhon, Applied Physics Letters 2006, 88, 043118.

[162] M. F. Saleem, H. Zhang, Y. Deng, D. Wang, Journal of Raman Spectroscopy 2017, 48, 224–229.

[163] J. Keller, L. Stolt, K. V. Sopiha, J. K. Larsen, L. Riekehr, M. Edoff, Solar RRL 2020, 2000508.

[164] J. Łażewski, H. Neumann, K. Parlinski, G. Lippold, B. J. Stanbery, Physical Review B 2003, 68, 144108.

[165] S. Shirakata, H. Kubo, C. Hamaguchi, S. Isomura, Japanese Journal of Applied Physics 1997, 36, L1394–L1396.

[166] D. S. Su, W. Neumann, R. Hunger, P. Schubert-Bischoff, M. Giersig, H. J. Lewerenz, R. Scheer, E. Zeitler, Applied Physics Letters 1998, 73, 785–787.

[167] C. Rincón, S. M. Wasim, G. Marín, J. M. Delgado, J. R. Huntzinger, A. Zwick, J. Galibert, Applied Physics Letters 1998, 73, 441–443.

[168] C. Insignares-Cuello, C. Broussillou, V. Bermúdez, E. Saucedo, A. Pérez-Rodríguez, V. Izquierdo-Roca, Applied Physics Letters 2014, 105, 021905.

[169] C. Persson, A. Zunger, Applied Physics Letters 2005, 87, 211904.

[170] R. Mainz, A. Weber, H. Rodriguez-Alvarez, S. Levcenko, M. Klaus, P. Pistor, R. Klenk, H.-W. Schock, Progress in Photovoltaics: Research and Applications 2015, 23, 1131–1143.

[171] A. Onno, C. Chen, P. Koswatta, M. Boccard, Z. C. Holman, Journal of Applied Physics 2019, 126, 183103.

[172] S. Kavadiya, A. Onno, C. C. Boyd, X. Wang, A. Cetta, M. D. McGehee, Z. C. Holman, Solar RRL 2021, 2100107, 9.

[173] H. Elanzeery, F. Babbe, M. Melchiorre, A. Zelenina, S. Siebentritt, IEEE Journal of Photovoltaics 2017, 7, 684–689.

[174] M. Burgelman, F. Engelhardt, J. F. Guillemoles, R. Herberholz, M. Igalson, R. Klenk, M. Lampert, T. Meyer, V. Nadenau, A. Niemegeers, J. Parisi, U. Rau, H. W. Schock, M. Schmitt, O. Seifert, T. Walter, S. Zott, Progress in Photovoltaics: Re- search and Applications 1997, 5, 121–130.

[175] D. K. Schroder, D. C. Gupta, F. R. Bacher, W. H. Hughes, W. M. Hughes, Recombination Lifetime Measurements in Silicon, ASTM International, 1998.

[176] M. E. Stuckelberger, T. Nietzold, B. West, R. Farshchi, D. Poplavskyy, J. Bailey, B. Lai, J. M. Maser, M. I. Bertoni, Journal of Physics: Energy 2020, 2, 025001.

[177] M. Theelen, R. Hendrikx, N. Barreau, H. Steijvers, A. Böttger, Solar Energy Materials and Solar Cells 2016, 157, 943–952.

[178] M. Theelen, S. Harel, M. Verschuren, M. Tomassini, A. Hovestad, N. Barreau, J. van Berkum, Z. Vroon, M. Zeman, Thin Solid Films 2016, 612, 381–392.

[179] M. Theelen, K. Polman, M. Tomassini, N. Barreau, H. Steijvers, J. van Berkum, Z. Vroon, M. Zeman, Surface and Coatings Technology 2014, 252, 157–167.

[180] S. Ouédraogo, M. B. Kébré, A. T. Ngoupo, D. Oubda, F. Zougmoré, J.-M. Ndjaka, Advances in Materials Physics and Chemistry 2020, 10, 151–166.

[181] S. Cheng, B. Li, W. Liu, K. Zhang, Y. Zhang, Z. He, L. Lin, S. Sun, Y. Sun, Optik 2020, 164757.

[182] A. Funaki, K. Arai, S. Aida, S. Phongtamrug, K. Tashiro, Polymer 2008, 49, 5497–5503.

[183] B. Adothu, F. R. Costa, S. Mallick, Solar Energy Materials and Solar Cells 2021, 224, 111024.

[184] F. J. Pern, A. W. Czanderna, Solar Energy Materials and Solar Cells 1992, 25, 3–23.

[185] D. Colombara, F. Werner, T. Schwarz, I. Cañero Infante, Y. Fleming, N. Valle, C. Spindler, E. Vacchieri, G. Rey, M. Guennou, M. Bouttemy, A. G. Manjón, I. Peral Alonso, M. Melchiorre, B. El Adib, B. Gault, D. Raabe, P. J. Dale, S. Siebentritt, Nature Communications 2018, 9.

[186] D. Grecu, A. D. Compaan, Applied Physics Letters 1999, 75, 361–363.

[187] R. Akis, D. Brinkman, I. Sankin, T. Fang, D. Guo, D. Vasileska, C. Ringhofer in 2014 IEEE 40th Photovoltaic Specialist Conference (PVSC), IEEE, Denver, CO, USA, 2014, pp. 3276–3281.

[188] H. Zhao, M. Kumar, C. Persson, physica status solidi (c) 2012, 9, 1600–1603.

[189] J. J. Rehr, J. J. Kas, F. D. Vila, M. P. Prange, K. Jorissen, Physical Chemistry Chemical Physics 2010, 12, 5503–5513.

[190] A. Rockett, Thin Solid Films 2000, 361-362, 330–337.

[191] Y. Jin, S. T. Dunham, IEEE Journal of Photovoltaics 2017, 7, 329–334.

[192] R. Zhou, M. Yu, D. Tweddle, P. Hamer, D. Chen, B. Hallam, A. Ciesla, P. P. Altermatt, P. R. Wilshaw, R. S. Bonilla, Journal of Applied Physics 2020, 127, 024502.

[193] H. J. Leamy, Journal of Applied Physics 1982, 53, R51–R80.

[194] P. O. Grabitz, U. Rau, B. Wille, G. Bilger, J. H. Werner, Journal of Applied Physics 2006, 100, 124501.

[195] G. El-Hajje, D. Ory, J.-F. Guillemoles, L. Lombez, Applied Physics Letters 2016, 109, 022104.

[196] A. Fell, IEEE Transactions on Electron Devices 2013, 60, 733–738.

[197] A. Fell, K. C. Fong, K. R. McIntosh, E. Franklin, A. W. Blakers, IEEE Journal of Photovoltaics 2014, 4, 1040–1045.

[198] A. Fell, K. R. McIntosh, P. P. Altermatt, G. J. M. Janssen, R. Stangl, A. Ho-Baillie, H. Steinkemper, J. Greulich, M. Mu ¨ller, B. Min, K. C. Fong, M. Hermle, I. G. Romijn, M. D. Abbott, IEEE Journal of Photovoltaics 2015, 5, 1250–1263.

[199] S. Karki, P. Paul, G. Rajan, B. Belfore, D. Poudel, A. Rockett, E. Danilov, F. Castel- lano, A. Arehart, S. Marsillac, IEEE Journal of Photovoltaics 2019, 9, 313–318.

[200] G. E. Bunea, K. E. Wilson, Y. Meydbray, M. P. Campbell, D. M. De Ceuster in 2006 IEEE 4th World Conference on Photovoltaic Energy Conference, Vol. 2, 2006, pp. 1312–1314.

[201] J. Bailey, D. Poplavskyy, G. Zapalac, L. Mansfield, W. Shafarman, IEEE Journal of Photovoltaics 2019, 9, 319–324.

[202] J. Yang, H. W. Du, Y. Li, M. Gao, Y. Z. Wan, F. Xu, Z. Q. Ma, AIP Advances 2016, 6, 085215.